National Technical University of Athens
School of Naval Architecture and Marine Engineering
Division of Marine Structures

Analysis of Ship Head-On Collisions

by

Angelos Nikomanis

July, 2023

Declaration

This report is submitted in partial fulfillment of the requirements for the diploma of Integrated Master of Engineering in Naval Architecture and Marine Engineering at the National Technical University of Athens. I declare that this thesis was composed by myself, that the work contained therein is my own, except where explicitly stated otherwise in the text, and that it has not been submitted, in whole or in part, for any other degree or professional qualification.

Angelos Nikomanis

This thesis was conducted under the supervision of Prof. Manolis Samuelides.

The cover photo has been retracted from Instagram webpage @salvage_and _wreck.

Abstract

Head-on collisions are a frequently-observed category of ship accidents, despite the accumulated navigational experience and equipment available to prevent them. The collision bulkhead is fundamental for containing the damage extent, following such accidents. However, the need to accurately assess bow responses during head-on collisions is inextricably linked to design of offshore installations, such as bridge piers and gravity platforms.

In the present study, the bow response of a Panamax Bulk Carrier, bearing a blunt bulbous bow, during a head-on collision accident is simulated, using Finite Element Analysis with Abaqus/CAE. Following design of the bow geometry, the material behavior is modelled using state-of-the-art techniques.

Three mesh sizes are constructed, for a mesh convergence study. The subsequent results reveal that a mesh size in the order of $3t$ is a suitable choice for the simulation of head-on collisions with Finite Elements. Followingly, comprehensive results and damage descriptions are presented, for three separate cases of initial collision speed ($V = 3kn$, $V = 6\ kn$ and $V = 9\ kn$), until dissipation of kinetic energy. The results identify the areas of excessive plastic strains on the bow model, and predict the formation of folds during crushing. The limitation of damage propagation to strictly fore of the collision bulkhead is observed, and the validity of the assumption of static bow crushing is examined.

A study on the relative bulb/stem contribution to the total bow strength reveals contributions of the bulb in the order of 80%, identifying it as the primary structural member resisting the bow deformation.

The present study's results are compared against various simplified analytical techniques for bow crushing analysis, whilst the deformation patterns exhibited are compared against several actual incidents; good agreement is observed, indicating the accuracy of the FEA modelling techniques employed.

Dedication

This thesis report marks the end of my personal studies at the National Technical University of Athens for the degree of Naval Architecture and Marine Engineering.

On this context, I express my wholehearted gratitude towards my thesis supervisor, Prof. Manolis Samuelides, for his guidance, advice and enthusiastic feedback - not only during the composition period of the present thesis, but also during the specialization courses, on which we cooperated and shared opinions and ideas.

Additionally, I would like to thank Ph.D. candidates Nicholas Silionis of the Shipbuilding Technology Laboratory, and Stamatis Fanourgakis of the Ship Design Laboratory; their observations, modelling technique suggestions and assistance in results evaluation has been immensely helpful, and I wish them all the best after completion of their respective theses.

Many thanks are also due to Mr.Vassilios Dimoulas, Bureau Veritas Hellas S.A., for his kind assistance in aspects of modelling ship collisions using Abaqus FEA.

On a more personal note, I am indebted to my family, Vassilios-Alkinoos Nikomanis, Efthimia Anadiotou and Konstantinos Nikomanis, for endlessly supporting me through hardships, for the values they passed on to me, and for (unwillingly) setting examples of who I aspire to become in life.

Last, but of course not the very least, I am forever grateful to the amazing network of my friends, for the unforgettable experiences we shared during these years. In alphabetical order, much love is due to Andreas Alexandris-Galanopoulos (special thanks for proofreading the draft), Iosif Damanakis, Areti Kargioti, Christos Kostopoulos, Isavella Kyprioti, Jacob Kyvelos, Aristeidis Lekkas, Konstantinos Machias, Paul Makris Jr., Michalis Mamaloukas-Frangoulis, Giannis Mertis, Antonis Mylonas, Andreas Ntouklias, Christina-Despoina Papadopoulou, Stamatia Savvidi and Spyros Zafeiris. Many thanks for always standing by my side, and cheers, for the days past, and the days that are yet to come!

Contents

Declaration i

Abstract iii

Dedication v

List of Figures xi

List of Tables xv

Abbreviations xvii

Nomenclature xix

1 Introduction and problem definition 1

1.1 Historical overview of studies of ship collisions 1

1.2 Limit States of Ship Structures 5

1.2.1 Serviceability Limit State (SLS) 5

1.2.2 Fatigue Limit State (FLS) 6

1.2.3 Ultimate Limit State (ULS) 6

1.2.4 Accidental Limit State (ALS) 6

1.3 Categories of accidental ship events 7

1.4 Description of ship head-on collisions 7

1.5 Risk Analysis procedures 9

1.5.1 Review of statistics regarding ship collision events 9

1.5.2 Definition of risk 11

1.5.3 Risk Control Options 12

1.6 An overview of tools for ship structural analysis . . . 13
1.7 Problem definition and current approach . . . 14
1.8 Summary of present work . . . 15

2 Modelling bow collisions using FEA 17
2.1 Introduction to Finite Element modelling for ship structures . . . 17
2.2 Geometric modelling . . . 18
2.3 Material Modelling . . . 20
2.3.1 Materials of plate-members . . . 20
2.3.2 Modelling of material plasticity . . . 20
2.3.3 Strain-rate effects . . . 23
2.3.4 Thickness . . . 27
2.3.5 Failure criteria . . . 28
2.4 Meshing considerations . . . 29
2.4.1 Meshing technique . . . 29
2.4.2 Selection of element type . . . 29
2.4.3 Mesh sizes constructed . . . 30
2.5 Model interactions . . . 35
2.5.1 Constraints . . . 35
2.5.2 Contact interaction . . . 36
2.5.3 Effect of the surrounding water . . . 37
2.5.4 Application of masses . . . 37
2.6 Boundary conditions and load application . . . 38
2.6.1 Boundary condition . . . 38
2.6.2 Load application . . . 38
2.7 Solving scheme . . . 39
2.8 Final modelling remarks . . . 40

3 Results of Finite Element Simulations 41
3.1 Mesh convergence study . . . 41
3.1.1 Mesh convergence on the Force-Displacement curves . . . 42
3.1.2 Mesh convergence on the energy distribution curves . . . 43

3.1.3 Mesh convergence on critical collision parameters 44
3.1.4 Computational costs of mesh convergence study 45
3.2 Results of the intermediate speed simulation 46
3.2.1 Discussion on the force-displacement curve ($V = 6$ kn) 46
3.2.2 Distribution of energies ($V = 6$ kn) 47
3.2.3 Damage description ($V = 6$ kn) 48
3.3 Results of the high-speed simulation 52
3.3.1 Discussion on the force-displacement curve ($V = 9$ kn) 52
3.3.2 Distribution of energies ($V = 9$ kn) 53
3.3.3 Damage description ($V = 9$ kn) 54
3.4 Results of the low-speed simulation 58
3.4.1 Discussion on the force-displacement curve ($V = 3$ kn) 58
3.4.2 Distribution of energies ($V = 3$ kn) 59
3.4.3 Damage description ($V = 3$ kn) 60
3.5 Distribution of forces on the bulb/stem 64
3.5.1 Force distribution from $V = 6$ kn simulation 64
3.5.2 Force distribution from $V = 9$ kn simulation 65
3.5.3 Force distribution from $V = 3$ kn simulation 66
3.5.4 Discussion on bulb/stem contribution (forces/energies) 67
3.6 Comparison of different collision scenarios 68
3.6.1 Comparison of the force-displacement curves 68
3.6.2 Summary of FEA results 69
3.7 Deformation patterns of actual bow collision incidents 69

4 Comparison of FEA results with simplified analytical methodologies 71
4.1 Introduction to simplified analytical methodologies 71
4.2 Division of bow section into L-, T-, and X-elements 72
4.2.1 The smearing-out technique 72
4.2.2 Bow structure discretization 73
4.3 Analytical formulae utilizing L-, T- and X-elements 74
4.3.1 Method of Amdahl (1983) 74

4.3.2 Method of Yang and Caldwell (1988) . . . 74
4.3.3 Method of Abramowicz (1994) . . . 75
4.3.4 Discussion and comparison with FEA results . . . 75
4.4 Simple formulae for the maximum crushing force F_M . . . 77
4.4.1 Method of Pedersen et al. (1993) . . . 77
4.4.2 Method of Zhang et al. (2004) . . . 79
4.5 Simple formulae for the maximum penetration depth . . . 80
4.6 Simple formulae for the force-deformation curve . . . 80
4.7 Conclusions from comparisons with analytical methodologies . . . 82

5 Conclusion and future work 83
5.1 Conclusions from present work results . . . 83
5.2 Recommendations for future work . . . 84

References 85

A Scantlings of Bow Structure 91
A.1 Outer Shell for the bow hull . . . 91
A.2 Deck at 18900 mm scantlings (Upper Deck) . . . 92
A.3 Deck at 13600 mm scantlings . . . 93
A.4 Deck at 9520 mm scantlings . . . 94
A.5 Deck at 5440 mm scantlings . . . 95
A.6 Web Frames at sides scantlings . . . 96
A.7 Double Bottom structure scantlings . . . 97
A.8 Horizontal side longitudinals scantlings . . . 98
A.9 Vertical stiffeners scantlings . . . 99
A.10 Stiffeners at CL section scantlings . . . 100

B Discretization to L-, T- and X- elements 101
B.1 Bulb section (Stage I) . . . 101
B.2 Stem and Bulb section (Stage II) . . . 102
B.3 Section fore of Frame 227 (Stage III) . . . 103
B.4 Section fore of Frame 223 (Stage IV) . . . 104

List of Figures

1.1 Examples of nuclear-powered merchant vessels 1

1.2 Cross-section of N/S Otto Hahn; the collision barrier comprising of stringer decks can be discerned to the side of the nuclear reactor (reproduced from Lettnin (1973)) 2

1.3 Grounding of M/T Amoco Cadiz (left) and its environmental outcome (right) 3

1.4 Schematic of a tanker double hull configuration 3

1.5 The M/T Exxon Valdez oil spill disaster 4

1.6 Illustration of the buffer bow design (reproduced from Kitamura (2000)) . . 4

1.7 Support structures for side shell (reproduced from Van de Graaf et al. (2004)) 5

1.8 Illustration of head-on collision (reproduced from Zhang et al. (2004)) . . . 8

1.9 Idealized behavior of Force-Displacement curve during axial crushing loads on box-like thin-walled structures (reproduced from Zhang et al. (2004)) . . 8

1.10 The Great Belt bridge, in case of a head-on collision against its piers 9

1.11 Classification of marine incidents with regard to ship type and navigational area (reproduced from EMSA (2022)) 10

1.12 Number of injuries, classified by cause (reproduced from EMSA (2022)) . . 10

1.13 Incidents resulting in considerable consequences to the ship structure, classified by cause (reproduced from EMSA (2022)) 11

1.14 Schematic of the IMO FSA procedure (reproduced from Pedersen (2010)) . 13

2.1 Assembled bow geometry in Abaqus/CAE environment 19

2.2 Illustration of ”engineering” vs ”true” stress-strain curves (reproduced from Pedersen et al. (2019)) 21

2.3 Grade A steel: True stress vs true strain curve imported to Abaqus/CAE . 23

2.4 AH36 steel: True stress vs true strain curve imported to Abaqus/CAE . . . 23
2.5 Effect of strain rate on yield stress according to Cowper and Symonds (1957) 25
2.6 Effect of strain-rate on Grade A steel (as imported to Abaqus/CAE) 27
2.7 Effect of strain-rate on AH36 steel (as imported to Abaqus/CAE) 27
2.8 Typical bow crushing deformation patterns 28
2.9 Coarse mesh ($\sim 15t$) constructed in Abaqus/CAE environment 32
2.10 Fine mesh ($\sim 7-8t$) constructed in Abaqus/CAE environment 33
2.11 Very fine mesh ($\sim 3-4t$) constructed in Abaqus/CAE environment 34
2.12 Starboard view of FEA model interactions in Abaqus/CAE environment . . 36
2.13 Schematic of "hard" pressure-overclosure formulation (Abaqus 6.14 (2014)) 36

3.1 Force-displacement curves for various mesh sizes (6 kn simulation) 42
3.2 Energy distributions for various mesh sizes (6 kn simulation) 43
3.3 Results of mesh convergence study (6 kn simulation) 44
3.4 Computational time for each mesh size (6 kn simulation) 45
3.5 Force-displacement curve (6 kn simulation) 46
3.6 Distribution of model energies (6 kn simulation) 47
3.7 Initial position at t=0 (6 kn simulation) 48
3.8 Deformation pattern at t=0.64 sec (6 kn simulation) 48
3.9 Deformation pattern at t=1.28 sec (6 kn simulation) 49
3.10 Deformation pattern at t=1.92 sec (6 kn simulation) 49
3.11 Final position at t=2.56 sec (6 kn simulation) 49
3.12 Initial undeformed position at t=0 (6 kn simulation) 50
3.13 Distribution of equivalent plastic strains at t=0.34 sec (6 kn simulation) . . 50
3.14 Distribution of equivalent plastic strains at t=0.82 sec (6 kn simulation) . . 51
3.15 Distribution of equivalent plastic strains at t=2.56 sec (6 kn simulation) . . 51
3.16 Force-displacement curve (9 kn simulation) 52
3.17 Distribution of model energies (9 kn simulation) 53
3.18 Initial position at t=0 (9 kn simulation) 54
3.19 Deformation pattern at t=0.624 sec (9 kn simulation) 54
3.20 Deformation pattern at t=1.25 sec (9 kn simulation) 55

3.21 Deformation pattern at t=1.874 sec (9 kn simulation) 55
3.22 Final position at t=2.52 sec (9 kn simulation) 55
3.23 Initial undeformed position at t=0 (9 kn simulation) 56
3.24 Distribution of equivalent plastic strains at t=0.45 sec (9 kn simulation) . . 56
3.25 Distribution of equivalent plastic strains at t=1.626 sec (9 kn simulation) . 57
3.26 Distribution of equivalent plastic strains at t=2.52 sec (9 kn simulation) . . 57
3.27 Force-displacement curve (3 kn simulation) 58
3.28 Distribution of model energies (3 kn simulation) 59
3.29 Initial position at t=0 (3 kn simulation) 60
3.30 Deformation pattern at t=0.53 sec (3 kn simulation) 60
3.31 Deformation pattern at t=1.06 sec (3 kn simulation) 60
3.32 Deformation pattern at t=1.59 sec (3 kn simulation) 61
3.33 Final position at t=2.12 sec (3 kn simulation) 61
3.34 Initial undeformed position at t=0 (3 kn simulation) 62
3.35 Distribution of equivalent plastic strains at t=0.218 sec (3 kn simulation) . 62
3.36 Distribution of equivalent plastic strains at t=0.72 sec (3 kn simulation) . . 63
3.37 Distribution of equivalent plastic strains at t=2.12 sec (3 kn simulation) . . 63
3.38 Force distribution (V = 6 kn simulation) 64
3.39 Force distribution (V = 9 kn simulation) 65
3.40 Force distribution (V = 3 kn simulation) 66
3.41 Comparison of Force-Displacement curves for various collision speeds 68
3.42 Deformation patterns of actual bow collision incidents 69

4.1 Division of plated ship structure into L-, T- and X-shaped elements 71
4.2 The smearing-out technique (reproduced from Yamada and Pedersen (2008)) 73
4.3 Comparison of Force-Displacement curve with simplified analytical formulas 76
4.4 Comparison of Force-Displacement curve with averaged analytical formulas 77
4.5 Zhang et al. (2004)'s method for the F-d curve, compared with FEA results 81

A.1 Snapshot of Outer Shell (starboard view) in Abaqus/CAE environment . . 91
A.2 Bottom view of Deck at 18900 mm (Upper) in Abaqus/CAE environment . 92
A.3 Bottom view of Deck at 13600 mm in Abaqus/CAE environment 93

A.4 Bottom view of Deck at 9520 mm in Abaqus/CAE environment 94
A.5 Bottom view of Deck at 5440 mm in Abaqus/CAE environment 95
A.6 Aft view of strengthened Web Frames 223-227 in Abaqus/CAE environment 96
A.7 Top view of double bottom structure in Abaqus/CAE environment 97
A.8 Top view of bow horizontal stiffening in Abaqus/CAE environment 98
A.9 Aft view of vertical stiffeners in Abaqus/CAE environment 99
A.10 Starboard view of bow fore CL stiffeners in Abaqus/CAE environment . . . 100

B.1 Bulb discretization to L-, T- and X- elements 101
B.2 Bulb-stem discretization to L-, T- and X- elements 102
B.3 Section fore of Fr. 227 discretization to L-, T- and X- elements 103
B.4 Section fore of Fr. 223 discretization to L-, T- and X- elements 104

List of Tables

1.1 Failure modes of accident categories (reproduced from Liu et al. (2018a)) . 7

2.1 General Particulars of Panamax Bulk Carrier under consideration 18
2.2 Nominal properties of materials used, according to CSR (2023) 20
2.3 Power law coefficients calculations, based on the method of Liu et al. (2017) 22
2.4 Calculation of material constants A and B suggested by Jones (1989) 25
2.5 Maximum expected strain-rate values (suggested by Ko et al. (2018)) 26
2.6 Parameters of constructed meshes 34
2.7 Calculations of added mass magnitude and location in Abaqus/CAE local CS 38
2.8 Collision cases examined in the present study 38

3.1 Summary of important results of FEA simulations 69

4.1 Results of application of Pedersen et al. (1993)'s formula for F_M calculation 78
4.2 Results of application of Zhang et al. (2004)'s formula for F_M calculation . 79
4.3 Results of application of Zhang et al. (2004)'s formula for d_{max} calculation . 80

A.1 Scantlings of Deck at 18900 mm 92
A.2 Scantlings of Deck at 13600 mm 93
A.3 Scantlings of Deck at 9520 mm 94
A.4 Scantlings of Deck at 5440 mm 95
A.5 Scantlings of strengthened Web Frames 96
A.6 Scantlings of double bottom grillage structure 97
A.7 Scantlings of horizontal stiffeners (side girders) 98

A.8 Scantlings of vertical stiffeners (pillars & girders) 99
A.9 Scantlings of CL section stiffeners 100

B.1 Scantlings of bulb section L-, T- and X- elements 102
B.2 Scantlings of bulb-stem section L-, T- and X- elements 102
B.3 Scantlings of Fr. 227 section L-, T- and X- elements 103
B.4 Scantlings of Fr. 223 section L-, T- and X- elements 104

Abbreviations

ALS Accidental Limit State.

ASIS The Japanese Association for Structural Improvement of the Shipbuilding Industry.

bbl Barrel of crude oil.

CAE Computer-Aided Engineering.

CFL Courant-Friedrichs-Lewy condition.

CL Centerline.

COG Center of Gravity.

CS Coordinate-system.

CSR Common Structural Rules for Bulk Carriers and Oil Tankers (2023).

DWT Ship's Deadweight Tonnage.

EMSA The European Maritime Safety Agency.

F/V Fishing Vehicle.

FEA Finite Element Analysis.

FEM Finite Element Method.

FLS Fatigue Limit State.

FSA Formal Safety Assessment.

IMO The International Maritime Organization.

LS Ship's Lightship weight.

M/T Motor Tanker.

M/V Merchant Vehicle.

N/S Nuclear Ship.

NLFEM Non-linear Finite Element Method.

PS Port Side.

RCO Risk Control Options.

RP Reference Point.

SLS Serviceability Limit State.

SS Starboard Side.

ULS Ultimate Limit State.

Nomenclature

Term	Description	Units
B	Ship Beam	m
C_B	Ship Block coefficient, $= \frac{\Delta}{\gamma \cdot L_{BP} \cdot B \cdot T}$	–
C_M	Ship midship section coefficient	–
C_P	Ship prismatic coefficient, $= \frac{C_B}{C_M}$	–
D	Cowper-Symonds denominator coefficient	sec^{-1}
E	Young's modulus of elasticity	GPa
E_K	Kinetic energy	J or MJ
$E_{frictional}$	Frictional energy	J or MJ
$E_{internal}$	Internal energy	J or MJ
F	Force	N or kN or MN
F_M	Maximum crushing force	kN or MN
F_m	Mean crushing force (see Figure 1.9)	kN or MN
K	Power law coefficient	MPa
L_{BP}	Ship length between perpendiculars	m
T	Ship Draft	m
V	Ship speed	kn
V_s	Ship service speed	kn
Δ	Ship displacement	t
$\dot{\epsilon}$	Strain rate	sec^{-1}
ϵ_f	Engineering fracture strain	–

Term	Description	Units
ϵ_{pl}	Plastic strain	–
ϵ_{true}	True strain (based on updated dimensions)	–
γ	Seawater density, = 1.025	$\frac{t}{m^3}$
μ	Friction coefficient	–
ν	Poisson's ratio	–
ρ	Density	t/mm^3
σ_0	Material flow stress, = $\frac{\sigma_y+\sigma_{UTS}}{2}$	MPa
σ_{UTS}	Material ultimate tensile strength	MPa
σ_{true}	True stress (based on updated dimensions)	MPa
σ_y	Material yield stress	MPa
b_f	Breadth of T-bar stiffener flange	mm
d	Penetration/Displacement	m
d_{max}	Maximum penetration/displacement	m
h_w	Height of stiffener web	mm
m_{ax}	Added mass coefficient in the surge direction	–
n	Power law strain hardening exponent	–
q	Cowper-Symonds exponential coefficient	–
t	Plate-member thickness	mm
t_c	Corrosion addition to plate-member thickness	mm
t_f	Thickness of T-bar stiffener flange	mm
t_w	Thickness of stiffener web	mm
x_{CG}	Longitudinal coordinate of center of gravity	mm
y_{CG}	Transverse coordinate of center of gravity	mm
z_{CG}	Vertical coordinate of center of gravity	mm

Note: Other terms are introduced as they are presented in the text.

Chapter 1

Introduction and problem definition

1.1 Historical overview of studies of ship collisions

Design of ships against collision loads has been an integrated part of ship design, ever since nuclear powered merchant vessels first appeared, during the 1950s. The first, N/S Savannah, configured to carry passengers and dry bulk cargo (mainly in United States' ports), began construction in 1958, made her maiden voyage in 1962, and ended her service in 1971. Today, N/S Savannah is considered a National Historic Landmark, moored in Baltimore, U.S.A. (see Figure 1.1a).

An additional example of nuclear power in civil service was N/S Otto Hahn, planned to carry passengers and ore. His keel was laid in 1963 and his first voyage completed in 1970, however his nuclear reactor was replaced with a diesel engine in 1979. After several renamings, N/S Otto Hahn ended his service in 2009, as he was scrapped (see Figure 1.1b).

(a) N/S Savannah (2022)

(b) N/S Otto Hahn (1977)

Figure 1.1: Examples of nuclear-powered merchant vessels

Since the main concern with nuclear powered vessels for civil use is the protection of the reactor against radioactive leakage during accidents (an event which would prove catastrophic), studies were undertaken in the design stage, in order to ensure a reliable structural design solution to protect the reactor, in case of side shell or bottom breaching.

The main outcome of such studies was the implementation of intermediate stringer decks, stiffened with additional transverse members, in order to further delay deck buckling (Akita et al. (1972)). Such configurations are better suited to absorb the kinetic energy associated with a ship-ship side collision (see, for reference, Figure 1.2). Specifically, N/S Savannah could withstand a side collision with a tanker bow, travelling with a speed of 15 knots (the available kinetic energy to cause structural damage being approximately 670 MJ), without considerable damage to the nuclear reactor space (Samuelides (2015)).

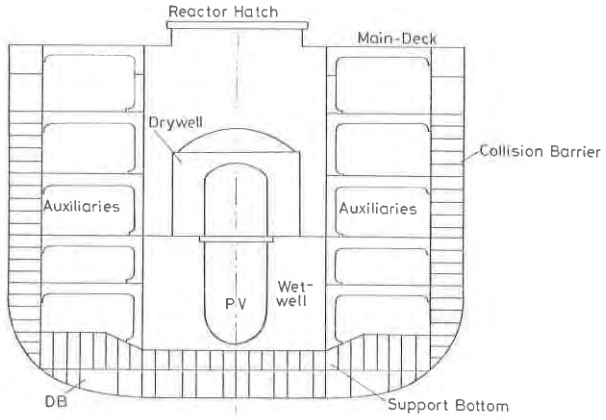

Figure 1.2: Cross-section of N/S Otto Hahn; the collision barrier comprising of stringer decks can be discerned to the side of the nuclear reactor (reproduced from Lettnin (1973))

The method employed for the damage assessment of ship to ship side collisions was that developed by Minorsky (1959); it relates the volume R_T of the damaged material of the struck and striking ships to the energy E_D they absorb, through a linear expression (see Eq. 1.1), provided that the structural elements considered are heavily damaged:

$$E_D\ [MJ] = 32 + 47 \cdot R_T\ [m^3] \tag{1.1}$$

Despite the satisfactory levels of safety achieved through the aforementioned structural configurations, nuclear marine propulsion for merchant vessels was abandoned (only four such ships were ever built - excluding icebreakers), as they proved too expensive to operate.

Nevertheless, research on analysis of collision accidents shifted focus towards prevention of pollution caused by oil outflow from damaged tankers, during the 1970s, especially following the grounding of M/T Amoco Cadiz in 1978 (see Figure 1.3).

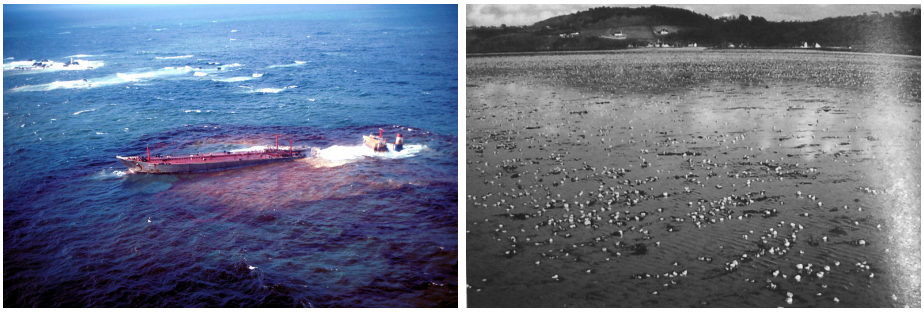

Figure 1.3: Grounding of M/T Amoco Cadiz (left) and its environmental outcome (right)

More specifically, the requirement during design of tankers against accidental loads was to avoid rupture of the cargo holds carrying crude oil. In order to reach this goal, double bottoms and double hull configurations (see Figure 1.4) were proposed during the 1970s, in Annex I, Regulation 19 of the International Convention for the Prevention of Pollution from Ships (MARPOL 73/78 (1992)).

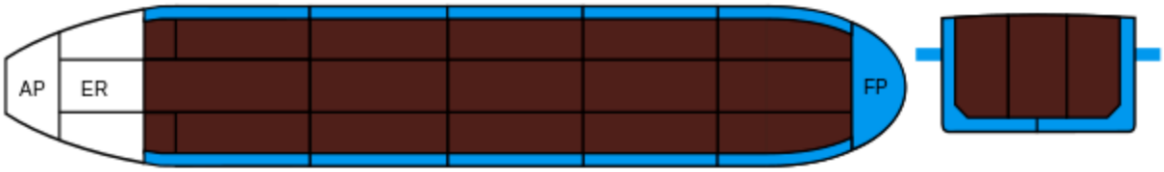

Figure 1.4: Schematic of a tanker double hull configuration

It should be noted that the double hull configuration is sufficient to protect against penetration of the inner side only in low-energy collisions. In high-energy collisions, the inner compartment is usually penetrated as well, however it assists in containing the damage extent, as well as significantly reducing the amount of oil spilled, through absorption of the kinetic energy available to cause structural damage (Pedersen (2010)).

After the M/T Exxon Valdez oil spill disaster in Alaska in 1989, which resulted in the (then) largest oil spill in U.S. waters (2^{nd} largest up to this day), releasing more than 260,000 bbl of crude oil (see Figure 1.5), the Oil Pollution Act of 1990 (OPA (1990)) required all oil tankers for use in U.S. ports to be constructed with a double hull configuration.

(a) M/T Exxon Valdez, protected with oil booms, following the 1989 accident

(b) Footage from the oil spill cleanup operations, which lasted three years

Figure 1.5: The M/T Exxon Valdez oil spill disaster

The International Maritime Organization (IMO) also adopted the mandatory design and construction of all oil tankers with a double hull (or a design providing equivalent protection against oil outflow) in 1992. Gradual phase-out of single-hull tankers from the world fleet was adopted after the M/V Erika incident at the coast of France in 1999.

Research for structural configurations capable of withstanding high-energy collisions is ongoing, to ensure better protection of oil tanker side shells. As a result of an extensive research project conducted by the Japanese Association for Structural Improvement of the Shipbuilding Industry (ASIS) during 1991-1997, Kitamura (2000) identified the need for a low crushing rigidity of the bow (smaller than the side structure of the struck ship), whilst maintaining the energy absorption capability of the bow as large as possible. The buffer bow design was proposed (see Figure 1.6), which constitutes of a bumper forehead above the waterline, and a bulbous bow design, stiffened only with vertical ring frames.

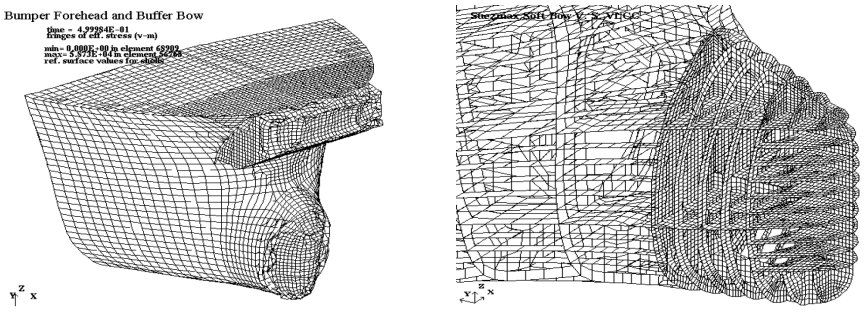

(a) View of buffer bow design; proposed bumper forehead can be discerned

(b) Bulb support structure, consisting mainly of vertical ring frames

Figure 1.6: Illustration of the buffer bow design (reproduced from Kitamura (2000))

More recently, Van de Graaf et al. (2004) suggested an innovative Y-shaped support structure for the side shell of a chemical cargo tanker, demonstrating greater capability for energy absorption than conventional designs. This design, also adapted for double hull carriers, has been proposed and implemented by Damen Schelde Naval Shipbuilding (see Figures 1.10a and 1.10b); it provokes the side shell membrane response before the web frames collapse, thus allowing for greater energy absorption before the cargo hold rupture.

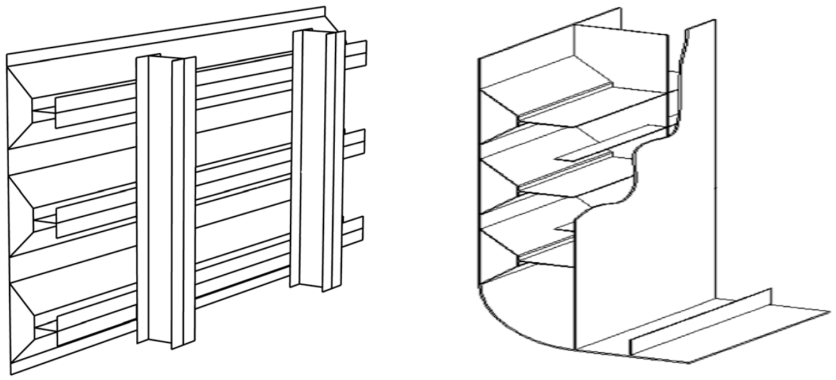

(a) Y-frame core for single hull design (b) Y-frame core for double hull design

Figure 1.7: Support structures for side shell (reproduced from Van de Graaf et al. (2004))

1.2 Limit States of Ship Structures

Traditional structural design is performed by keeping the response stresses due to specific loads under acceptable working levels (a method termed Allowable Stress Design).

In contrast, the Limit State Design considers explicitly the different loading conditions expected, and accordingly evaluates the structural capacity when the structure fails to perform its designated function, defining it as a limit for such a behavior (Paik (2018)).

Recent trends on structural analysis of marine structures place emphasis on Limit State Design, versus the traditional Allowable Stress Design; the following four types of limit states are usually evaluated:

1.2.1 Serviceability Limit State (SLS)

The SLS considers functional failure of the structure due to normal operational loads, frequently experienced and regularly expected during the lifetime of the structure.

1.2.2 Fatigue Limit State (FLS)

The FLS considers functional failure of the structure due to repeated (cyclic) loading, causing fatigue cracking, local stress concentrations and crack growth until fracture. The loads considered are normal operational in a cyclic fashion, however the behavior under consideration is the long-term effect (typically a few years) of the exposure to such loads.

1.2.3 Ultimate Limit State (ULS)

The ULS considers functional failure of the structure due to complete loss of strength capacity. Typical examples of failure in ULS include:

- Complete loss of structural capacity by gross yielding or plastic collapse
- Loss of equilibrium, such as capsizing
- Structural instabilities, such as buckling

The loads considered are extreme, expected to be encountered no more than once during the lifetime of the structure.

1.2.4 Accidental Limit State (ALS)

During Accidental Limit State (ALS) analyses, a target structure is submitted to accidental scenarios and subsequent loads, such as collision, grounding, fire and explosion. The results are consequently assessed as acceptable or not, and usually consider the survivability of the structure after the accident, as well as minimization of the consequences.

In order to perform an ALS analysis, one needs to define (Wang et al. (2002)):

- The accident scenario under consideration.
- The structural analysis method to assess the response to the various loads.
- The acceptance criteria, usually in conjunction with acceptable levels of loss of human lives, environmental pollution and/or financial losses.

The analysis may be performed either in a probabilistic or a deterministic manner.

The present study considers an ALS, where the accidental scenario is predefined in a deterministic fashion.

1.3 Categories of accidental ship events

Accidental events encountered by a ship structure can generally be classified into one of the following categories (Liu et al. (2018a)):

1. Ship grounding, with the predominant mode of deformation being vertical penetration (henceforth referred to as "stranding").

2. Ship grounding, with the predominant mode of deformation being horizontal sliding (henceforth referred to as "raking"). The accident of the Exxon Valdez (see Figure 1.5) is a notorious example of this category.

3. Ship side penetration (henceforth referred to as "side collision").

4. Bow crushing during head-on collisions (henceforth referred to as "bow collision").

The present study focuses on the latter category.

The various different failure modes of individual plate elements, associated with each of the aforementioned accident categories, are presented in Table 1.1:

Scenario	Main failure mode of plate elements			
	Tension	Folding/Crushing	Tearing/Cutting	Sliding
Side collision	X	X		
Bow collision		X		
Stranding	X	X		
Raking		X	X	X

Table 1.1: Failure modes of accident categories (reproduced from Liu et al. (2018a))

It can be deduced that in bow collisions, the main failure modes expected are folding and crushing of individual plated elements. Formation of neck, tearing, formation and propagation of rupture are of lesser concern.

1.4 Description of ship head-on collisions

Ship bow collisions occur when a ship, sailing either in the open sea or in restricted waterways (Pedersen et al. (1993)):

1. Experiences problems with the steering gear/propulsion system in the vicinity of a hazard, when following their ordinary route.

2. Fails to change course at the specified turning point near the hazard.

3. Carries out unsuccessful evasive actions in the vicinity of the hazard, or

4. Sails off-course/drifts.

Additionally, in order for the collision to be classified as bow (head-on), the hazard's three-dimensional features should be large enough (comparable to the ship's beam and draft), whilst providing enough rigidity, so that the ship's bow structure exhibits large deformations and strains, following the incident (see Figure 1.8).

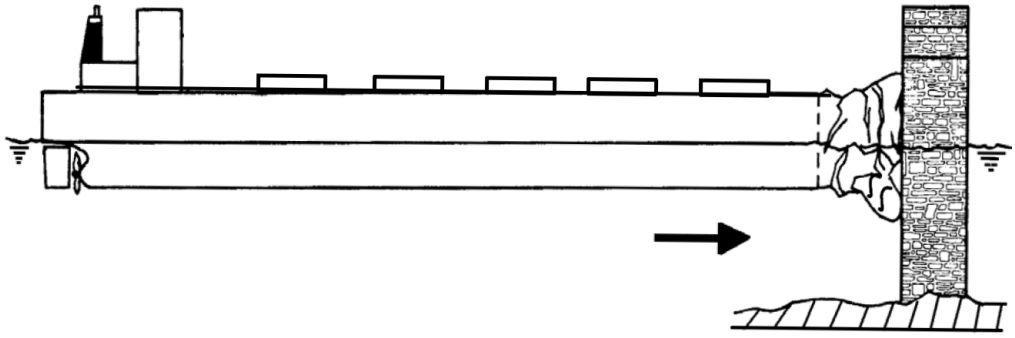

Figure 1.8: Illustration of head-on collision (reproduced from Zhang et al. (2004))

Past experience has revealed that even during high-energy bow collisions (the available kinetic energy being a few hundred MJ), the majority of the damage is contained locally fore of the collision bulkhead, since it provides a rigid support to the adjacent structure.

As such, the ship bow behaves like a slender thin-walled structure, loaded axially in a compressive fashion. The deformation pattern comprises of progressive folding of the bow structure (fore of the collision bulkhead), also observed in an idealized force-displacement curve as sinusoidal fluctuations around a mean resistance force F_m (see Figure 1.9).

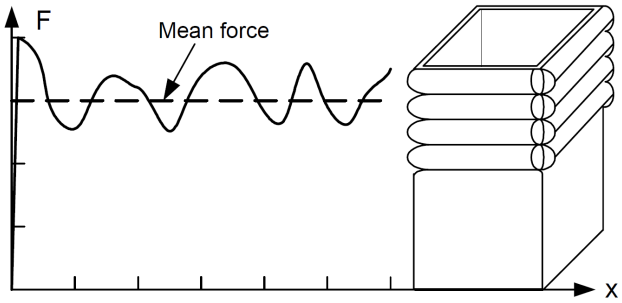

Figure 1.9: Idealized behavior of Force-Displacement curve during axial crushing loads on box-like thin-walled structures (reproduced from Zhang et al. (2004))

The hazard can be modelled as a rigid flat obstacle, in the case of collision against concrete bridge piers or gravity offshore platforms. This accidental scenario has been extensively studied for the design and construction of the Great Belt Bridge in Denmark, finished in 1997 and connecting the Danish islands of Zealand and Funen (see Figure 1.10).

(a) M/V Allure of the Seas, passing under the Great Belt Bridge (2010)

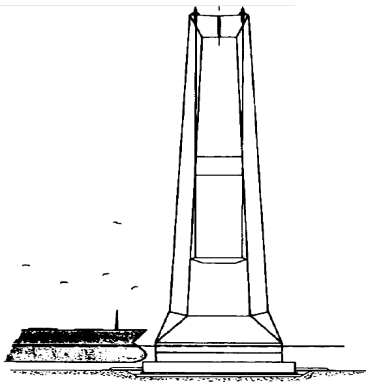

(b) Schematic of bow collision against bridge pier (from Pedersen et al. (1993))

Figure 1.10: The Great Belt bridge, in case of a head-on collision against its piers

1.5 Risk Analysis procedures

1.5.1 Review of statistics regarding ship collision events

Collision and grounding events are dominant concerns in the maritime industry, not only for protection of the ship structure, cargo and general owner property, but for environmental considerations as well.

In an overview of marine casualties in the period 2014-2021, presented by the European Maritime Safety Agency (EMSA (2022)), it was concluded that:

- During the period 2014-2021, 41% (4312) of all incidents regarding cargo ships occurred in internal waters/port areas, where the sailing speeds are usually limited, but increased marine traffic is observed. This was by far the most dominant class among categories of navigational areas for this ship type (see Figure 1.11).

- Contact with an external object is one of the most dangerous classes of marine accidents, being consistently one of the three most injury-provoking causes from 2014 all the way up to 2021 (see Figure 1.12). It should be noted that in this publication,

a collision is defined as necessarily involving two ships, hence bow collisions against rigid obstacles fall under the ”Contact” category.

- Contact events with considerable impact to the ship structure continue to occur annually with no apparent downward trend, despite the accumulated navigational experience and the modernization of relevant equipment (see Figure 1.13).

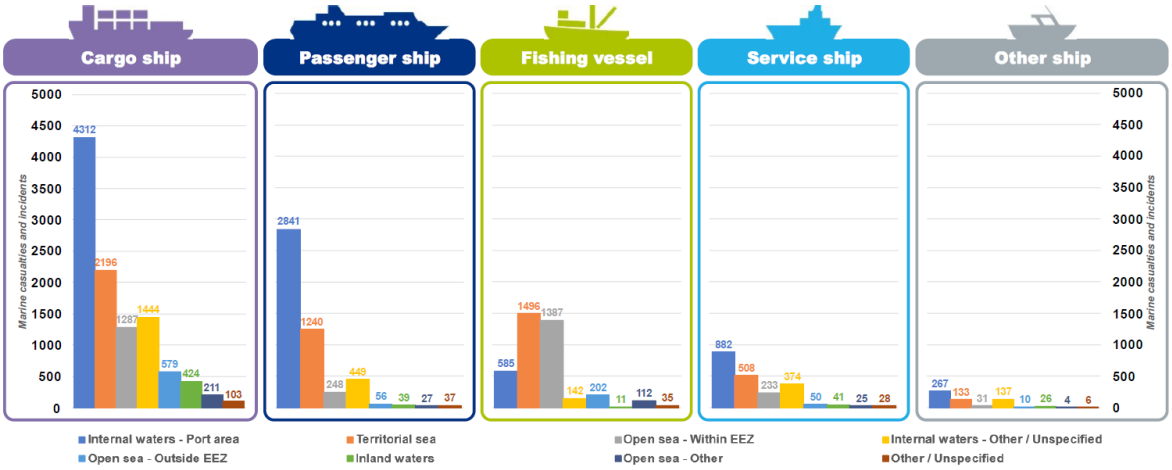

Figure 1.11: Classification of marine incidents with regard to ship type and navigational area (reproduced from EMSA (2022))

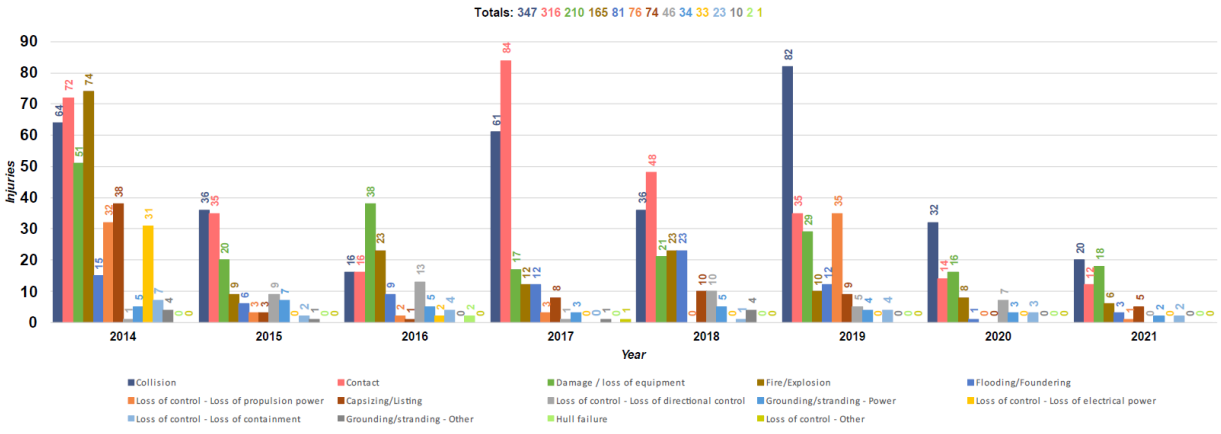

Figure 1.12: Number of injuries, classified by cause (reproduced from EMSA (2022))

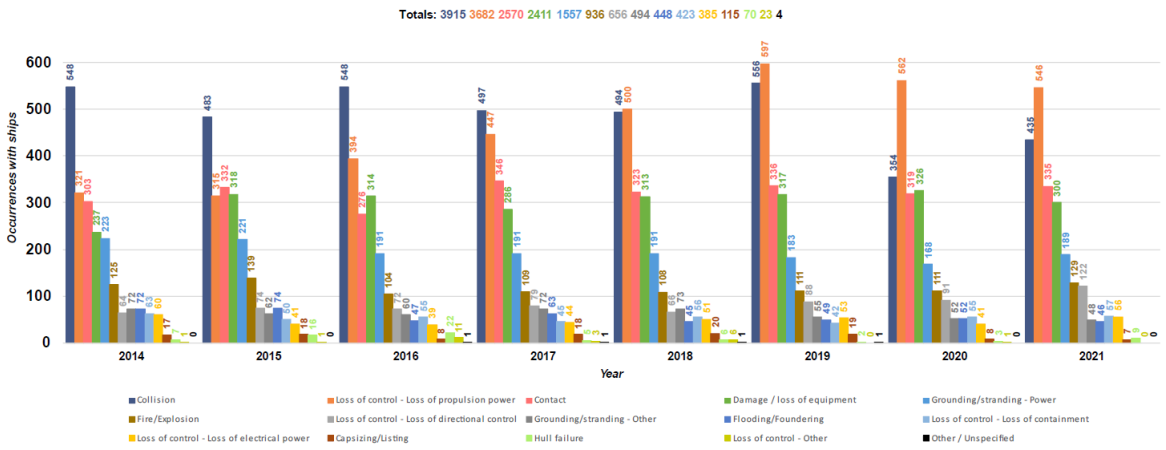

Figure 1.13: Incidents resulting in considerable consequences to the ship structure, classified by cause (reproduced from EMSA (2022))

In a study conducted by Samuelides et al. (2009) and concerning the accidents involving ships with Greek flag from 1992 to 2005, it was reported that dry bulk cargo ships are associated with 58% of the total number of collision and grounding events observed in the fleet. Additionally, the most accident-prone category regarding ship age was the 21+ years old, and the size of the vessel can be considered an independent variable.

Hence, it appears that contact accidents, concerning dry bulk cargo vessels (size is irrelevant), sailing in internal waters/port areas (that is, with restricted speeds and not sailing at full speed) is an important category of marine accidents, in need of proper structural analysis and further research.

1.5.2 Definition of risk

The most often-used mathematical expression for the calculation of the risk associated with a specific event i under consideration is the following (Kristiansen and Haugen (2023)):

$$R_i = P_i \cdot C_i \tag{1.2}$$

where R_i denotes the risk associated with event i, P_i denotes the probability of occurrence of event i, and C_i denotes the consequences of event i, evaluated either with regard to human life, or (more conveniently, in order to take into account multiple consequences, such as human life, loss of cargo, environmental damage etc.) in a monetarist fashion.

Despite several inconsistencies arising from the simplicity of this definition, which (all things considered) is still a matter of scientific research, it is adopted hereafter, so as to reach several conclusions.

In accordance with definition 1.2, in order to mitigate the risk R_i associated with collision and grounding events, the analyst should place emphasis either (Samuelides (2009)):

1. On the minimization of the probability P_i of occurrence of such events (active safety / prevention). Measures improving the probability of collision occurrence include installation of proper instrumentation on-board, training of the ship crew to familiarize with equipment use, and introduction of emergency procedures.

2. On the minimization of the consequences C_i (equivalently, on the minimization of the damage extent), given that the accident scenario has happened (passive safety / mitigation). Relevant measures include further compartmentation of the hull, innovative structural configurations (such as depicted in Figures 1.6 and 1.7) and appropriate arrangement of cargo/fuel tanks.

3. On both aspects (measures controlling both P_i and C_i). Such a measure could be restrictions on the sailing speed of vessels, when navigating in high-traffic areas.

1.5.3 Risk Control Options

A risk related to an event under consideration is usually assessed on the context of a Formal Safety Assessment (FSA). A FSA is defined as a systematic process, targeting the evaluation of risk associated with maritime safety and subsequent protection of the environment, by estimating costs/benefits from implementing proposed measures to counteract the aforementioned risk (IMO (2018)).

A schematic of the procedure required for a FSA is depicted in Figure 1.14.

On this context, a structural analysis is performed on evaluation of e.g. capacity of the structure to withstand specific loads, and if the associated risk is non-satisfactory, specific countermeasures are proposed, termed Risk Control Options (RCOs).

The proposed RCOs are then studied in detail, in order to assess the risk reduction achieved, as well as their implementation costs (Cost-Benefit Assessment), before finalizing the resulting decisions of the FSA.

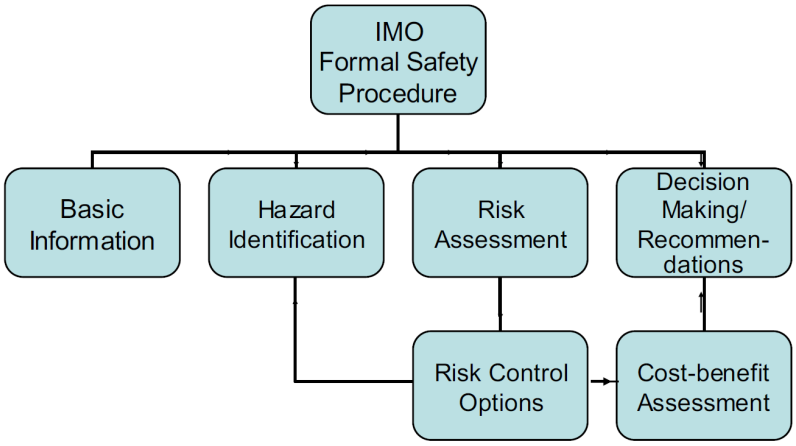

Figure 1.14: Schematic of the IMO FSA procedure (reproduced from Pedersen (2010))

1.6 An overview of tools for ship structural analysis

In order to assess the crashworthiness of a marine structure, as required in order to concur whether the proposed design is structurally sound and safe, a number of tools and methods may be employed, depending on the accidental scenario. These tools are usually classified into one of the following three categories (Samuelides (2015)):

1. Numerical tools, such as finite element modellers and solvers.

2. Analytical tools, usually based on the upper or lower bound theorems of collapse loads. Such methodologies (more often than not) utilize a priori expected kinematic deformation fields, meaning the analyst has to predict the expected modes of failure of the main structural elements (hence, some degree of relevant experience is required).

3. Experimental tools, employing measurements from actual incidents or laboratory experiments. Experimental data are often of paramount importance, in order to validate any newly-proposed analytical or numerical procedure.

1.7 Problem definition and current approach

In accordance with the remarks of sections 1.2 through 1.6, in the present study, an accident is assumed to occur on a specific vessel, (i.e. an Accidental Limit State is to be assessed, see subsection 1.2.4). The accidental scenario considered is a head-on (bow) collision against a flat, vertical, fully rigid plate.

The vessel considered for the study is a Panamax Bulk Carrier, since such a vessel type exhibits increased collision frequency, and the velocities examined will be strictly smaller than the service speed V_s (see for reference subsection 1.5.1).

The purpose of the analysis is to determine the damage evolution, extent and deformation patterns on the ship bow structure in a head-on collision, in order to evaluate the energy absorption capability and the maximum horizontal reaction forces exerted on the ship hull. This is assumed to be required on the context of a FSA, assessing the structural crashworthiness of the current bow design and examining possible cost-effective improvements (see for reference subsection 1.5.3). The method employed for this analysis will be the Finite Element Method (FEM), described in depth in Chapter 2.

Verification of present study's results

Verification of ship collision incidents directly through measurements and experimental procedures is difficult. Only a few full-scale collision tests have ever been conducted, and the costs for such setups is prohibitive. Additionally, the collision forces exerted on the bow exhibit considerable disparity with regard to different bow construction designs (Woisin (1976)). As a result, the present model results will be assessed for reliability through:

1. Comparison with simplified analytical methods, which have been constructed after experimental verification, and can thus be considered relatively accurate tools.

2. Careful consideration of state-of-the-art numerical procedures for modelling using FEA, including a comprehensive mesh-convergence study.

3. Comparison of observed deformation patterns with real-life incidents.

4. Application of sound engineering judgement and practice.

1.8 Summary of present work

In Chapter 1, the motivation behind the problem has been established, as well as its definition.

In Chapter 2, the various techniques utilized for FEA modelling using Abaqus/CAE are discussed. Special treatment on material plasticity and strain-rate effects are explained. The constructed meshes for the mesh convergence study are presented, as well as the various model interactions.

In Chapter 3, the results of the mesh convergence study are presented, in order to decide the most well-suited mesh for the problem. Following this choice, comprehensive results and damage descriptions are presented, for the low-speed (3 kn), the intermediate-speed (6 kn) and the high-speed (9 kn) collision scenarios. Emphasis is placed on the relative contribution of the bulb and the stem to the bow crushing process. Additionally, a comparison with deformation patterns of actual incidents in head-on collision is presented.

In Chapter 4, several simplified analytical methodologies are applied for the approximation of the force-displacement curves, mean crushing forces F_m, maximum crushing forces F_M and maximum penetration depths d_{max}. These methodologies range from subdivision of bow sections into idealized L-, T- and X-elements, to simple empirical formulae produced from experimental curve-fitting. A rather satisfactory agreement is observed, compared to the FEA results of the present study, indicating that the FEM modelling techniques applied are in the right direction.

Finally, in Chapter 5, the most important conclusions of the present study are summarized, and several recommendations for future research are proposed.

Chapter 2

Modelling bow collisions using FEA

2.1 Introduction to Finite Element modelling for ship structures

Ship structures and ship-shaped offshore installations have traditionally been analyzed and designed against prescriptive structural loads, utilizing a series of (well-established and widely accepted by the Naval Architecture community) rules and standards, at least for the better part of the last century. Classification Societies (non-governmental organizations, responsible for annually publishing these rules and standards, and ensuring their compliance) are assigned to each vessel, in order to classify their cargo carrying capacity and subsequent strength against various sea conditions and loads exerted on the ship hull.

As computing capacity has skyrocketed during the last few decades, the Nonlinear Finite Element Method (NLFEM) has gained popularity in the shipbuilding industry, in order to analyze complex marine structures under even more complex loads, with a satisfactory degree of uncertainty. Unlike hand calculations, semi-analytical or empirical methods, the NLFEM allows for strength assessment of arbitrary geometries, including a plethora of highly nonlinear phenomena, such as material plasticity, creep and strain-rate effects, and is an indispensable tool for Naval Architects, especially during novel designs, for which no prior experience has been recorded.

An important aspect to be highlighted is that the NLFEM approach allows for parametric trial-and-error of local scantlings, resulting in a strengthened structure only where required, leading to a much lighter, steel (and, thus, fuel) efficient structure, without sacrificing safety or strength.

However, these advantages are often compromised by extensive modelling efforts, as well as the increased computing capacity and memory storage required, aspects which need to be balanced in order to reach a solution that is both reliable and cost-effective.

In the following sections, the Finite Element Analysis (FEA) model of the ship bow structure utilized in the current approach will be thoroughly described. The selected modelling software is Abaqus/CAE and the designated solver is Abaqus/Explicit (products of Dassault Systemes Simulia^{TM}).

2.2 Geometric modelling

Following the remarks of section 1.7, the ship under consideration in the present study is a Panamax Bulk Carrier. Her general particulars are presented in Table 2.1:

$L_{BP} =$	186.00	m
$B =$	32.20	m
$D =$	18.90	m
$T =$	13.60	m
$C_B =$	0.854	$-$
$C_M =$	0.991	$-$
$C_P =$	0.862	$-$
$V_s =$	14.2	kn
$DWT =$	60629	t
$\Delta =$	71634	t
$LS =$	11005	t

Table 2.1: General Particulars of Panamax Bulk Carrier under consideration

It should be noted that the loading condition under consideration (implied through the values of draft, displacement and DWT of Table 2.1) is the full load condition, which represents the worst-case scenario for ship bow collisions, given that the displacement inertia, along with the vessel speed, governs the damage evolution.

Since the present thesis focuses on the damage description of the ship bow due to the loads exerted on the modelled structure (Internal Mechanics of collisions), rather than the resulting ship motion (External Mechanics of collisions), the geometry explicitly modelled in the Abaqus/CAE environment is limited to fore of the collision bulkhead. This is in accordance with the observations of section 1.4. The geometry considered comprises of all structural elements contributing to the local strength of the ship bow, which include:

- The Outer Shell of the ship bow hull (the bow, notably, having a blunt form)
- All Intermediate Decks up to the Upper Deck, with their respective longitudinal stiffeners (and openings, where significant)
- All strengthened Web Frame Supports, either at sides or at the decks
- The Double Bottom grillage structure
- Horizontal longitudinal stiffeners at the side shell
- Vertical pillars and girders, supporting adjacent decks
- Additional stiffeners on the CL section

The recommendations of DNV-RP-C208 (2019), Paragraph 4.4, were adopted for geometric modelling, which include the following remarks:

1. Small details of actual drawings need to be omitted. These include cut-outs and local reinforcements.
2. Local thickness addition because of weld material is excluded from the analysis.
3. Welded parts should be modelled as joint surfaces, in order to construct a continuous mesh during FEA.

For additional information regarding the scantlings considered for the present study, the reader is referred to Appendix A. The assembled geometry is presented in Figure 2.1:

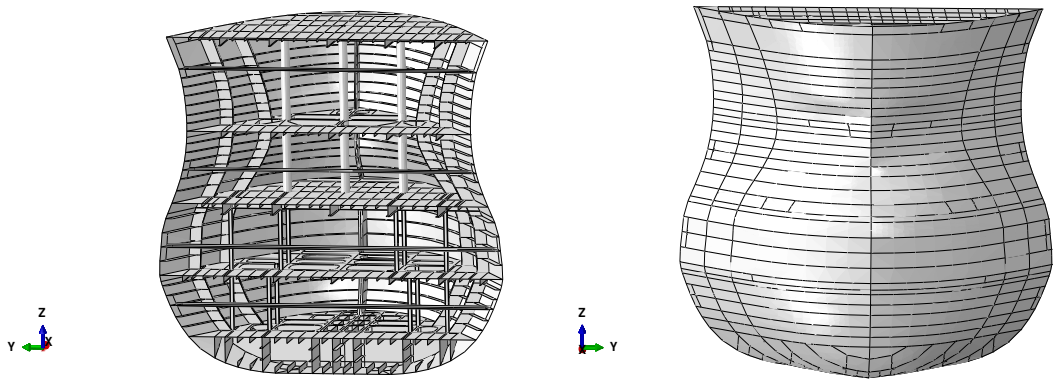

(a) Aft view of modelled bow geometry (b) Fore view of modelled bow geometry

Figure 2.1: Assembled bow geometry in Abaqus/CAE environment

2.3 Material Modelling

2.3.1 Materials of plate-members

The materials selected for the present FEA are:

1. Grade A shipbuilding steel
2. High-strength AH36 shipbuilding steel

The nominal properties assumed are retrieved from CSR (2023), Part 1, Chapter 3, Section 1, Paragraph 2, and are based on a 95% probability of exceedance, based on scatter of actual measurements (Storheim and Amdahl (2015)). Use of the lower-end of the spectrum of nominal properties produces conservative results from the analysis, i.e. the structure will be able to withstand somewhat higher loads than calculated.

Nominal properties of materials used				
	Grade A steel		AH36 steel	
Property	*Value*	*Units*	*Value*	*Units*
Density ρ	7.85E-09	t/mm^3	7.85E-09	t/mm^3
Young's Modulus E	206	GPa	206	GPa
Poisson's ratio ν	0.3	-	0.3	-
Yield stress σ_y	235	MPa	355	MPa
Ultimate tensile strength σ_{UTS}	400	MPa	490	MPa
Engineering fracture strain ε_f	0.22	-	0.21	-

Table 2.2: Nominal properties of materials used, according to CSR (2023)

The engineering fracture strain ϵ_f displays significant scatter, however the values of Table 2.2 are based on the minimum requirements of Lloyd's Register (2018).

2.3.2 Modelling of material plasticity

A material plastic behavior is characterized by its stress-strain curve beyond the elastic limit. Experimental tensile tests produce the "engineering" stress-strain curves (i.e. stresses and strains based on the initial cross-section and length of the test specimen).

However, FEA software require the input of "true" stress-strain curves for each material, meaning that stresses and strains are continuously updated based on the current specimen geometry, a difference which can be substantial in large deformation analyses (DNV-RP-C208 (2019)). A schematic, showcasing the differences between "engineering" stress-strain and "true" stress-strain curves, is depicted in Figure 2.2:

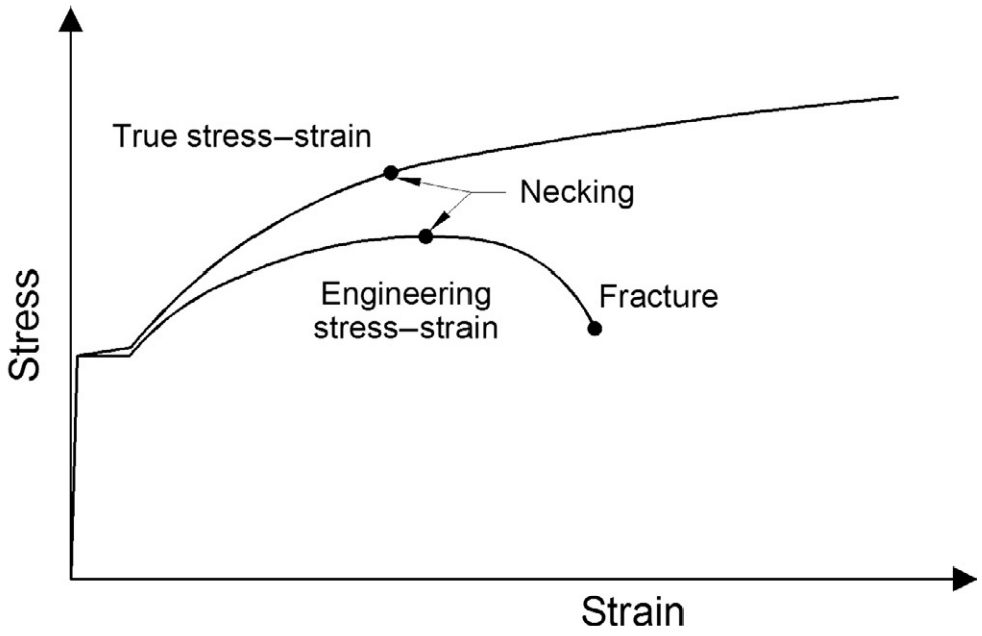

Figure 2.2: Illustration of "engineering" vs "true" stress-strain curves (reproduced from Pedersen et al. (2019))

"Engineering" stress-strain curves exhibit a clear necking point (in the form of the curve maximum, where the stress σ_{UTS} is obtained), beyond which the nominal force load does not further increase, whereas the formation of neck in the middle of the specimen is observed. Fracture occurs at the neck, after a short nominal load decrease, at a strain ϵ_f.

On the other hand, "true" stress-strain curves are continuously increasing, since the actual loading of the material in the specimen neck increases until the point of fracture, which is the curve maximum in this case.

In the present study, the true stress-strain curves were evaluated and exported to Abaqus/CAE based on the method of Liu et al. (2017), which requires only the material nominal properties of Table 2.2.

This method proposes a true stress vs true strain curve based on a power law with a yield plateau. As such, the following assumptions are made (Liu et al. (2017)):

1. A yield plateau, extending from the yield strain and up to $\epsilon_{true} = 0.006$ is assumed. The value of 0.006 is recommended based on the findings of Sever et al. (2011).

2. When $\epsilon_{true} \geq 0.006$, the true stress - true strain flow curve is characterized by a power law of the form $\sigma_{true} = K \cdot \epsilon_{true}^{n}$.

3. The strain hardening exponent n is equal to the engineering strain at the ultimate tensile strength ($n = \epsilon_{eng,UTS}$).

4. The power law curve is truncated, when the true strain is equal to the engineering fracture strain ϵ_f.

The latter assumption is based on the hypothesis that, for analyses on which compressive phenomena are dominant, the true stress - true strain curve should not significantly exceed the necking point of the engineering stress - engineering strain curve, since these curves are produced from tensile tests (instead of compressive tests), lest the stresses exhibited on the simulated structure will be overestimated (Paik (2007a)). Additionally, for such high values of compressive stresses, buckling phenomena are dominant, which are not captured by a true stress - true strain curve.

The aforementioned assumptions produce the following 2x2 system of equations for Grade A and AH36 steels, where the respective material parameters K and n are unknown:

$$\sigma_y = K \cdot 0.006^n \tag{2.1}$$

$$\sigma_{UTS} \cdot (1 + n) = K \cdot ln(1 + n)^n \tag{2.2}$$

The results of the calculation for materials Grade A and AH36 are shown in Table 2.3:

Calculation of power law coefficients				
	Grade A steel		AH36 steel	
	Value	*Units*	*Value*	*Units*
Coefficient K	684.25	MPa	752.31	MPa
Exponent n	0.2089	-	0.1468	-

Table 2.3: Power law coefficients calculations, based on the method of Liu et al. (2017)

The resulting material true stress - true strain curves for Grade A and AH36 steel are respectively depicted in Figures 2.3 and 2.4. The data points which correspond to Equations 2.1 and 2.2 (Yield plateau limit and Engineering Ultimate Tensile Stress point) are plotted with a blue marker.

In Abaqus/CAE, the true stress - true strain curve is extrapolated horizontally if the calculated strains are larger than the maximum strain, i.e. materials exhibit negligible additional resistance after the point of truncation ϵ_f (Abaqus 6.14 (2014)).

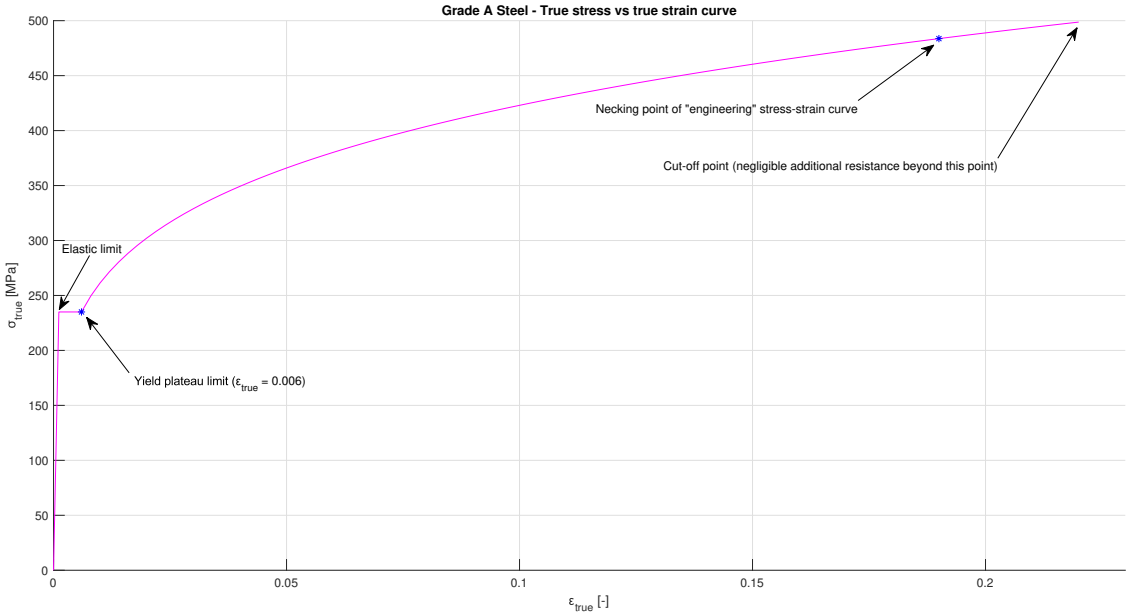

Figure 2.3: Grade A steel: True stress vs true strain curve imported to Abaqus/CAE

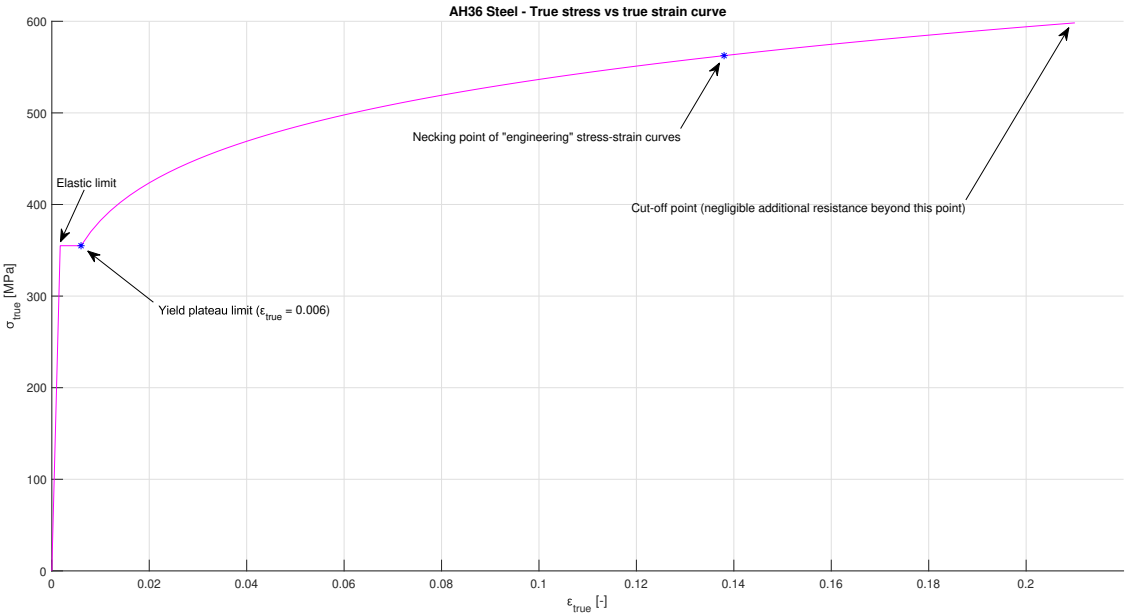

Figure 2.4: AH36 steel: True stress vs true strain curve imported to Abaqus/CAE

2.3.3 Strain-rate effects

Pre-modelling remarks

Since the modelled collision is governed mainly by inertia forces acting during a small time period (typically a few seconds), strain-rate effects are expected to heavily influence the results of the simulation.

It should, however, be noted, that inclusion of material strain-rate effects tends to overestimate the calculated forces and stresses on the structure, when compared to experimental measurements (see Figure 4 of Samuelides (2015), also Pedersen et al. (1993)), since strain-rate tends to increase the material strength but reduce the ductility it exhibits. As a result, it is not uncommon to ignore modelling these effects, in order to calculate conservative results, since designing against specific targeted loads, without inclusion of strain-rate effects on the response, leads to thicker scantlings (DNV-RP-C208 (2019)).

In the present study, strain-rate effects are considered an important factor, and both Grade A and AH36 steels are accordingly tuned for the FEA.

Modelling of strain-rate effects

When a structure is loaded dynamically with a strain rate $\dot{\epsilon}$, the material static yield stress $\sigma_{Y,s}$ increases to a dynamic value $\sigma_{Y,d}$. Perhaps the most well-known equation to model this effect was established by Cowper and Symonds (1957):

$$\frac{\sigma_{Y,d}}{\sigma_{Y,s}} = 1 + (\frac{\dot{\epsilon}}{D})^{\frac{1}{p}} \tag{2.3}$$

where D and p are constants, depending on the material.

For mild steels Cowper and Symonds (1957) suggest $D = 40.4$ and $q = 5$, while for high strength steels, Paik (2018) suggests $D = 3200$ and $q = 5$.

The effect of strain-rate on material yield stress described from Equation 2.3 is depicted on Figure 2.5. The ratio $\frac{\sigma_{Y,d}}{\sigma_{Y,s}}$ is asymptotically 1 for low strain-rates (static loading). It is also apparent from Figure 2.5 that the strain-rate effect on the yield stress is more prominent for mild steels, rather than high strength steels, effectively more than doubling the material yield strength on high loading rate events, such as blasts and explosions.

However, Equation 2.3 applies only regarding the material yield stress, whereas in the present FEA model, the phenomenon needs to be modelled in the complete range of the material (true) stress-strain curves. Additionally, it is a well-established fact that the strain-rate effect decreases with an increase on the material strain (i.e. it is more evident on the yield stress rather than the ultimate stress, see Liu et al. (2018b)), hence Equation 2.3 cannot be exploited for the complete range of strains on a true stress-true strain curve.

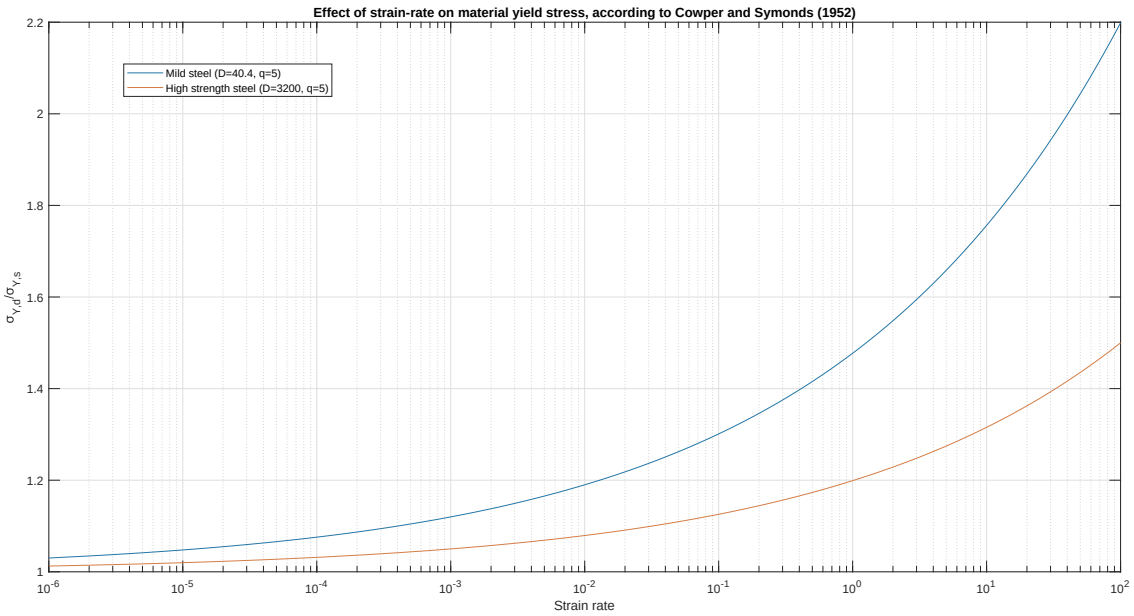

Figure 2.5: Effect of strain rate on yield stress according to Cowper and Symonds (1957)

To accurately capture this phenomenon, Jones (1989) suggested a linear dependency between the Cowper-Symonds denominator coefficient D and plastic strain ϵ_{pl}, as:

$$D = A + B \cdot \epsilon_{pl} \tag{2.4}$$

where A and B are material constants, computed as:

$$A = \frac{\epsilon_u \cdot D_y - \epsilon_y \cdot D_u}{\epsilon_u - \epsilon_y} \quad \text{and} \quad B = \frac{D_u - D_y}{\epsilon_u - \epsilon_y} \tag{2.5}$$

where the subscript "y" denotes the yield state, and the subscript "u" denotes the ultimate tensile strength state. For Grade A steel, the experimental values provided in Jones (2013) lead to the calculation results of Table 2.4:

Calculation of Jones (1989) coefficients for mild steel		
	Grade A steel	
Property	*Value*	*Units*
Yield strain ε_y	0.00114	-
Engineering strain at ultimate tensile stress ε_u	0.2089	-
Cowper-Symonds denominator coefficient at yield D_y	40.4	1/sec
Cowper-Symonds denominator coefficient at ultimate tensile strength D_u	230,000	1/sec
Material constant A	-1222.276	1/sec
Material constant B	1106856	1/sec

Table 2.4: Calculation of material constants A and B suggested by Jones (1989)

For high strength marine steel AH36, Choung (2013) recommended the following quadratic relation between the denominator coefficient D and plastic strain ϵ_{pl}:

$$D = 3.72 \cdot 10^5 + 9.4 \cdot 10^6 \cdot \epsilon_{pl}^2 \tag{2.6}$$

Through the use of Equations 2.4 (for Grade A steel) and 2.6 (for AH36 steel), the application of Equation 2.3 is possible for the complete range of strains on the true stress-true strain curves.

Since Abaqus/CAE accepts stress-strain curves for fixed strain rates (and interpolates for inbetween values, Abaqus 6.14 (2014)), the problem of uppermost expected strain rate arises. Ko et al. (2018) monitored the strains on a ship bow during a right-angled collision FEA simulation, in order to compute the maximum expected strain-rates as a function of the collision velocity; the proposed formula is the following linear expression:

$$\dot{\epsilon}_{max}\ [sec^{-1}] = 1.528 \cdot V\ [kn] - 0.686 \tag{2.7}$$

For the velocities examined in the present study (3 kn, 6 kn and 9 kn, see for reference subsection 2.6.2), the results of applying Equation 2.7 are presented in Table 2.5:

Calculation of maximum expected strain-rates		
based on the formula of Ko et. al (2017)		
	Maximum $\dot{\varepsilon}$	*Units*
Ship initial velocity V=3kn	3.898	1/sec
Ship initial velocity V=6kn	8.482	1/sec
Ship initial velocity V=9kn	13.066	1/sec

Table 2.5: Maximum expected strain-rate values (suggested by Ko et al. (2018))

It is deduced that the maximum strain rates expected for ship head-on collisions is in the order of 10-20 sec^{-1}. This is consistent with the findings of Chen et al. (2019) and Storheim and Amdahl (2015), who predicted a range of 3-15 sec^{-1} for the expected strain-rates during head-on collisions (although, notably, these ranges are mesh-dependent). Thus, truncation of data produced from application of Equations 2.3, 2.4 and 2.6 is applied at $\dot{\epsilon} = 30\ sec^{-1}$.

Contour plots of strain-rate effects on Grade A and AH36 true stress - true strain curves are presented in Figures 2.6 and 2.7, respectively:

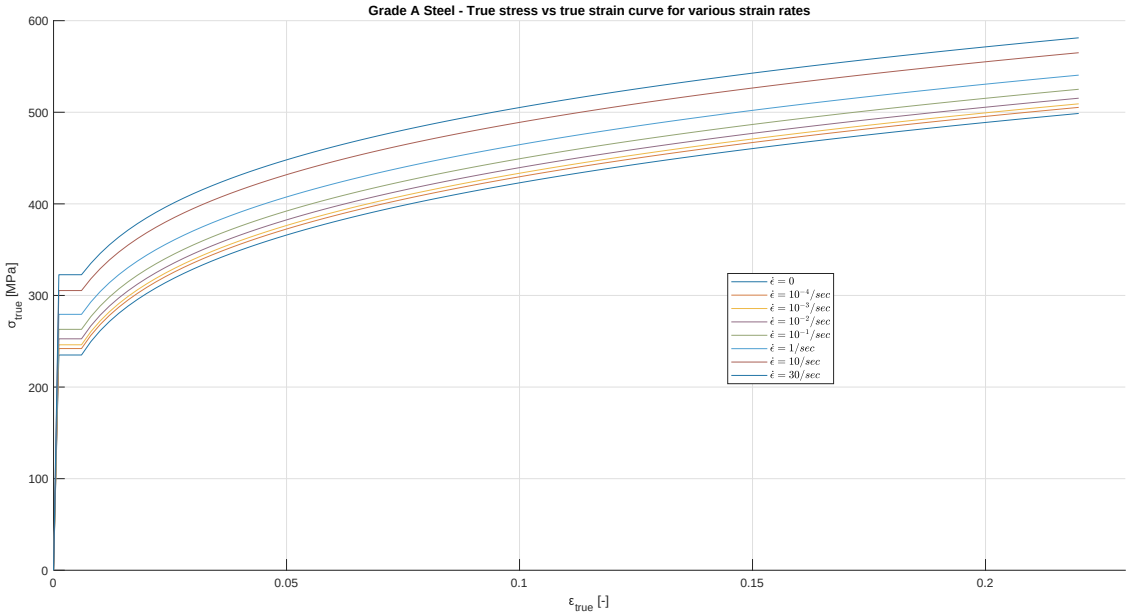

Figure 2.6: Effect of strain-rate on Grade A steel (as imported to Abaqus/CAE)

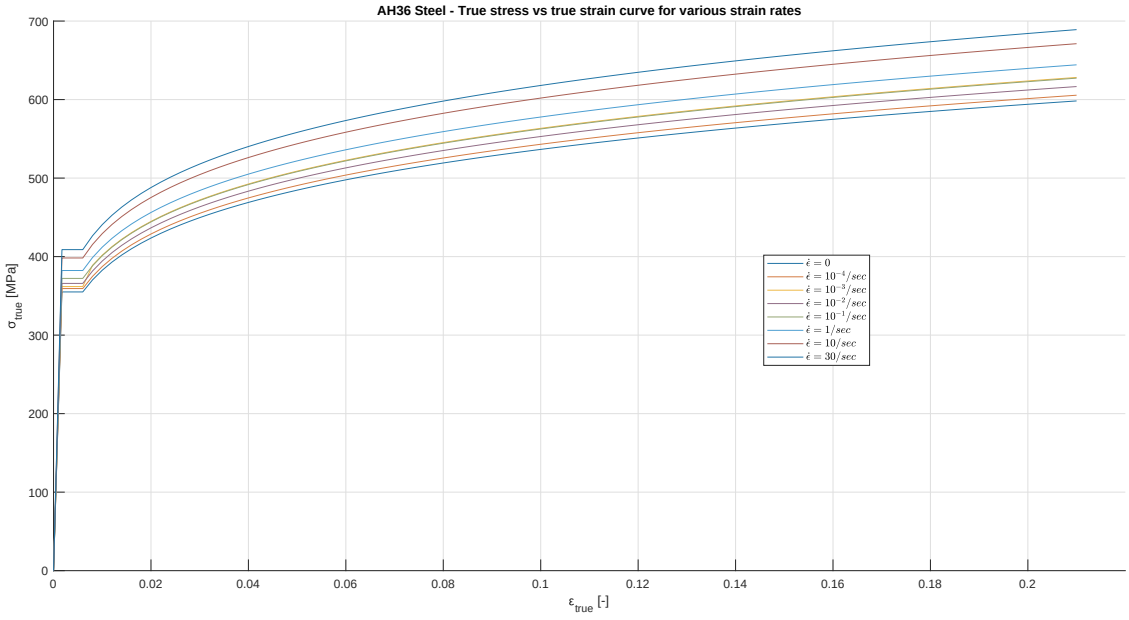

Figure 2.7: Effect of strain-rate on AH36 steel (as imported to Abaqus/CAE)

2.3.4 Thickness

For each plated element of the geometry modelled, the thickness assigned is based on the net scantling approach of CSR (2023). This means that a corrosion addition of $0.5 \cdot t_c$ is applied to the required member thicknesses, for strength assessment by use of Finite Elements, where t_c is the corrosion addition (for more information, the reader is referred to CSR (2023), Part 1, Chapter 3, Section 2, Table 1).

2.3.5 Failure criteria

An important factor affecting the results of ship collision simulations is the choice of an appropriate rupture/fracture criterion. It is well-established by the scientific community that the results heavily depend on the choice of the rupture criterion, so much so, that the choice of a different criterion may result not only in a different point of initiation of rupture, but rather a completely dissimilar force vs penetration curve (Samuelides (2015)).

Figure 2.8 depicts damage patterns exhibited on ship bows after head-on crushing; although significant deformations and folding is observed above the waterline, no extensive rupture is discerned; this is also consistent with the observations of section 1.3.

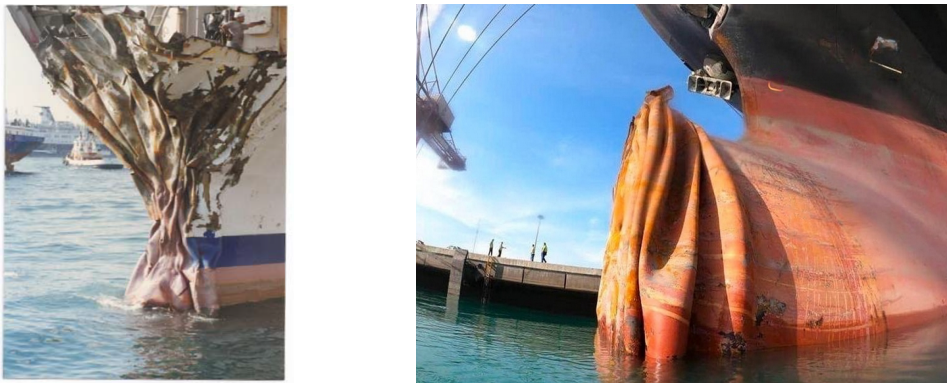

(a) Bow bulb and fore deck damage (reproduced from Samuelides (2009))

(b) Bow damage following a collision of containership M/V Basht (December 2021)

Figure 2.8: Typical bow crushing deformation patterns

The selection of appropriate failure criteria is a matter in need of further research and experimentation, since most criteria are developed on the basis of specific experimental tests and stress states (Ehlers (2011)), the vast majority of which are of a tensile nature. Tautz et al. (2013) conducted experiments on the collision behavior of a bow structure under quasi-static loading, and concluded that good agreement between FEA simulation and experiment is achieved, even if no fracture criteria is introduced, because it is a negligible failure mode.

As such, in the present modelling, no fracture/rupture initiation is modelled, an assumption valid when compressive phenomena are dominant, due to the abscence of thinning strains (Storheim et al. (2015)). The main source of damage will be extensive plastic strains and large deformations. Element failure will be exhibited in the form of complete loss of capability to exhibit further resistance, due to excessive plastic straining.

Nevertheless, the structural impact response is still expected to be accurately simulated using FEA, on the condition that the boundary conditions and the material properties are properly dealt with (Ko et al. (2018), Paik (2007b)).

2.4 Meshing considerations

2.4.1 Meshing technique

Because the bow structure modelled comprises of many structural elements welded together, the constructed meshes will be continuous at the joints (DNV-RP-C208 (2019), Paragraph 4.5.1).

2.4.2 Selection of element type

The following are in accordance with DNV-RP-C208 (2019), Paragraph 4.5.2.

General element category

In FEA problems of thin-walled structures, plate/shell elements are employed for discretization of the plated structure. For the longitudinal stiffeners, it is left to the user to decide whether they will be modelled as line (beam) elements, or plate/shell elements.

In the present study, the geometry will be discretized using plate/shell elements.

Element integration scheme

Full integration elements exhibit shear locking, meaning that the transverse shear stresses are overestimated, and the element displays excessive bending stiffness. On the other hand, although reduced integration elements are more cost-effective, they exhibit the problem of hourglassing (production of zero-strain deformation modes).

Nevertheless, since in collision analyses, computational time is of the essence, reduced integration elements are the preferred choice for explicit solvers. Hourglass energy is controlled with so-called artificial strain energy, which must be checked to be small enough, compared to the initial model energy (typically less than 5%).

Abaqus/CAE selected element

In accordance with the above remarks, for the constructed meshes, S4R/S3R shell elements from the Abaqus/Explicit library are employed, with second-order accuracy and five through-the-thickness integration points, utilizing Simpson's rule. The S3R elements will only be employed in case of abrupt geometric transitions, where S4R elements produced will be poorly shaped/distorted (quad-dominated mesh).

Additionally, the mesh will mainly be structured, where applicable for regularly shaped regions, and free for local irregular geometric regions.

It is noted that higher-order accuracy is employed, in order to provide more refined results, and allow for a relatively coarser mesh (Paik (2007a)).

2.4.3 Mesh sizes constructed

Literature review on mesh sizes for ship collision simulations

Appropriate element sizes for FEA collision simulations is heavily dependent on the accidental category simulated, the rupture criterion (if any), the dominant failure modes, and (ultimately) the experience of the analyst. DNV-RP-C208 (2019) recommends performing mesh convergence studies on the FEA models, in order to ensure reasonable stability of results.

Chen et al. (2019) simulated the experiments of quasi-static bow crushing performed by Yamada and Endo (2005) using various element sizes, ranging from 25 - 200 mm. The mesh convergence study (performed on the maximum crushing force) concluded that a reasonable compromise between accuracy and computational time is achieved, with a general mesh size of 50 mm.

Hareide et al. (2013) also observed that a fine mesh in the order of $3t$ (which corresponds to 50 mm for the present study) is able to accurately simulate the failure mechanisms of crushing of plates and stiffeners during grounding events.

Abubakar and Dow (2013) performed mesh convergence studies (with gradually more refined meshes, in the order of $6t$, $4t$ and $2.5t$), to simulate grounding experiments with FEA. They concluded that reliable force-displacement curves can be produced, even for the coarser mesh sizes examined.

From the aforementioned review, it is evident that an element size of about 50 mm (or denser) must be employed, in order to capture the main structural deformation modes and strain patterns. This choice is consistent with the observations of Samuelides (2009), who recommended an element size of at most 50 mm for the most strained areas, when simulating structural responses of ship structures with finite elements.

Iqbal and Shifan (2018) recommended the use of at least three shell elements along the stiffener web (in order to capture local variations of the stress patterns), and three shell elements for the plating between stiffeners. By employing a general element size of 50 mm, 3-4 elements along the stiffener web are generated, as well as more than 10 elements for the plating between the stiffeners.

Based on the aforementioned remarks, a mesh convergence study will be performed to assess the reliability of the simulation results, whilst minding the limitations on the computational resources available for the present thesis. On this context, three meshes will be constructed to discretize the assembled bow geometry:

1. A coarse mesh, with a general element size in the order of 200 mm ($\sim 15t$).

2. A fine mesh, with a general element size in the order of 100 mm ($\sim 7-8t$).

3. A very fine mesh, with a general element size in the order of 50 mm ($\sim 3-4t$).

Coarse mesh details

As a rough discretization, a mesh having a general element size of 200 mm ($\sim 15t$) was constructed, consisting of about 65,000 finite elements. Approximately 96.7% are S4R elements, while the rest 3.3% are S3R. The smallest stable time increment at the start of the simulation (see Section 2.7 for more details) is about $5 \cdot 10^{-6}$ sec. This mesh (henceforth termed "coarse mesh") is depicted in Figure 2.9:

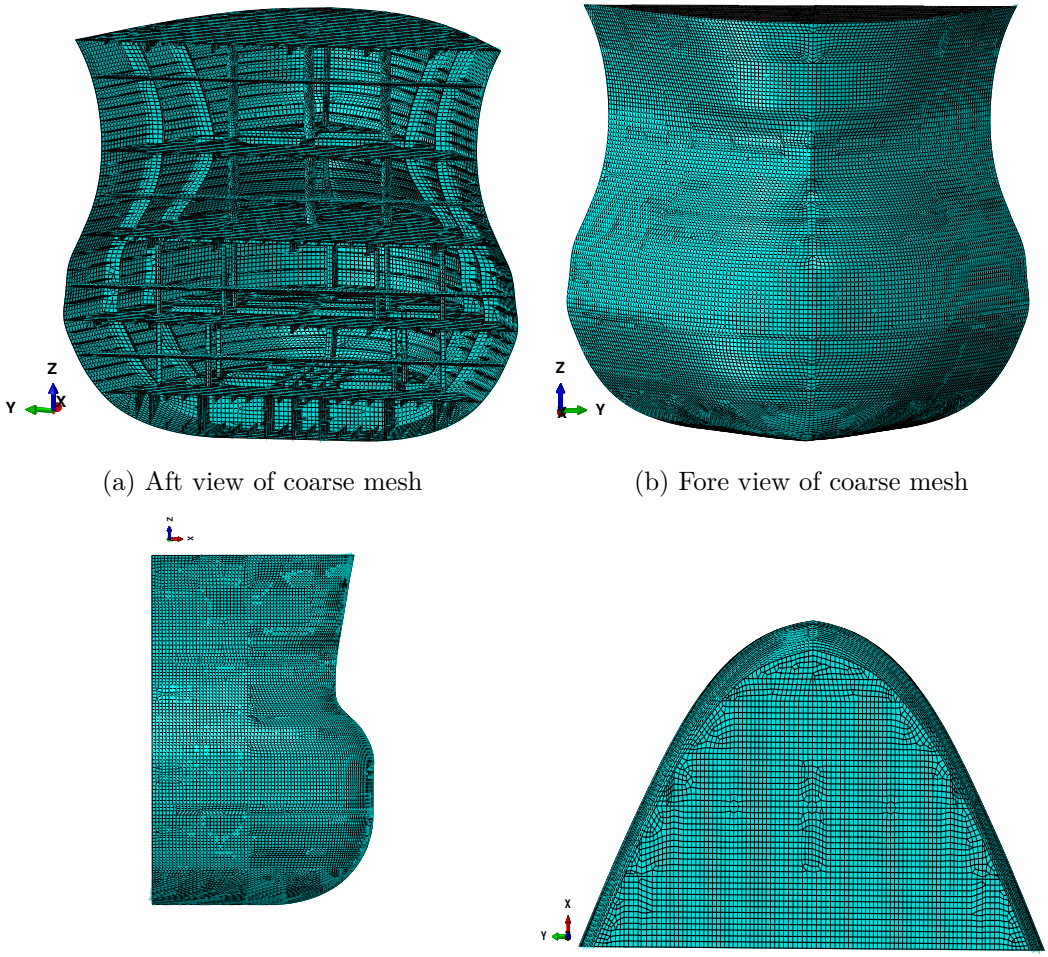

(a) Aft view of coarse mesh

(b) Fore view of coarse mesh

(c) Starboard view of coarse mesh

(d) Top view of coarse mesh

Figure 2.9: Coarse mesh ($\sim 15t$) constructed in Abaqus/CAE environment

Fine mesh details

As a relatively fine discretization, a mesh having a general element size of 100 mm in the area of interest ($\sim 7 - 8t$) was constructed. The geometry was divided into the following regions, in order to limit the computational effort required:

1. Coarse region, away from the collision front (aft of frame 223, where 200 mm element size was employed).

2. Intermediate/transition region (fore of frame 223 and aft of frame 227, where 150 mm element size was employed).

3. Collision front region (fore of frame 227, where 100 mm element size was employed).

This mesh consists of more than 130,000 finite elements. Approximately 98.2% are S4R

elements, while the rest 1.8% are S3R. The smallest stable time increment at the start of the simulation (see Section 2.7 for more details) is about $4.7 \cdot 10^{-6}$ sec. This mesh (henceforth termed "fine mesh") is depicted in Figure 2.10:

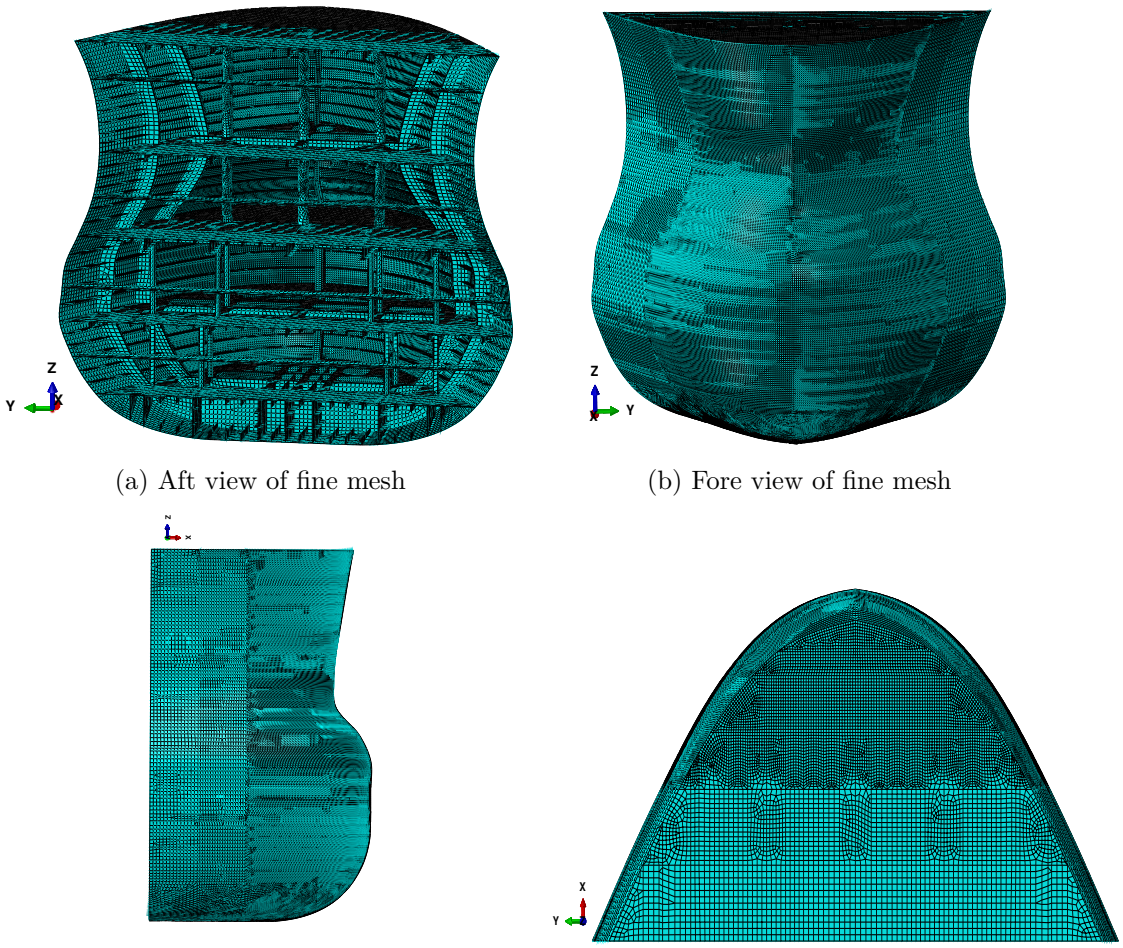

(a) Aft view of fine mesh

(b) Fore view of fine mesh

(c) Starboard view of fine mesh

(d) Top view of fine mesh

Figure 2.10: Fine mesh ($\sim 7-8t$) constructed in Abaqus/CAE environment

Very fine mesh details

Finally, a mesh having a general element size of 50 mm in the area of interest ($\sim 3-4t$) was constructed. The geometry was divided into the following regions, in order to limit the computational effort required:

1. Coarse region, away from the collision front (aft of frame 223, where 200 mm element size was employed).

2. Intermediate/transition region (fore of frame 223 and aft of frame 227, where 100 mm element size was employed).

3. Collision front region (fore of frame 227, where 50 mm element size was employed).

The final mesh consists of more than 400,000 finite elements. Approximately 98.5% are S4R elements, while the rest 1.5% are S3R. The smallest stable time increment at the start of the simulation (see Section 2.7 for more details) is about $2.6 \cdot 10^{-6}$ sec. This mesh (henceforth termed "very fine mesh") is depicted in Figure 2.11:

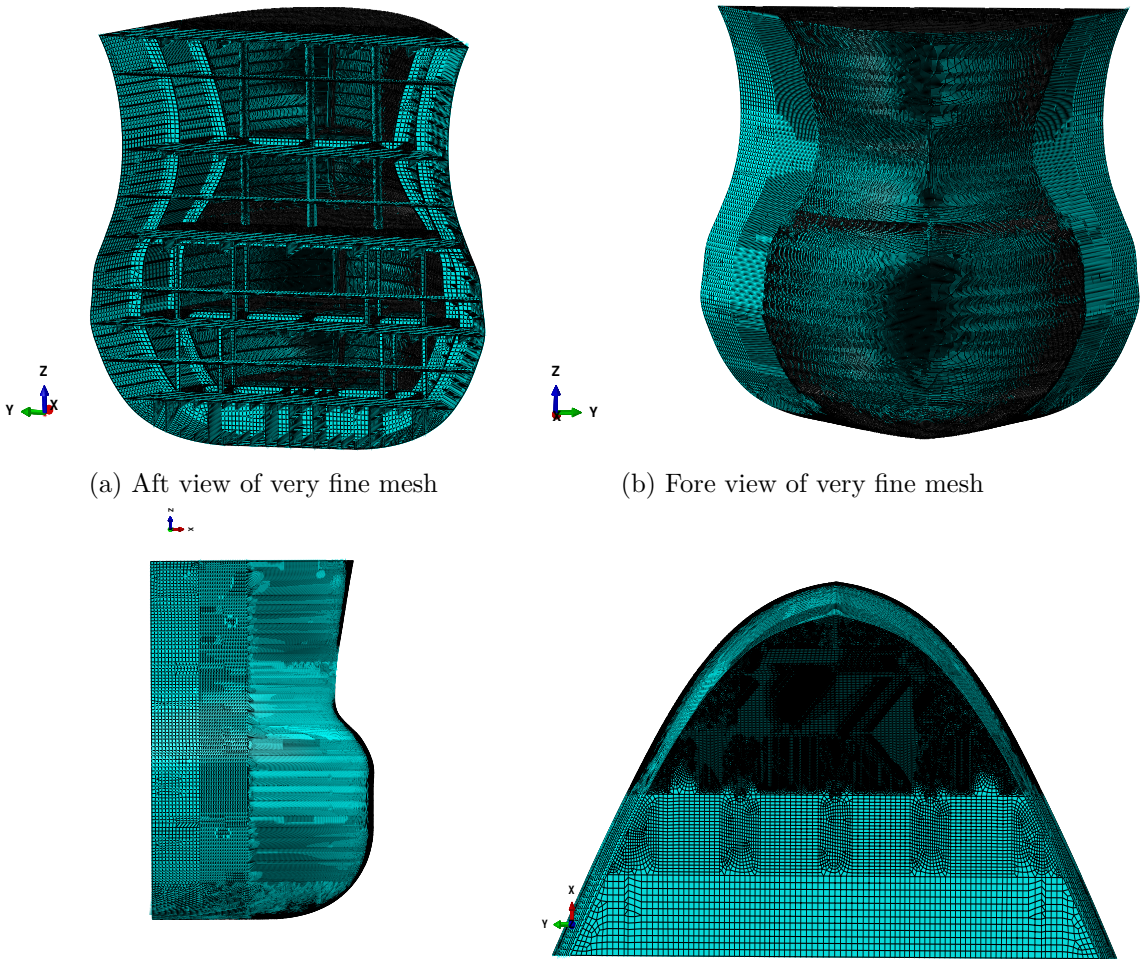

(a) Aft view of very fine mesh

(b) Fore view of very fine mesh

(c) Starboard view of very fine mesh

(d) Top view of very fine mesh

Figure 2.11: Very fine mesh ($\sim 3-4t$) constructed in Abaqus/CAE environment

The parameters associated with each of these meshes are presented in Table 2.6:

Mesh sizes parameters						
	Coarse Mesh (200 mm element size)		Fine Mesh (100 mm element size)		Very Fine Mesh (50 mm element size)	
Active Number of Elements:	66653		130577		410685	
Active Number of Nodes:	65236		128881		406387	
Active Number of Degrees of Freedom:	390093		771963		2436999	
		(%) of total elements		*(%) of total elements*		*(%) of total elements*
Number of Quad Elements (S4R):	64438	96.7	128212	98.2	404590	98.5
Number of Tri Elements (S34):	2212	3.3	2362	1.8	6089	1.5
Initial smallest stable time increment [sec]:	5.03E-06		4.72E-06		2.59E-06	

Table 2.6: Parameters of constructed meshes

2.5 Model interactions

The modelled and meshed bow geometry will be submitted to collision with a fully rigid, flat plate, having a 90° angle with the ship base plane, simulating an accidental load case against a vertical wall.

2.5.1 Constraints

On the above context, the following constraints are placed on the FEA model:

1. A reference point (RP) is created on top of the collision plate and kinematically coupled to it, with all degrees of freedom constrained. As such, the placement of fixed boundary condition on the whole plate can easily be achieved, simply by constraining the displacements of RP (see for reference subsection 2.6.1).

2. A reference point (RP-1) is created on the full ship's center of gravity (as calculated based on the loading condition, see subsection 2.5.4 for more information), and kinematically coupled to the aftmost section of the modelled bow, with all degrees of freedom constrained. This enables inclusion of the complete ship's mass on the simulation, as well as a rigid behavior of the aftmost bow section, simulating the rigid support of the collision bulkhead. The rigid idealization is valid, provided that no significant plastic deformations will occur around these boundaries, meaning that these boundaries must be far enough from the impact location, so as not to affect the damage evolution (Liu et al. (2018a)). However, this idealization tends to yield higher resistance forces than can be expected in continuous structures - thus being a non-conservative modelling addition (Yamada and Pedersen (2008)), and should be applied cautiously.

These constraints can also be observed in Figure 2.12. Reference points RP and RP-1 are discerned with a green color, and the rigid coupling constraint of RP-1 to the bow aftmost section (purple) is highlighted with a red color.

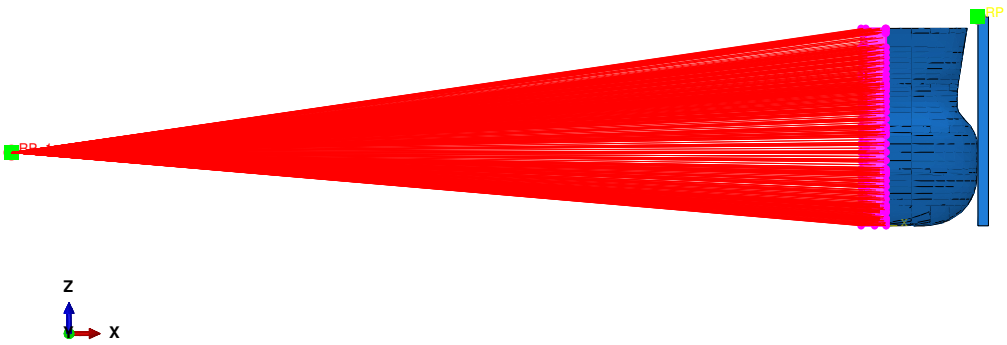

Figure 2.12: Starboard view of FEA model interactions in Abaqus/CAE environment

2.5.2 Contact interaction

A contact interaction for the FEA model is constructed (with enabled auto-contact, in case of large deformations causing self-contact of modelled geometry). This is mainly focused on the interaction between modelled bow geometry and flat collision plate.

1. For the tangential behavior, a penalty-based friction formulation with a friction coefficient $\mu = 0.3$ is assumed (Ehlers (2011)).

2. For the normal behavior (which is expected to dominate the simulation), a pressure-overclosure behavior must be selected, i.e. the application of pressure vs penetration depth. In the present study, "hard" contact formulation is enabled (see Figure 2.13). Such a formulation enforces zero penetration when the surfaces are in contact by use of a kinematic predictor/corrector contact algorithm, while transmitting any pressure between them (Abaqus 6.14 (2014)). Contact is strictly enabled when the clearance among the surfaces is zero.

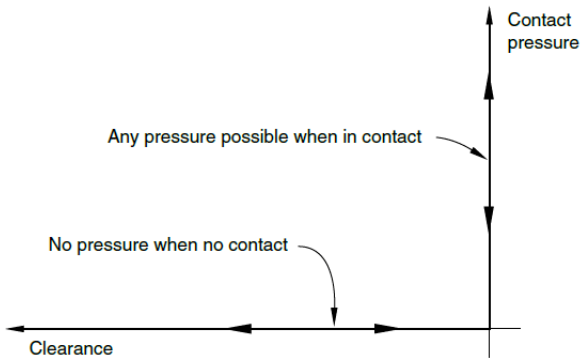

Figure 2.13: Schematic of "hard" pressure-overclosure formulation (Abaqus 6.14 (2014))

2.5.3 Effect of the surrounding water

Since the problem is assumed to be mainly governed by the ship inertia and normal contact forces, the additional hydrodynamic forces exerted on the ship hull during the collision (a heavily transient phenomenon with a small duration of at most a few seconds) can be assumed as sufficiently described by constant added masses.

These masses' constant values are equal to the frequency-dependent added masses, for infinite frequency. Reasonably accurate structural responses are obtained with this approximation (Pedersen et al. (2019)).

For the present study, the prevailing ship motion is the surge motion (in the longitudinal direction), hence an added mass coefficient m_{ax} should be determined (although, notably, being small compared to the ship mass). Petersen (1982) suggested the range:

$$0.02 \leq m_{ax} \leq 0.07 \tag{2.8}$$

where the value $m_{ax} = 0.05$ should be used, when lacking detailed information - a value also adopted in the present study.

Regarding the hydrostatic pressure exerted on the outer bow hull, it is assumed to be small compared to the inertial/contact pressure/hydrodynamic forces of the accidental event, and is thus not included in the current model.

2.5.4 Application of masses

A nodal mass is applied on reference point RP-1, in order to include the ship displacement inertia in the simulation. The relevant calculations are based on simple subtractions and equilibrium of mass moments, and are presented in Table 2.7.

It should also be noted that a nodal mass with extreme magnitudes of mass and rotational inertia (in the order of 10^{12} tonnes) has been assigned to reference point RP, in order to enforce correct collision dynamics, in which only the resulting ship motion will be simulated.

Calculations regarding ship's mass and COG			
Mass calculations			
Hydrostatic ship displacement [t]:	71634.1		
Added mass coefficient m_{ax} [-]:	0.05		
Ship displacement with added mass [t]:	75215.8		
Modelled geometry mass [t]:	208.4		
Nodal mass to be applied [t]:	75007.4		
COG calculations			
	x_{CG} [mm]	**y_{CG} [mm]**	**z_{CG} [mm]**
Ship CG Initial position (ship-fixed coordinate system):	95344	34	11105
Ship CG Initial position (Abaqus local coordinate system):	-81156	34	11105
Modelled geometry COG (Abaqus local coordinate system):	4738	-1	8594
RP-1 coordinates (Abaqus local coordinate system):	-81395	34	11112

Table 2.7: Calculations of added mass magnitude and location in Abaqus/CAE local CS

2.6 Boundary conditions and load application

2.6.1 Boundary condition

Following the remarks of subsection 2.5.1, a single boundary condition is applied on reference point RP, fully constraining its displacements and rotations. Considering the coupling constraint, the same (clamped) boundary condition will consequently be applied on the collision plate.

2.6.2 Load application

An initial, uniform, translational velocity V on the longitudinal direction is applied, in order to simulate the ship surge motion. The load cases to be examined in the present study (after evaluation of the mesh convergence study, resulting in an appropriate mesh size) are presented in Table 2.8:

Ship velocities considered for the present study				
	Initial speed V [kn]	**Initial speed V [m/sec]**	**% of service speed V_s**	**Initial kinetic energy [MJ]**
Low-speed collision	3	1.543	21%	89.54
Intermediate-speed collision	6	3.086	43%	358.31
High-speed collision	9	4.630	64%	806.23

Table 2.8: Collision cases examined in the present study

The magnitudes examined (as percentage of the service speed V_s) are considered representative of the candidate velocities of a ship sailing in restricted waterways.

Additionally, when modelling ship collision events, it is not uncommon to compensate for the rigid obstacle assumption, by a reduction of the examined velocities. This is

justified, since the real obstacle is expected to deform in some (difficult to measure) fashion, thus absorbing a fraction of the available kinetic energy to cause structural damage, and so, a reduction of this kinetic energy in idealized FEA modelling can be assumed, through a direct speed reduction.

2.7 Solving scheme

In crashworhiness analyses, the preferred choice for solving the FEA equations in the time-domain is the explicit integration scheme, which does not require matrix inversion or iterations, being much more computationally efficient for one time step, than implicit schemes (DNV-RP-C208 (2019), Paragraph 4.3.1). As such, an explicit discretization in the time-domain is employed hereafter, i.e. the designated solver of the FEA problem will be Abaqus/Explicit, a well-suited choice for short-duration, transient phenomena.

When employing explicit schemes, one should exercise caution, since they are stable, only provided that the time step is small enough (Courant-Friedrichs-Lewy condition). The expression of the CFL condition for structural analysis with shell elements is:

$$\Delta t \leq L_s \cdot \sqrt{\frac{\rho}{E}} \tag{2.9}$$

where ρ is the material density, E is the material Young's modulus and L_s is the characteristic element size. For analysis using common structural steels and mesh sizes in the order of 100 mm, the maximum time step is in the order of 10^{-6} sec, i.e. a couple million increments are required for a collision simulation lasting a few seconds.

Thus, it can be deduced that the smallest element governs the choice of the time step for explicit integration schemes. During the mesh convergence study, fine meshes are expected to require even finer discretization in the time-domain.

A remedy to this effect is introduced through the concept of mass scaling (DNV-RP-C208 (2019), Paragraph 4.3.4), which is artificial increase of the density of the smallest elements. However, this method is only applicable if inertia forces are small, i.e. the kinetic energy is small compared to the deformation energy, which is not the case in the present model, hence no mass scaling was introduced.

2.8 Final modelling remarks

Regarding the coupling effect of the hull-girder loads exerted on the hull structure as a result of the loading state (full load condition), they are not included in the current model. Since the structure modelled is located near the hull-girder fore end (which is free), they are considered negligible (Liu et al. (2018a)).

The focus on the present study is on the deformation patterns exerted on the fore part of the collision bulkhead. Thus, any and all deformations caused by the accidental event and located on and abaft the collision bulkhead, although present in any accidental event due to strain concentrations observed in deck-bulkhead junctions, can be considered irrelevant for the problem under consideration.

Chapter 3

Results of Finite Element Simulations

In this chapter, the results of the FEA simulations will be presented.

First, a mesh convergence study will be performed, comparing the performance of the coarse, fine, and very fine meshes constructed, as described in subsection 2.4.3.

Following the decision on the most suitable mesh size, analytical results for the examined initial velocities (namely, 3 kn, 6 kn and 9 kn) will be presented, as well as a comprehensive respective damage description. Some results of interest will, consequently, be assessed, when comparing the different initial collision velocity scenarios, and, additionally, the deformation patterns observed will be compared to actual head-on collision events.

3.1 Mesh convergence study

For the mesh convergence study, simulations were performed at the intermediate collision velocity (6 kn), utilizing the coarse, the fine and the very fine meshes. The criterion to terminate the simulation was either:

1. Nullification of available kinetic energy, or (when that was not computationally possible)

2. Observation of a local kinetic energy minimum, the absolute kinetic energy value being less than 30 kJ (i.e. less than 0.01 % of the initial kinetic energy).

3.1.1 Mesh convergence on the Force-Displacement curves

The most important resulting curve from a crashworthiness simulation is the force (exerted on the examined structure) vs penetration depth curve. For the bow collision simulation, the force examined is the horizontal component (F_x) of the total reaction force, and the penetration depth is the horizontal displacement d. From a general point of view, force-displacement curves exhibit a lesser sensitivity to mesh size than stress or strain patterns (Samuelides (2009)), thus they are examined for mesh convergence with an increased priority. Results are presented in Figure 3.1:

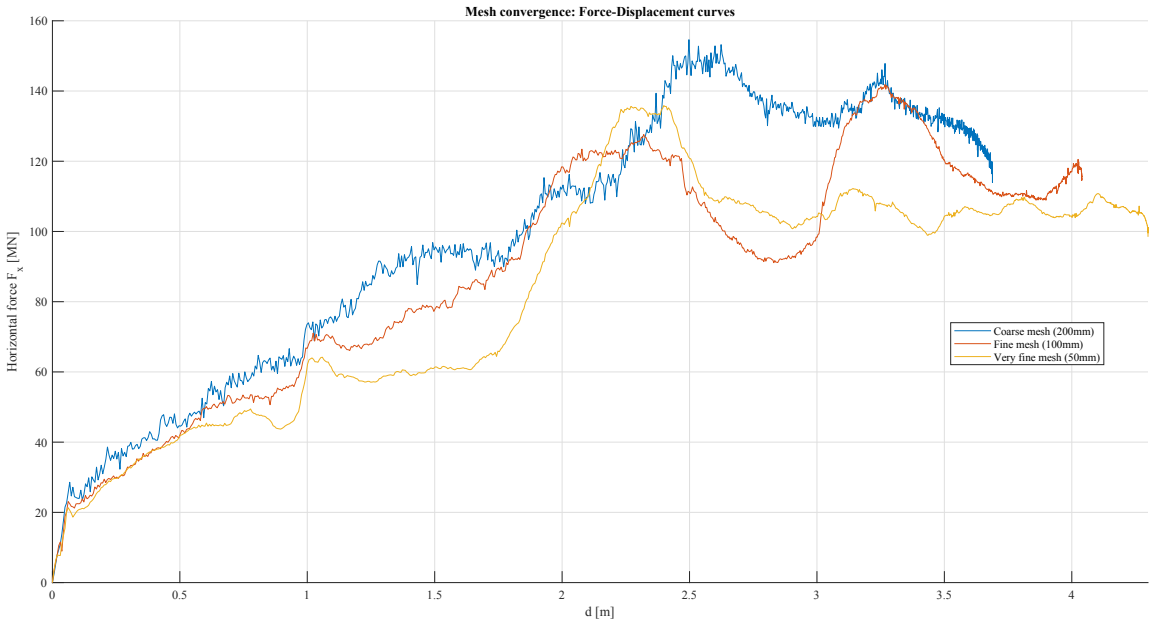

Figure 3.1: Force-displacement curves for various mesh sizes (6 kn simulation)

The resulting curves exhibit some degree of similar behavior, with an increasing trend around displacements of 1 m (when contact of the stem is first established) and 2 m (when full contact of the stem is established). However, their behavior diverges significantly after $d = 1\ m$, and they exhibit dissimilar maximum forces F_M, mean crushing forces F_m and collision durations (and, thus, maximum penetration depths). Ehlers et al. (2008) also reported inconsistencies in the trends of force-displacement curves, using mesh sizes of 100 mm, 50 mm and 25 mm, for a numerically simulated side collision experiment.

Additionally, it is noted that the coarse and fine meshes exhibit perturbations, most likely due to the successive failure of relatively bigger elements, with a more significant contribution to the total structural capacity of the bow.

3.1.2 Mesh convergence on the energy distribution curves

An additional result of interest is the relative distribution of the model energies (mainly consisting of kinetic energy E_K, internal energy $E_{internal}$ and frictional dissipation energy $E_{frictional}$) during the simulation, evaluated for the three mesh sizes constructed.

These curves are expected to exhibit similar trends among the mesh sizes, since they are (theoretically) computed based on integrations of the force-displacement curves, thus smoothening any dissimilarities. The results are presented in Figure 3.2:

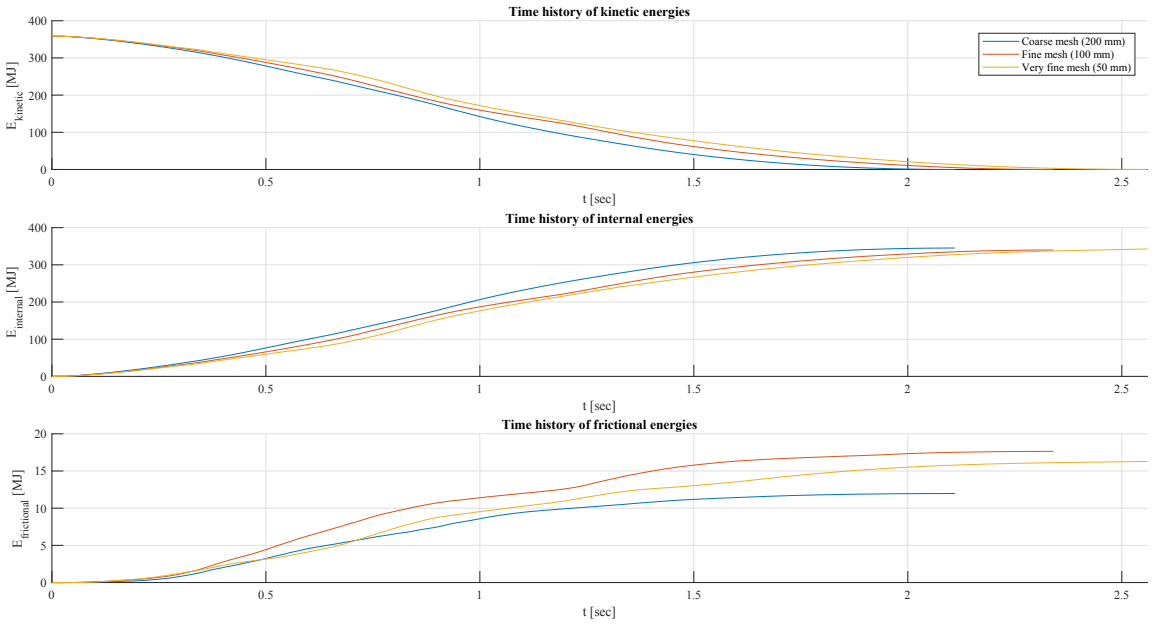

Figure 3.2: Energy distributions for various mesh sizes (6 kn simulation)

For the kinetic and internal energies, it is observed that the fine and very fine mesh curves lie very close, indicating some degree of convergence. However, it is noted that the very fine mesh curve for the frictional energy lies between the coarse and fine mesh curves. This may be attributed to the (slightly better, yet inadequate) description of the contact area evolution by the fine mesh, resulting in an overestimation of the frictional energy dissipated (although, notably, the frictional energy has a relatively low contribution of $\sim 15MJ/4\%$ to the total model energy).

3.1.3 Mesh convergence on critical collision parameters

The parameters whose convergence was examined by mesh refinement are the following:

- The duration of the 6 kn collision simulation (i.e. when the criteria established in the introduction of section 3.1 have been fulfilled).
- The maximum reaction force F_M exerted on the bow structure.
- The maximum penetration d_{max} achieved with the given initial ship velocity.
- The percentage of frictional energy dissipated during the collision (which was found to vary, following the remarks of subsection 3.1.2).

The results are presented in Figure 3.3:

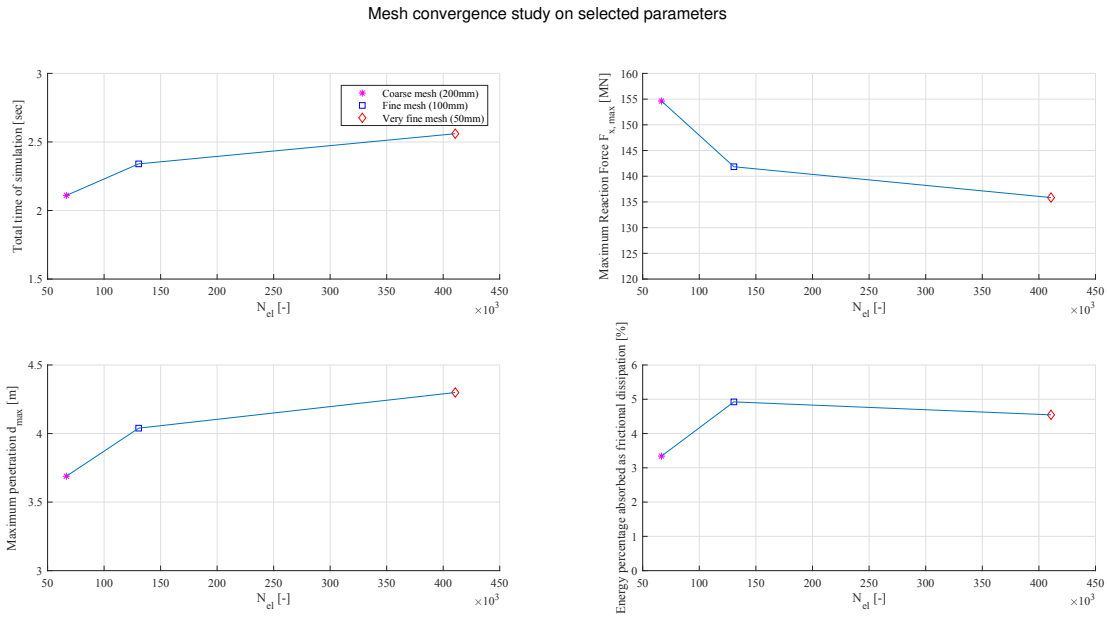

Figure 3.3: Results of mesh convergence study (6 kn simulation)

The respective divergence percentages, when comparing the fine and very fine mesh results, are:

- About 10% for the collision duration.
- About 4% for the maximum reaction force F_M.
- About 6% for the maximum penetration d_{max}.
- About 8% for the frictional energy percentage.

Although no definite convergence can be deduced based on the aforementioned divergence percentages, the achieved solution with the very fine mesh can be considered reliable enough, given the complexity of the phenomenon and the inherent modelling uncertainties.

3.1.4 Computational costs of mesh convergence study

In order to investigate the performance of each mesh size, the computational time required for each mesh to complete a simulation was measured. The results (in CPU·h) are presented in Figure 3.4:

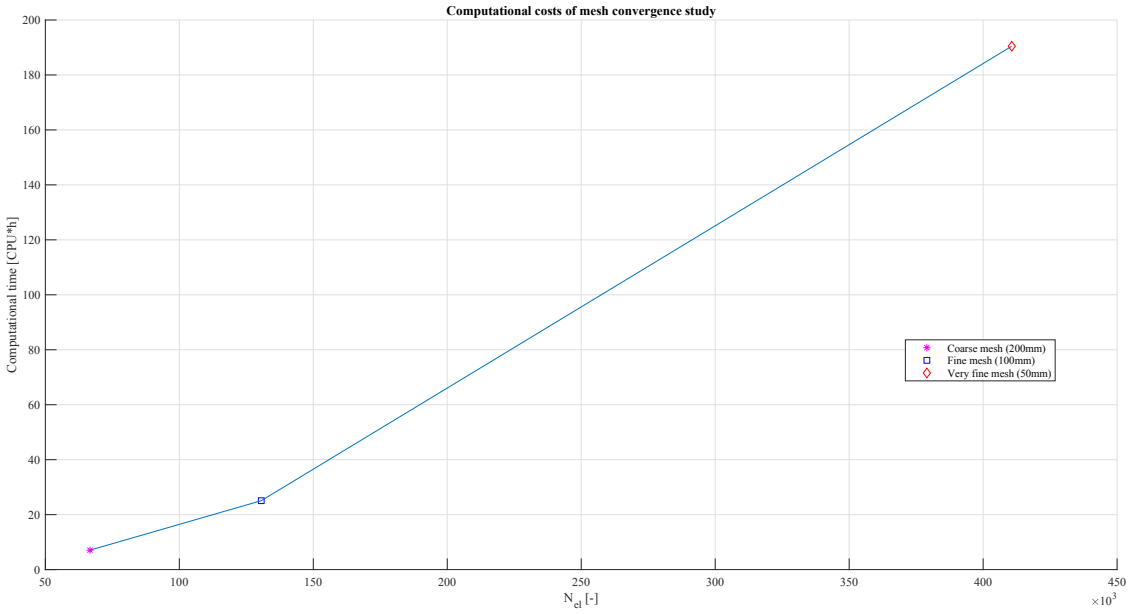

Figure 3.4: Computational time for each mesh size (6 kn simulation)

The computational time required appears to be approximately proportional to the number of elements of the FEA model, a remark well-established in the literature of crashworthiness analyses, when employing explicit solvers (Samuelides (2009)).

Considering the degree of convergence achieved (see subsection 3.1.3), the computational time required, and the limited resources available for the present thesis, a balance of reliability and cost-effectiveness is hereafter decided, and the following simulation results are computed with the very fine mesh.

This choice, although the most computationally expensive, allows the capture of the crushing failure mechanism more accurately, since the folded configuration requires relatively fine mesh sizes (Paik (2007a)).

3.2 Results of the intermediate speed simulation

3.2.1 Discussion on the force-displacement curve ($V = 6\ kn$)

The force-displacement curve for the 6 kn simulation is presented in Figure 3.5:

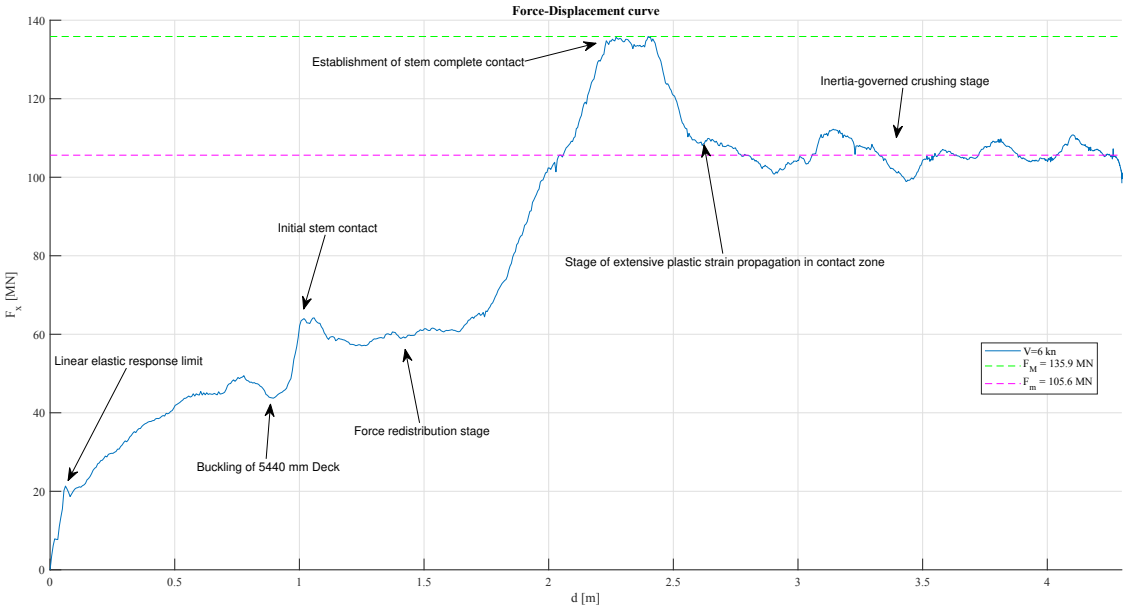

Figure 3.5: Force-displacement curve (6 kn simulation)

The following stages are noted:

1. The initial part of the F-d curve denotes the linear elastic response of the structure, without significant plastic strains. The reaction force is hereafter increased, with extensive plastic deformations, while the bulb is being crushed.

2. The first significant force drop occurs at $d \approx 0.85\ m$, when the buckling of the 5440 mm Deck signifies a loss on the load-bearing capacity of the bulb.

3. After that, a sharp increase in the collision force is observed, owing to the initiation of the stem contact.

4. On the following stage, the collision force remains almost constant, while a separate crushing behavior of the bulb and the stem is observed.

5. On the next stage, complete flattening of the bulb takes place, as well as extensive contact of the stem. This results in a progressive increase of the reaction force, up to its maximum value $F_M \approx 136\ MN$.

6. Consequently, a sharp drop from the maximum value F_M is observed, owing to propagation of plastic strains around the contact zone, whilst the bulb and the stem are simultaneously crushed. It is noted that all of the aforementioned stages occur in about 1 sec, i.e. 40% of the collision duration.

7. Finally, fluctuations of the reaction force around a mean value $F_m \approx 106\ MN$ are observed. This final stage lasts 1.5 sec (60% of the collision duration), and denotes the inertia-governed crushing of the bow structure, fore of the strengthened Web Frame 227. During this stage, the ship velocity is decreased in a linear fashion.

Comparing Figure 3.5 to the idealized Force-Displacement curve of Figure 1.9, a rather similar behavior is observed.

3.2.2 Distribution of energies ($V = 6\ kn$)

The distribution of energies during the 6 kn simulation is presented in Figure 3.6, as a percentage of the initial model energy of $E_k = 358.31\ MJ$:

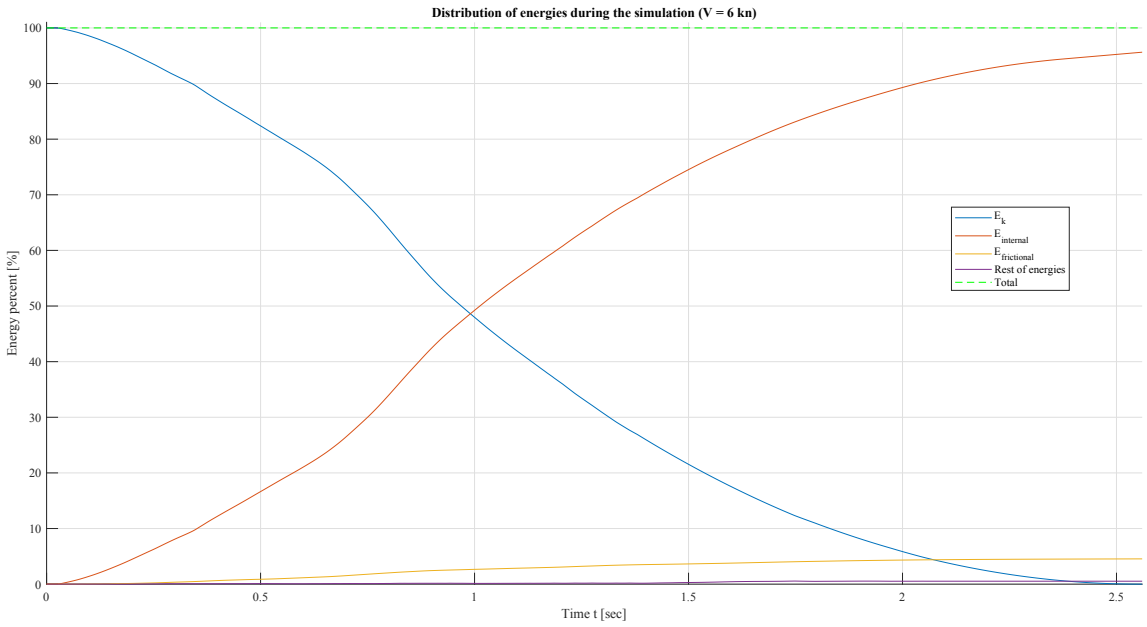

Figure 3.6: Distribution of model energies (6 kn simulation)

The following remarks can be made:

1. The available kinetic energy E_k to cause structural damage is dissipated mainly ($\approx 95\%$) by internal energy $E_{internal}$ (which consists of elastic strain energy, plastic

strain energy and artificial strain energy - the latter has been checked to be at most 4% of the initially available model energy).

2. The energy dissipated by friction is notably low ($\approx 4.5\%$ of the model energy).

3. Other energies, attributed to artificial stabilizing of Abaqus/Explicit through viscous damping, are negligible (less than 0.5%).

These rough energy distribution percentages are in accordance with results of Hareide et al. (2013) and Paik (2007a).

3.2.3 Damage description ($V = 6\ kn$)

The deformation pattern observed on the ship bow is presented in Figures 3.7-3.11. On these figures, an aft view of the bow geometry is presented on the left, and a fore view on the right (the collision plate has been removed from the fore views, for clarity):

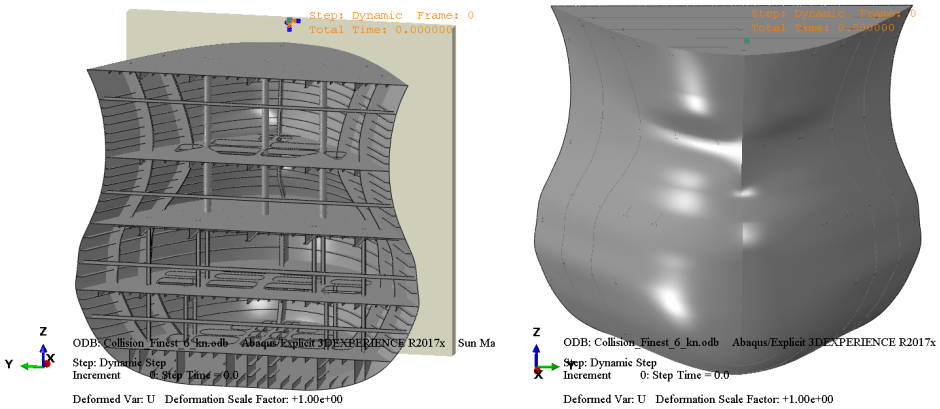

Figure 3.7: Initial position at t=0 (6 kn simulation)

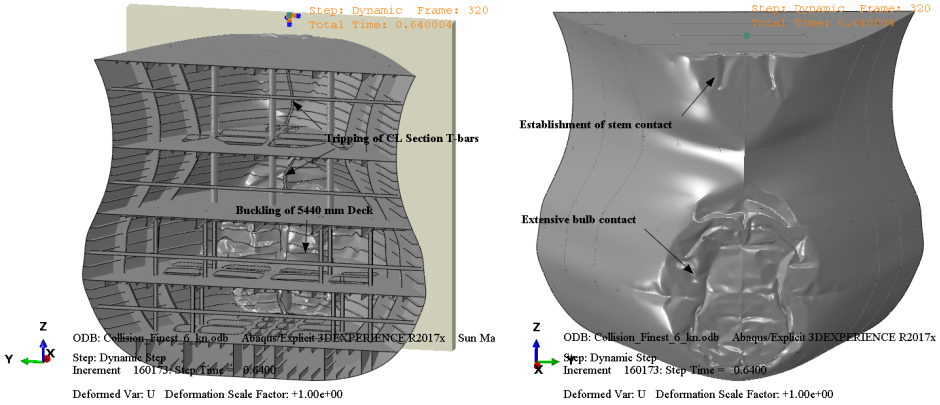

Figure 3.8: Deformation pattern at t=0.64 sec (6 kn simulation)

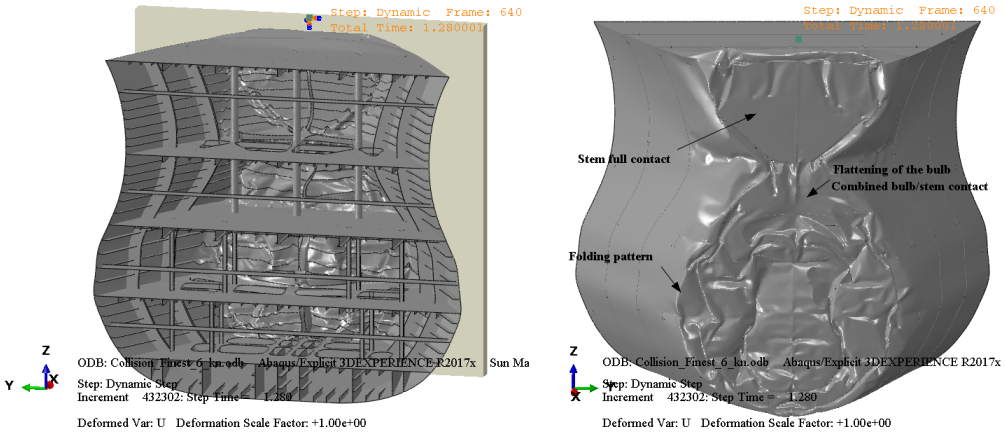

Figure 3.9: Deformation pattern at t=1.28 sec (6 kn simulation)

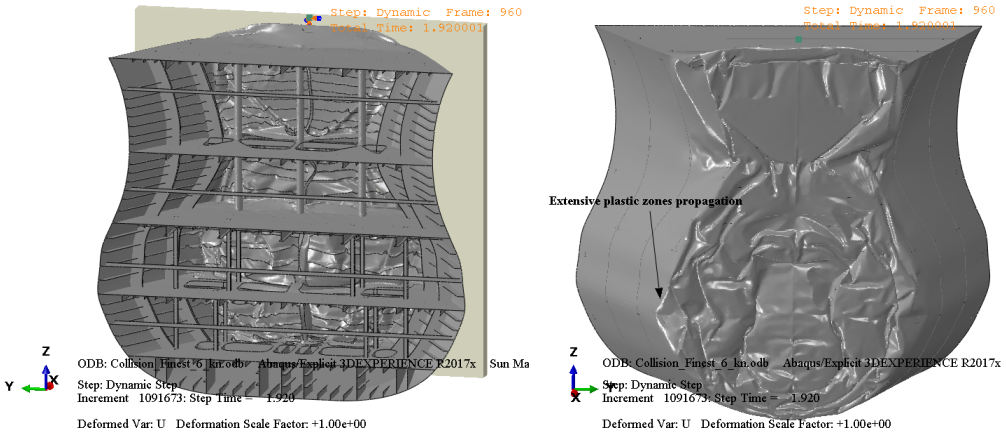

Figure 3.10: Deformation pattern at t=1.92 sec (6 kn simulation)

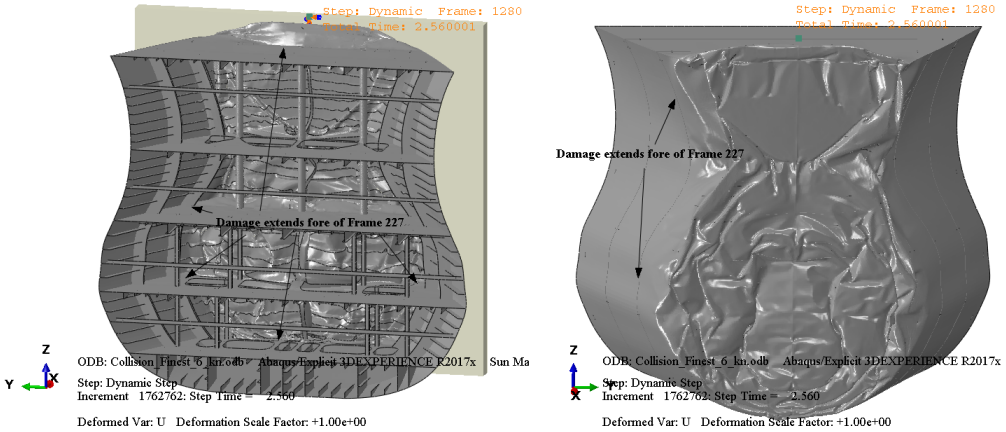

Figure 3.11: Final position at t=2.56 sec (6 kn simulation)

It is observed that the final deformation patterns extend only fore of the strengthened Web Frame 227, since it provides a rigid enough support to cause buckling/folding of the adjacent (fore) structure. The available energy is mainly dissipated either through bending of plastic hinge lines, or in-plane stretching of plate elements (Zhang et al. (2004)).

On the context of damage description, several contour plots of the equivalent plastic strain are depicted in Figures 3.12-3.15. The fringes' upper limit is the 0.22 cut-off value of the Grade A true stress - true strain curve:

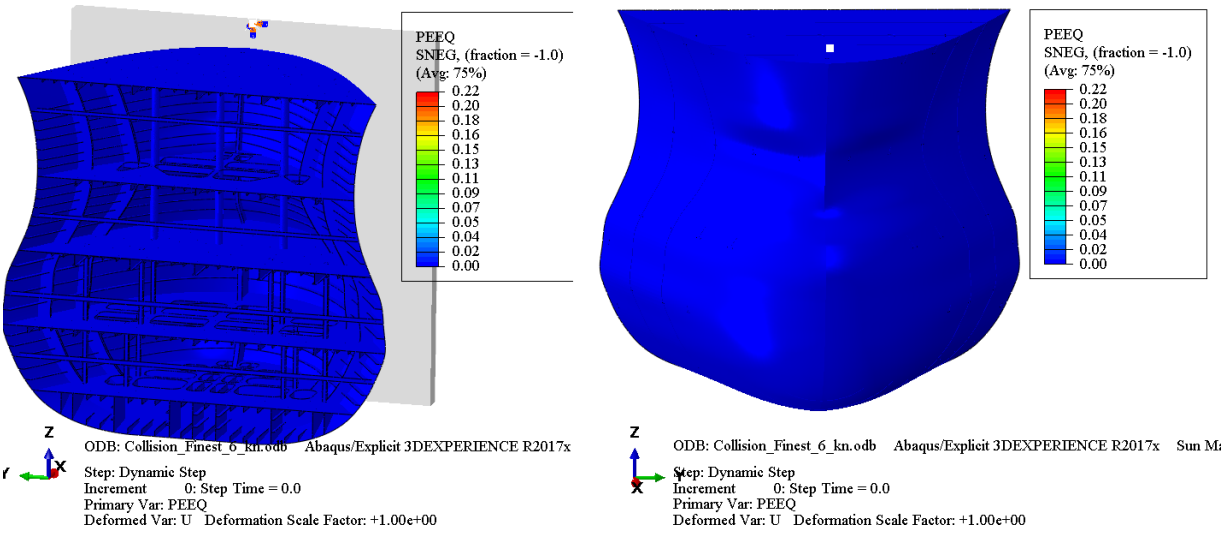

Figure 3.12: Initial undeformed position at t=0 (6 kn simulation)

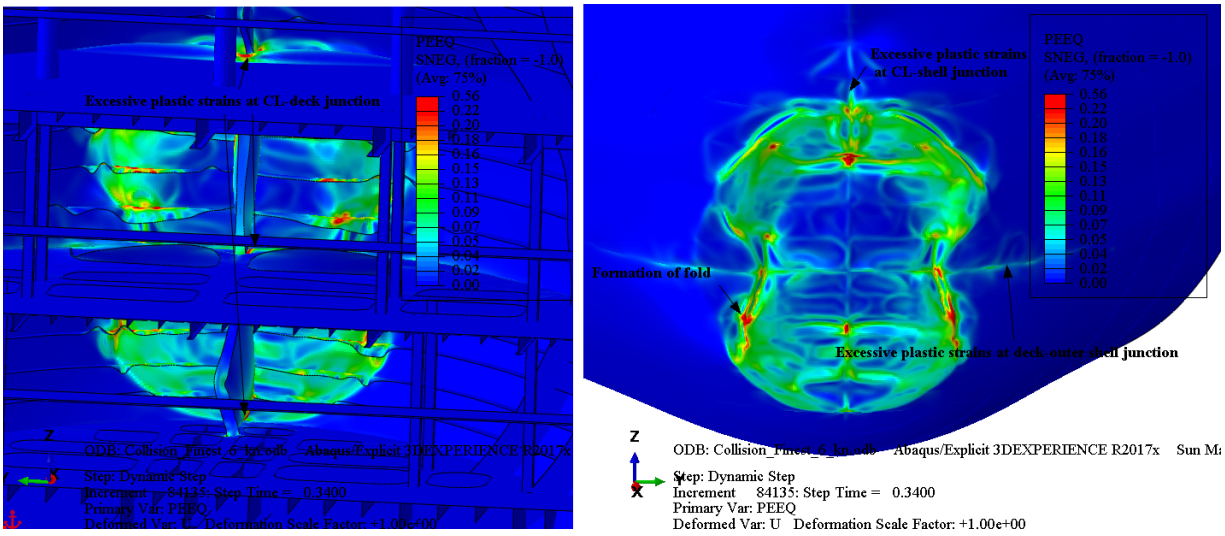

Figure 3.13: Distribution of equivalent plastic strains at t=0.34 sec (6 kn simulation)

Figure 3.13 depicts the damage distribution prior to initiation of stem contact. A zoomed screenshot of the bulb aft view is depicted on the left (Decks 9520 mm - 5440 mm - Tank Top), while a zoomed screenshot of the bulb fore view is depicted on the right, noting the areas of plastic strain concentrations. Several extensive plastic zones of limited equivalent plastic strain value are observed, which can be attributed to the yield plateau of the material modelling (Storheim and Amdahl (2015)).

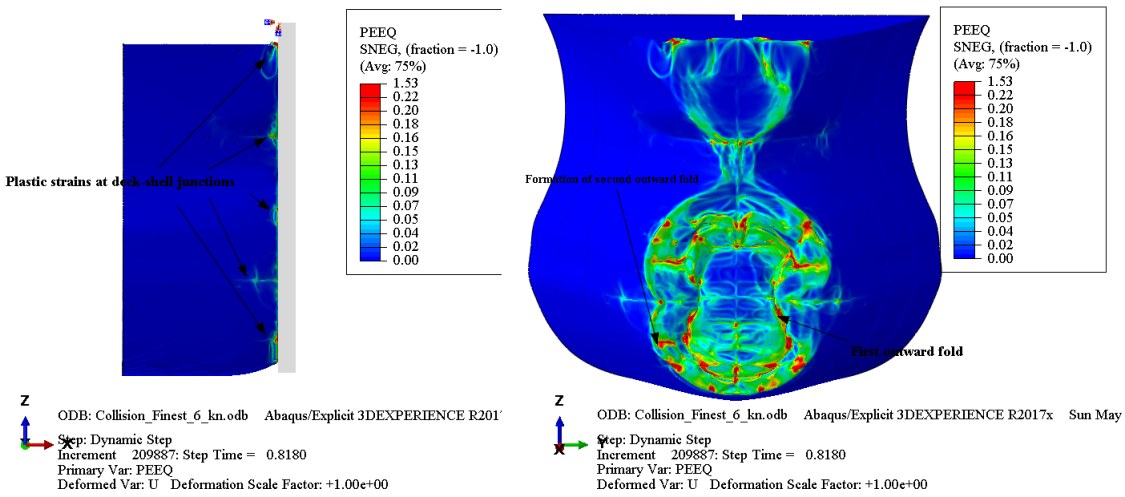

Figure 3.14: Distribution of equivalent plastic strains at t=0.82 sec (6 kn simulation)

Figure 3.14 depicts the damage distribution at the moment of maximum force F_M (t=0.82 sec). A starboard view of the bow structure is depicted on the left, while a fore view is depicted on the right, noting the areas of plastic strain concentrations and the formation of folding patterns.

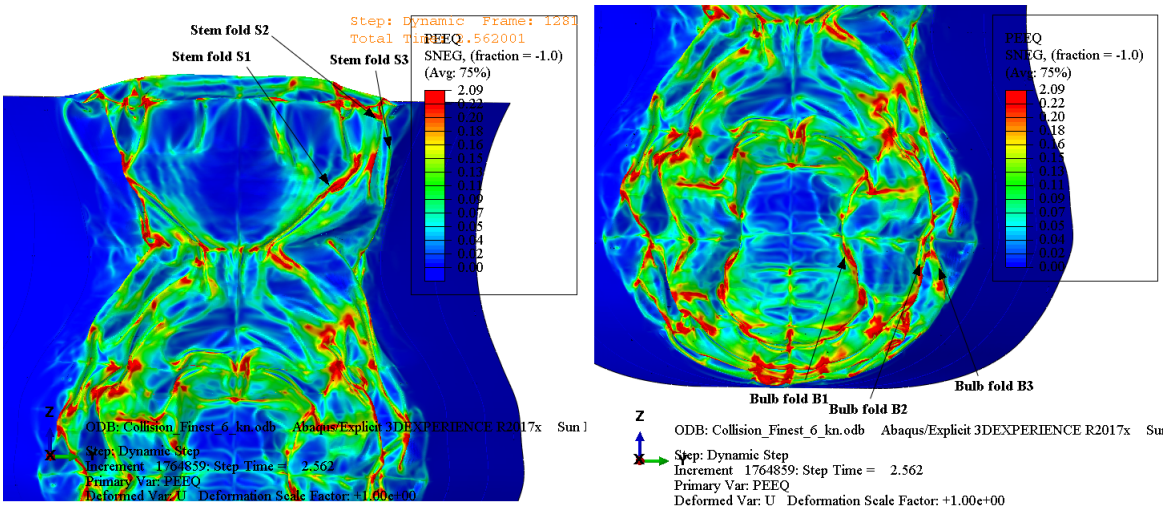

Figure 3.15: Distribution of equivalent plastic strains at t=2.56 sec (6 kn simulation)

Finally, Figure 3.15 depicts the final damage distribution at the end of the collision simulation (t=2.56 sec). A zoomed view of the stem is depicted on the left, while a zoomed view of the bulb is depicted on the right, noting the final folding patterns observed. It is noted that three clear folds are observed on the stem (S1, S2 and S3) and three more on the bulb (B1, B2 and B3), of which the S2-B2 and S3-B3, respectively, are interconnected. All folds are located fore of the strengthened Web Frame 227.

3.3 Results of the high-speed simulation

3.3.1 Discussion on the force-displacement curve ($V = 9\ kn$)

The force-displacement curve for the 9 kn simulation is presented in Figure 3.16:

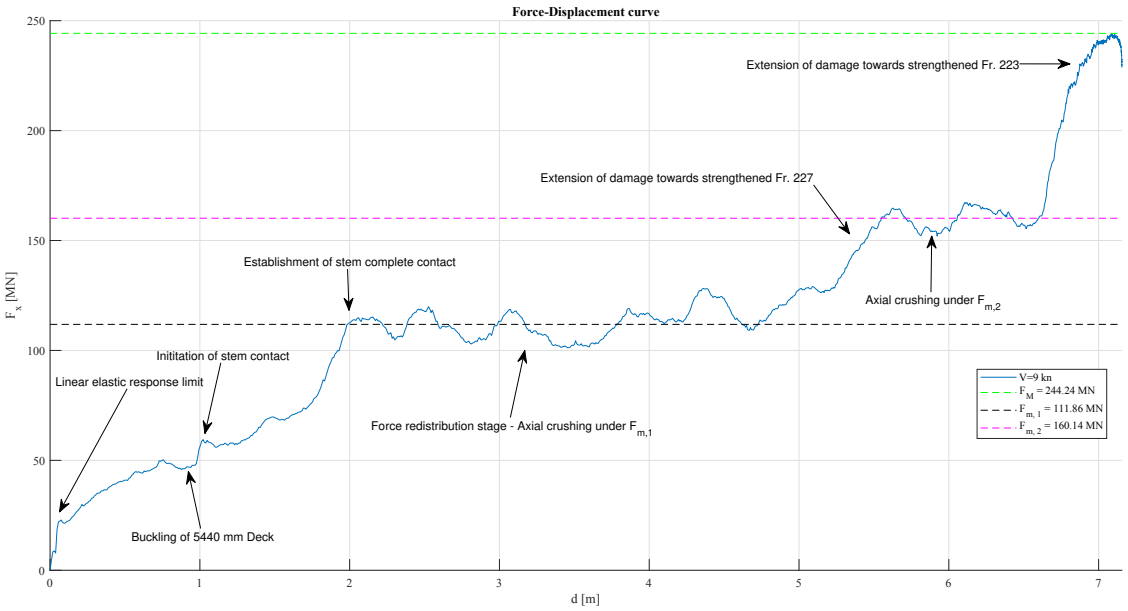

Figure 3.16: Force-displacement curve (9 kn simulation)

The following stages are noted:

1. The initial part of the F-d curve denotes the linear elastic response of the structure. Following that, crushing of the bulb occurs.

2. Buckling of the 5440 mm Deck, yet again, signifies a loss on the load-bearing capacity of the bulb.

3. After that, initiation of stem contact at about $d = 1\ m$ occurs.

4. Unlike the 6 kn simulation, the following stage is characterized by a gradual increase of the reaction force, denoting a force redistribution among the bulb and the stem. This may be attributed to the larger velocity of the bow structure in this simulation.

5. When contact of the stem is fully established, axial crushing of the structure fore of the strengthened Web Frame 227 occurs (the bulb and the stem behaving as a single structure), under a mean load $F_{m,1} \approx 112\ MN$.

6. After this crushing stage, a gradual increase on the reaction force is observed, due to the damage extension towards and on the strengthened Web Frame 227, effectively activating more elements for the crushing process.

7. Following that, fluctuations of the reaction force around a mean value $F_{m,2} \approx 160\ MN$ are observed, whilst the damage extends aft of Frame 227.

8. Finally, a sharp increase on the reaction force is observed during the final 0.7 sec (28%) of the simulation, owing to the damage extension towards the strengthened Web Frame 223. The simulation stops at a maximum penetration $d_{max} = 7.16$ m, near which it also exhibits its maximum reaction force $F_M \approx 244MN$.

As noted, two mean forces $F_{m,1}$ and $F_{m,2}$ can be distinguished, due to the engagement of different elements (fore and aft, respectively, of Frame 227) in the crushing process.

3.3.2 Distribution of energies ($V = 9\ kn$)

The distribution of energies during the 9 kn simulation is presented in Figure 3.17, as a percentage of the initial model energy of $E_k = 806.23\ MJ$:

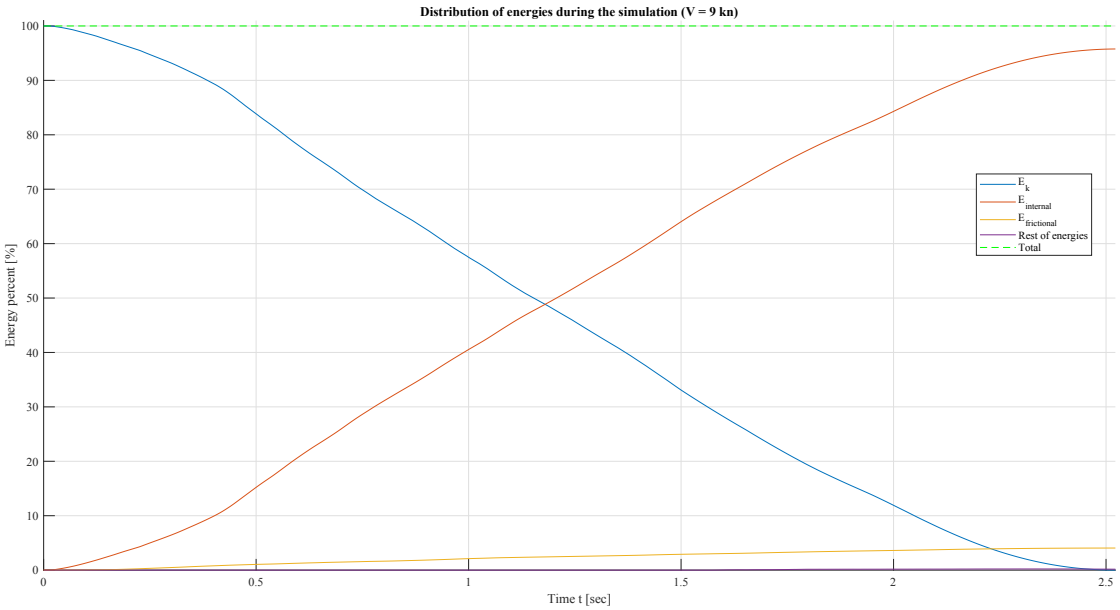

Figure 3.17: Distribution of model energies (9 kn simulation)

The following remarks can be made:

1. The available kinetic energy E_k to cause structural damage is dissipated mainly (more than 96%) by internal energy $E_{internal}$ (the artificial strain energy has been checked to be at most 5% of the initially available model energy).

2. The energy percentage dissipated by friction is even smaller than the 6 kn simulation ($\approx$ 4% of the model energy).

3. The rest of the model energies are negligible (less than 0.2%).

3.3.3 Damage description ($V = 9\ kn$)

The deformation pattern observed on the ship bow is presented in Figures 3.18-3.22. On these figures, an aft view of the bow geometry is presented on the left, and a fore view on the right (the collision plate has been removed from the fore views, for clarity):

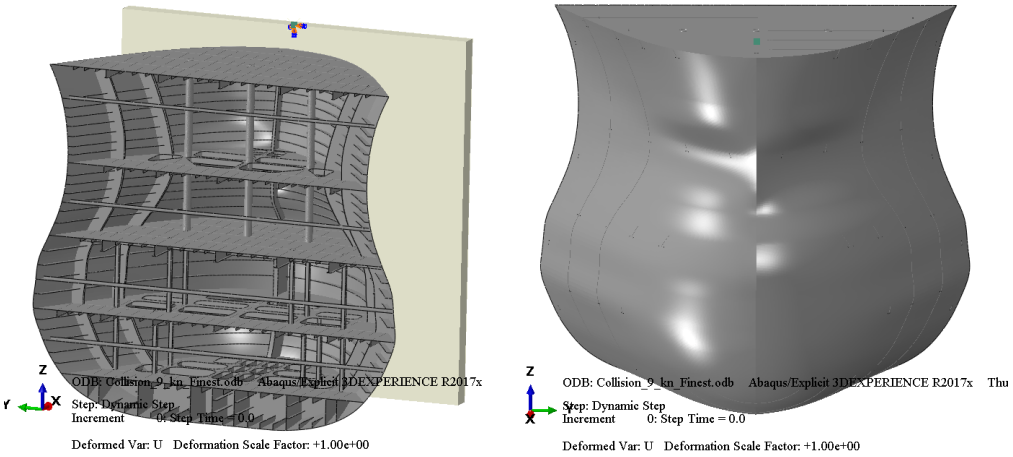

Figure 3.18: Initial position at t=0 (9 kn simulation)

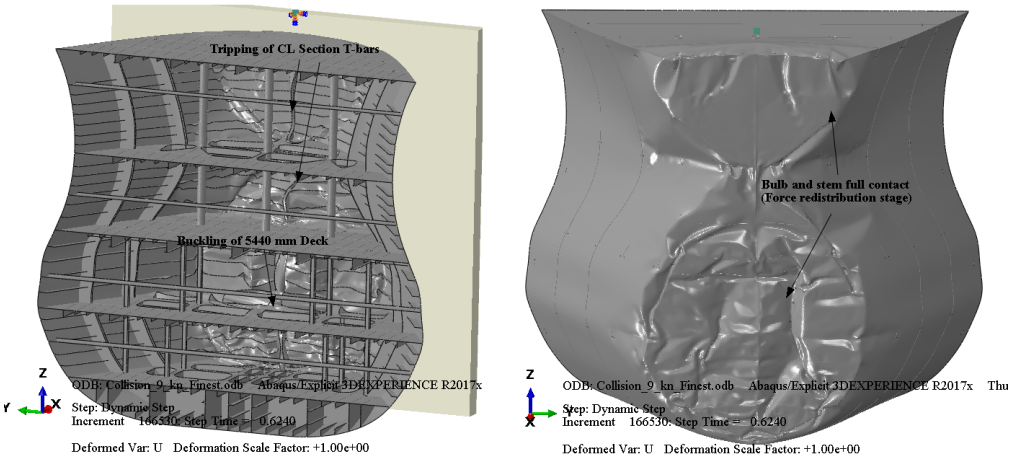

Figure 3.19: Deformation pattern at t=0.624 sec (9 kn simulation)

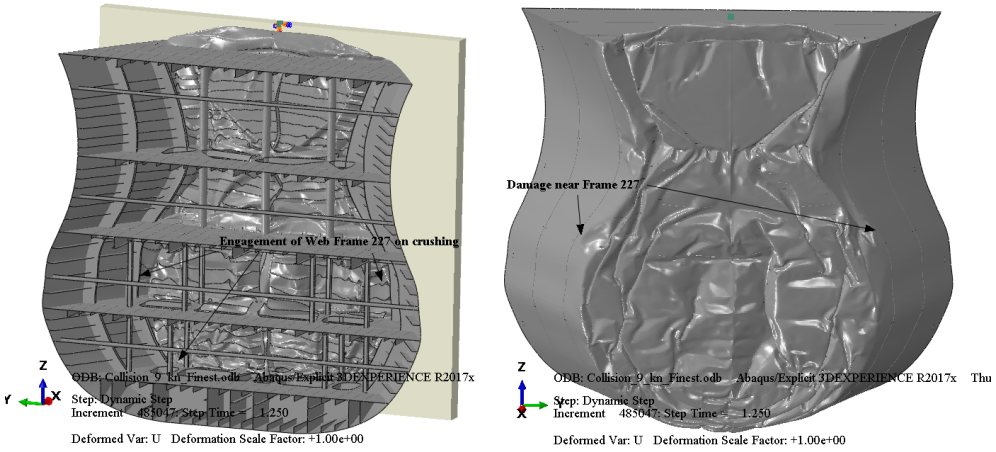

Figure 3.20: Deformation pattern at t=1.25 sec (9 kn simulation)

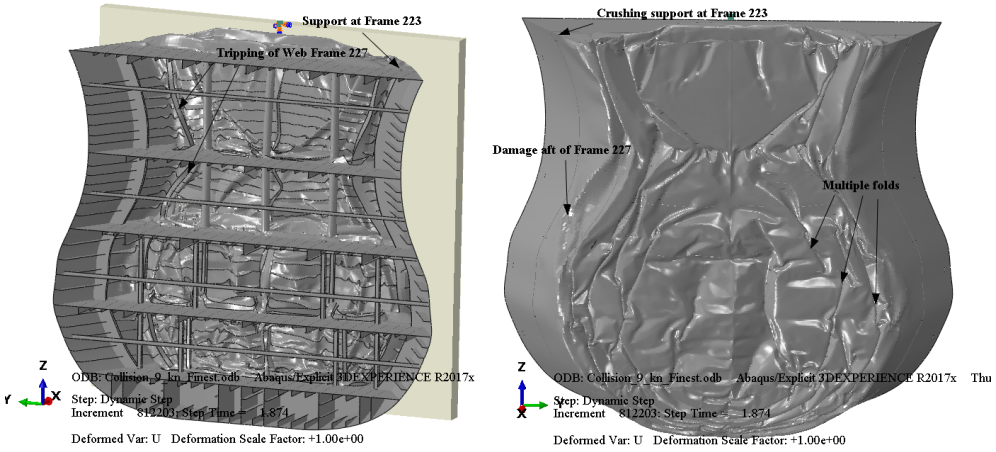

Figure 3.21: Deformation pattern at t=1.874 sec (9 kn simulation)

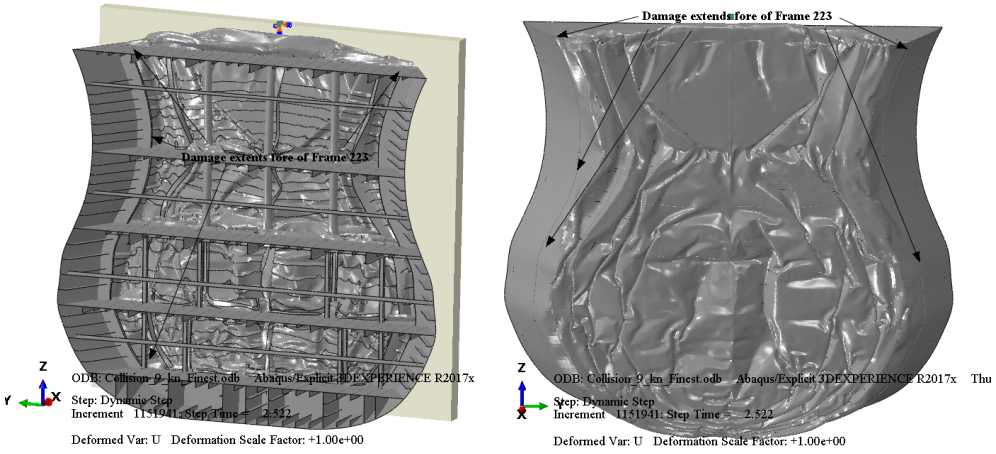

Figure 3.22: Final position at t=2.52 sec (9 kn simulation)

It is observed that the final deformation patterns extend just fore of the strengthened Web Frame 223 (instead of Frame 227, on the 6 kn simulation), since it provides a rigid enough support to cause buckling/folding of the adjacent (fore) structure.

On the context of damage description, several contour plots of the equivalent plastic strain are depicted in Figures 3.23-3.26. The fringes' upper limit is the 0.22 cut-off value of the Grade A true stress - true strain curve:

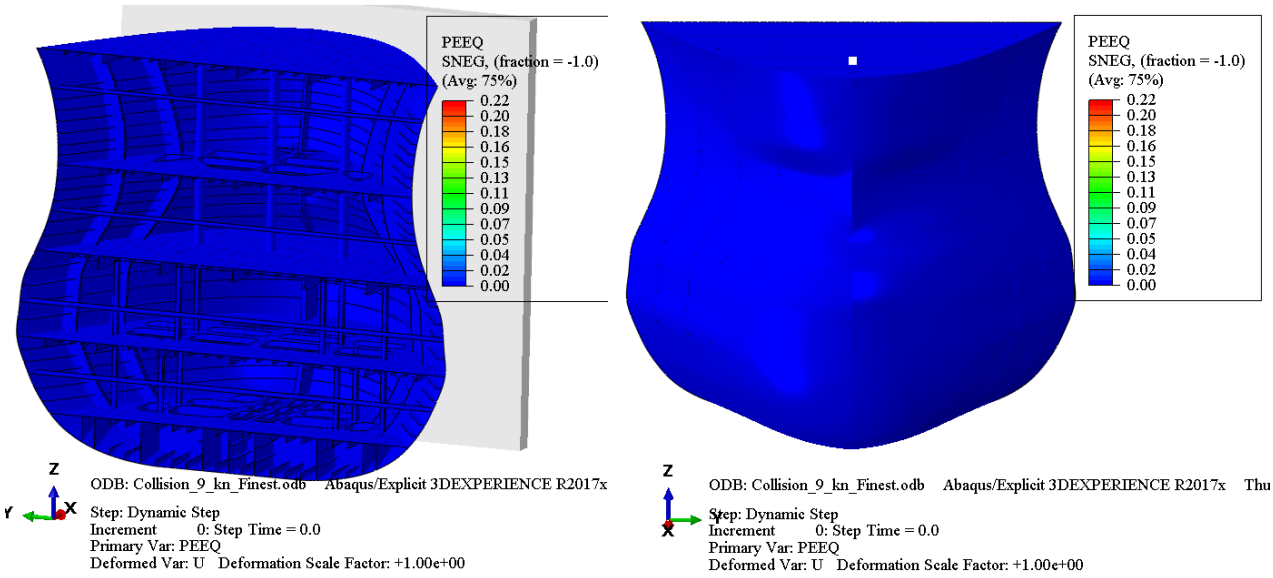

Figure 3.23: Initial undeformed position at t=0 (9 kn simulation)

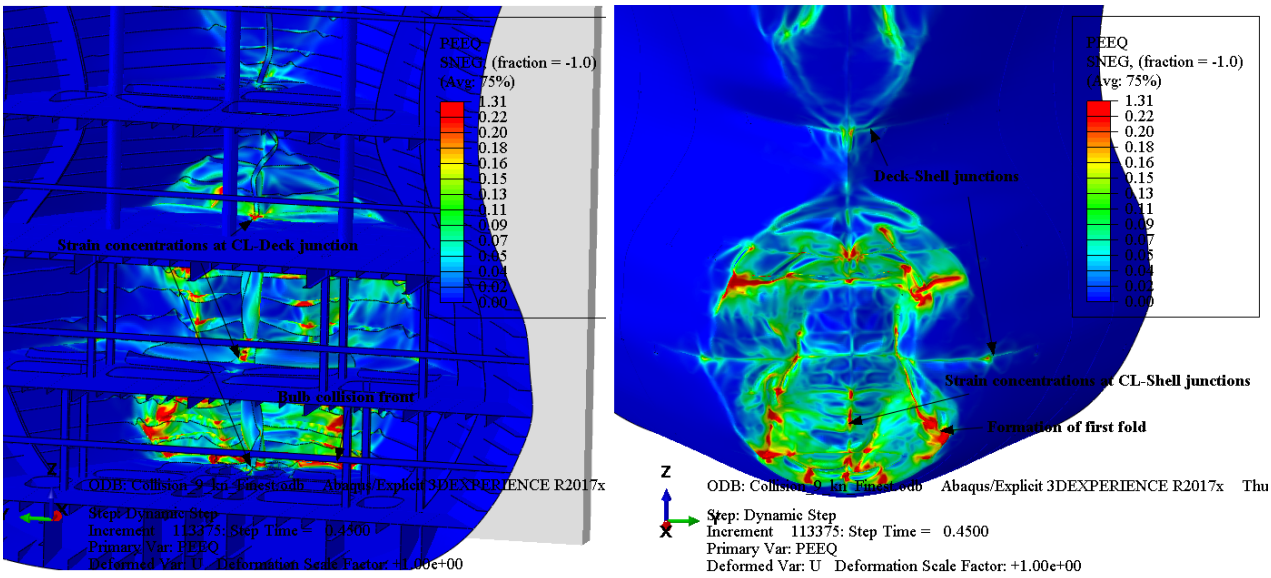

Figure 3.24: Distribution of equivalent plastic strains at t=0.45 sec (9 kn simulation)

Figure 3.24 depicts the damage distribution after stem contact has been established. A zoomed screenshot of the bulb aft view is depicted on the left, while a zoomed screenshot of the bulb-stem fore view is depicted on the right, denoting the areas of plastic strain concentrations, which are mainly observed in junctions of the outer shell with internal members, such as decks and CL section T-bar stiffeners.

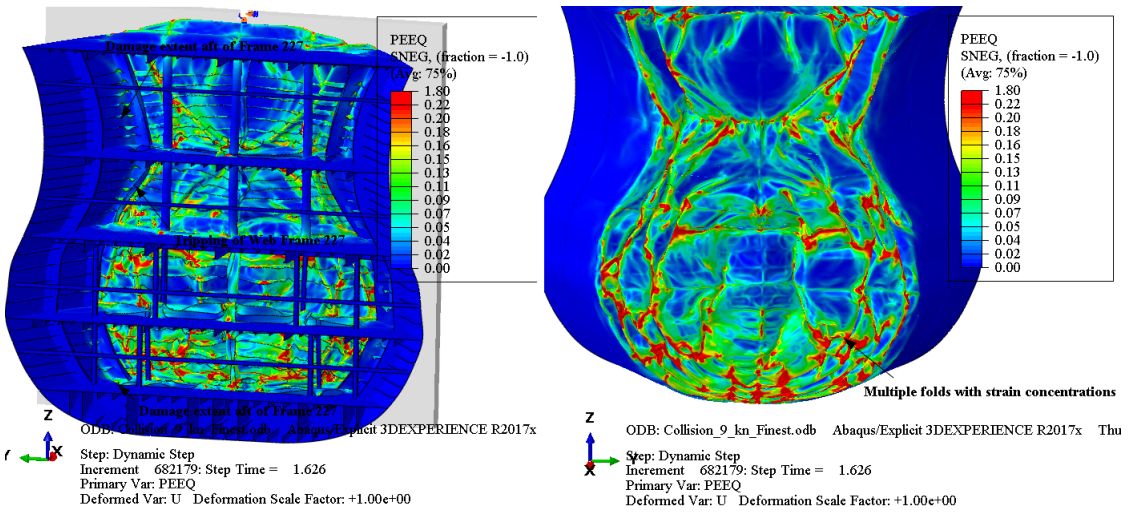

Figure 3.25: Distribution of equivalent plastic strains at t=1.626 sec (9 kn simulation)

Figure 3.25 depicts the damage distribution during axial crushing under $F_{m,2}$ (t=1.626 sec). The formation of folding patterns, as well as the damage extent aft of the strengthened Web Frame 227 is noted.

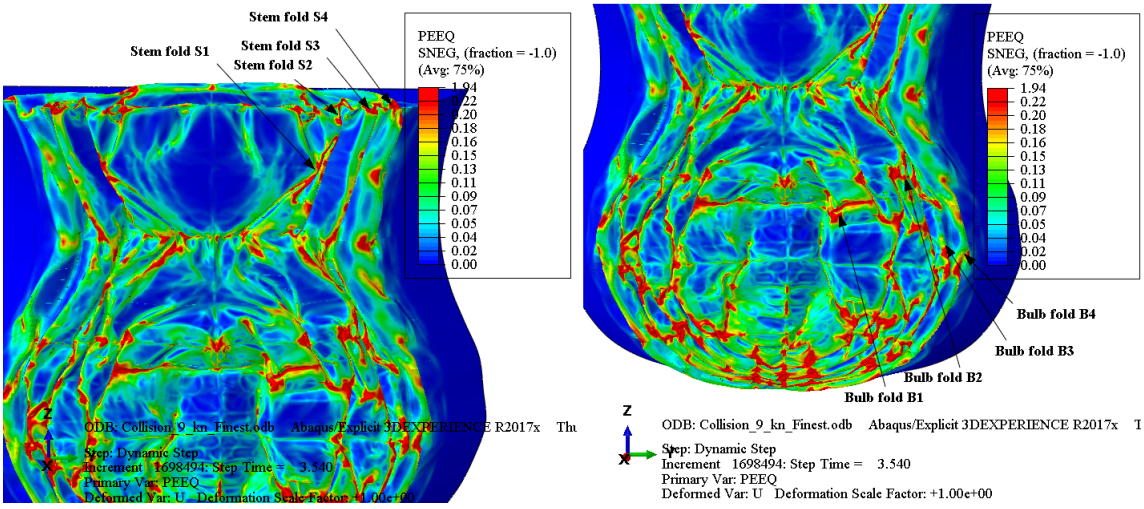

Figure 3.26: Distribution of equivalent plastic strains at t=2.52 sec (9 kn simulation)

Finally, Figure 3.26 depicts the final damage distribution at the end of the collision (t=2.52 sec). A zoomed view of the stem is depicted on the left, while a zoomed view of the bulb is depicted on the right, noting the final folding patterns observed. It is noted that four clear folds are observed on the stem (S1, S2, S3 and S4) and four more on the bulb (B1, B2, B3 and B4), of which the S2-B2, S3-B3 and S4-B4, respectively, are interconnected. The formation of one additional fold is noted, between frames 223-227, compared to the 6 kn simulation.

3.4 Results of the low-speed simulation

3.4.1 Discussion on the force-displacement curve ($V = 3\ kn$)

The force-displacement curve for the 3 kn simulation is presented in Figure 3.27:

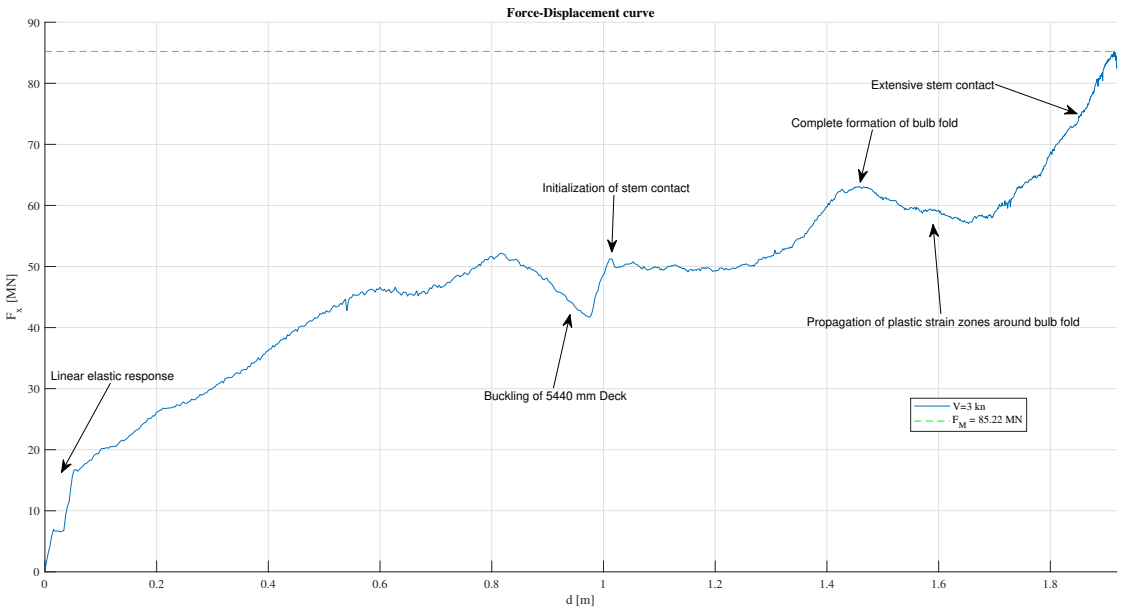

Figure 3.27: Force-displacement curve (3 kn simulation)

The following stages are noted:

1. The initial part of the F-d curve denotes the linear elastic response of the structure.

2. Buckling of the 5440 mm Deck signifies a loss on the load-bearing capacity of the bulb.

3. After that, initiation of stem contact at about $d = 1\ m$ occurs.

4. A gradual increase on the reaction force denotes the formation of the bulb fold.

5. Following that, propagation of plastic strain areas around the bulb fold occurs, signifying a small decrease on the reaction force.

6. Finally, a sharp increase on the reaction force is observed, due to the establishment of complete stem contact. The simulation stops at a maximum penetration $d_{max} = 1.92$ m, at which it also exhibits its maximum reaction force $F_M \approx 85MN$.

It is hereby noted that no clear mean force F_m can be discerned on the low-speed collision simulation. This is most likely attributed to the relatively small collision velocity, which results in simulation termination before the bulb and the stem are simultaneously in complete contact with the collision plate, crushing their adjacent aft structure.

3.4.2 Distribution of energies ($V = 3\ kn$)

The distribution of energies during the 3 kn simulation is presented in Figure 3.28, as a percentage of the initial model energy of $E_k = 89.58\ MJ$:

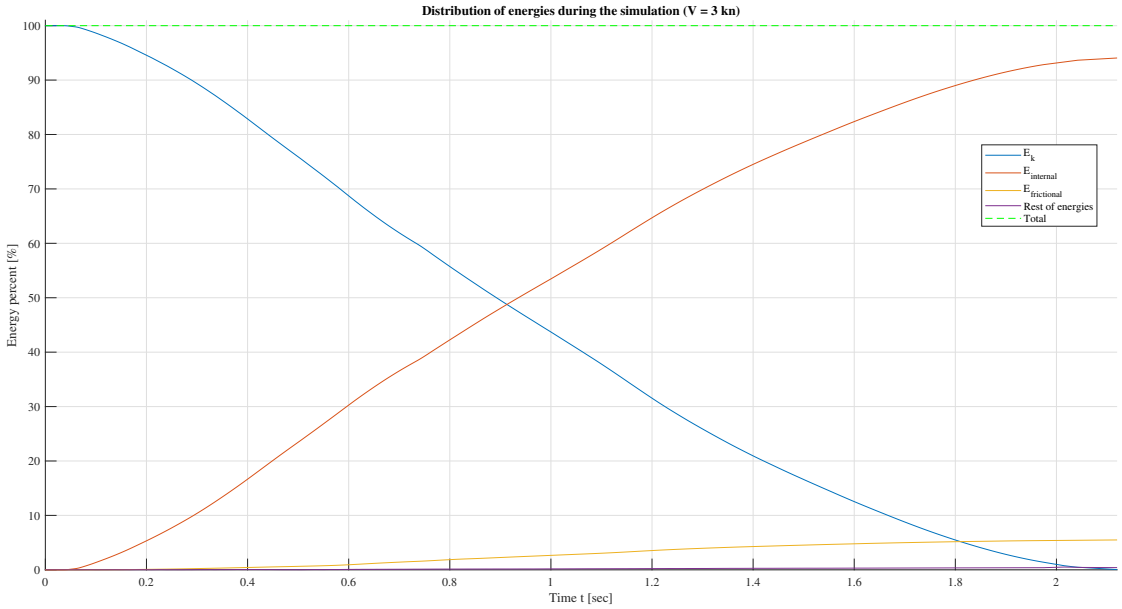

Figure 3.28: Distribution of model energies (3 kn simulation)

The following remarks can be made:

1. The available kinetic energy E_k to cause structural damage is dissipated mainly (94.5%) by internal energy $E_{internal}$ (the artificial strain energy has been checked to be at most 3% of the initially available model energy).

2. The energy dissipated by friction is $\approx 5.5\%$ of the model energy. A decrease on this percentage is observed, as a function of collision speed.

3. The rest of the model energies are negligible.

3.4.3 Damage description ($V = 3\ kn$)

The deformation pattern observed on the ship bow is presented in Figures 3.29-3.33. Once again, an aft view is presented on the left, and a fore view on the right:

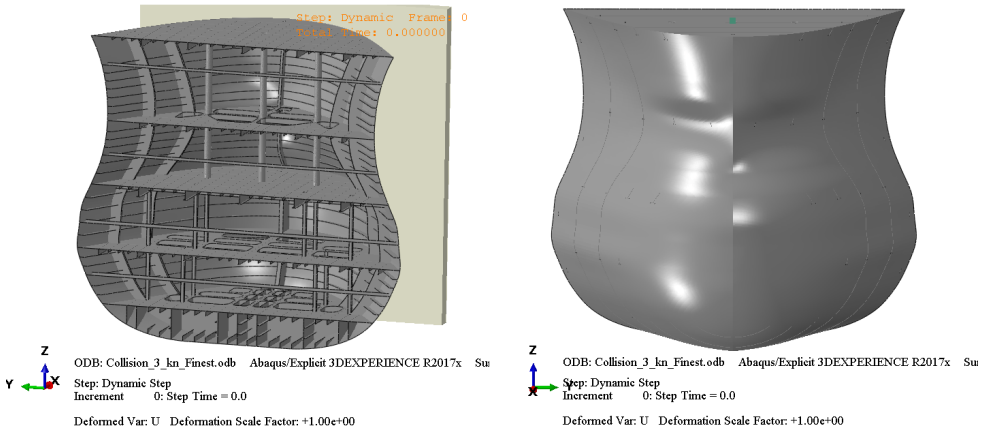

Figure 3.29: Initial position at t=0 (3 kn simulation)

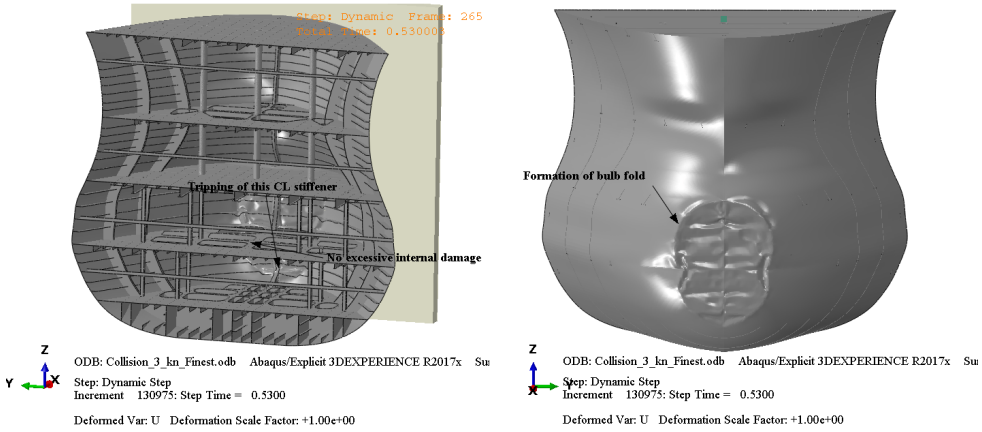

Figure 3.30: Deformation pattern at t=0.53 sec (3 kn simulation)

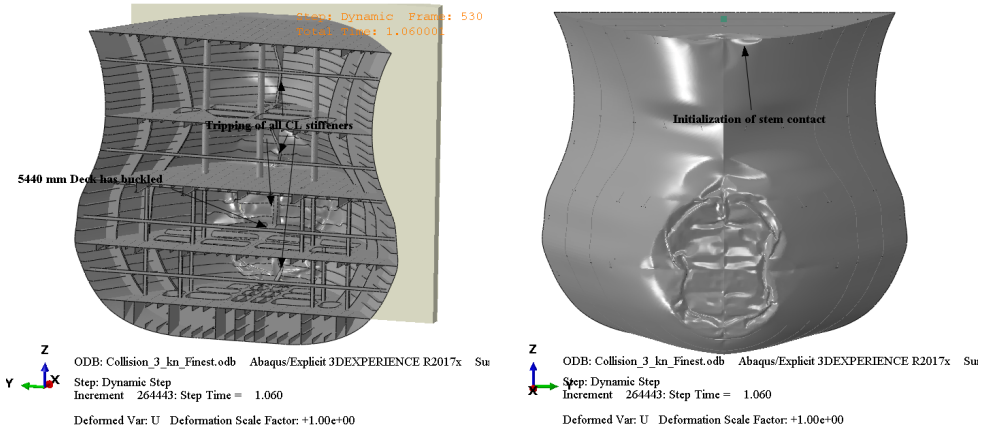

Figure 3.31: Deformation pattern at t=1.06 sec (3 kn simulation)

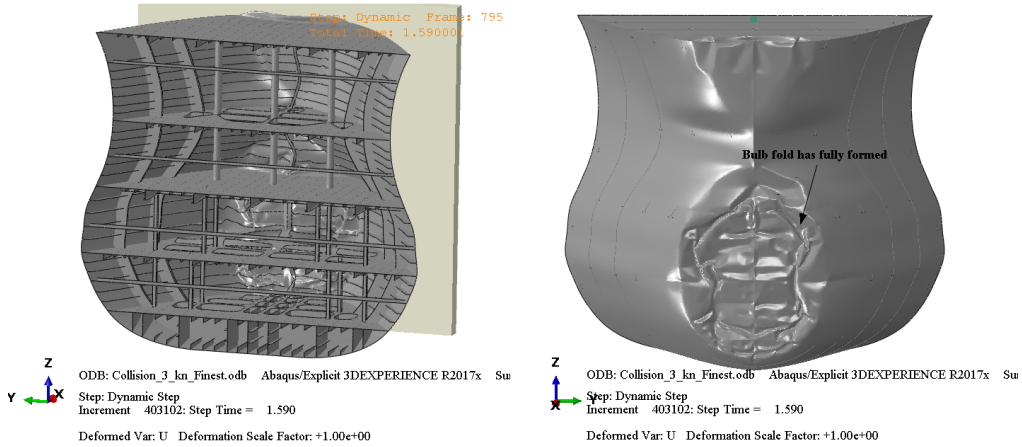

Figure 3.32: Deformation pattern at t=1.59 sec (3 kn simulation)

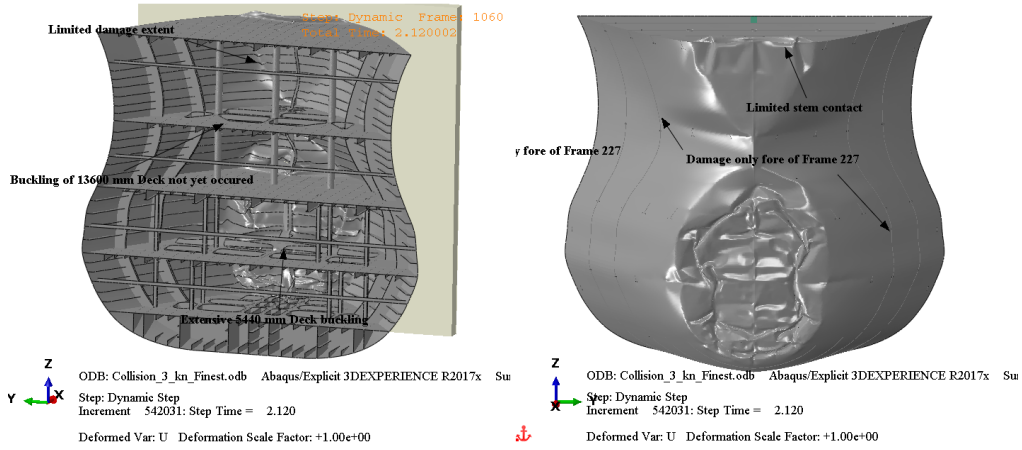

Figure 3.33: Final position at t=2.12 sec (3 kn simulation)

It is observed that the final deformation patterns have a limited extent, and only fore of the strengthened Web Frame 227, since it provides a rigid enough support to cause buckling/folding of the adjacent (fore) structure.

On the context of damage description, several contour plots of the equivalent plastic strain are depicted in Figures 3.34-3.37. The fringes' upper limit is the 0.22 cut-off value of the Grade A true stress - true strain curve:

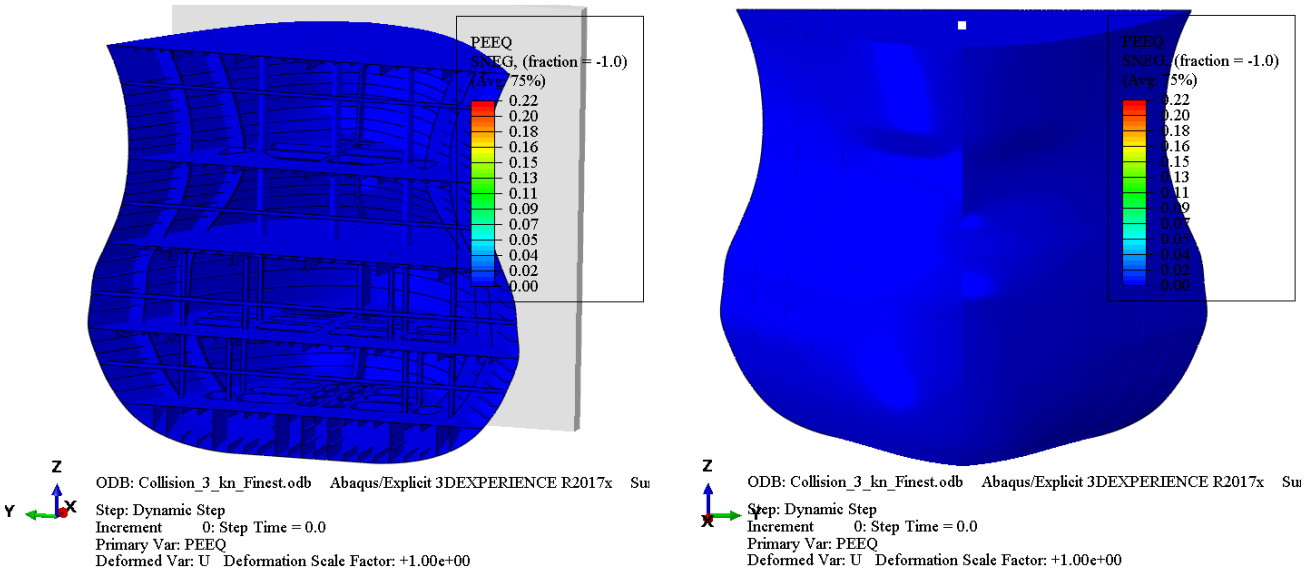

Figure 3.34: Initial undeformed position at t=0 (3 kn simulation)

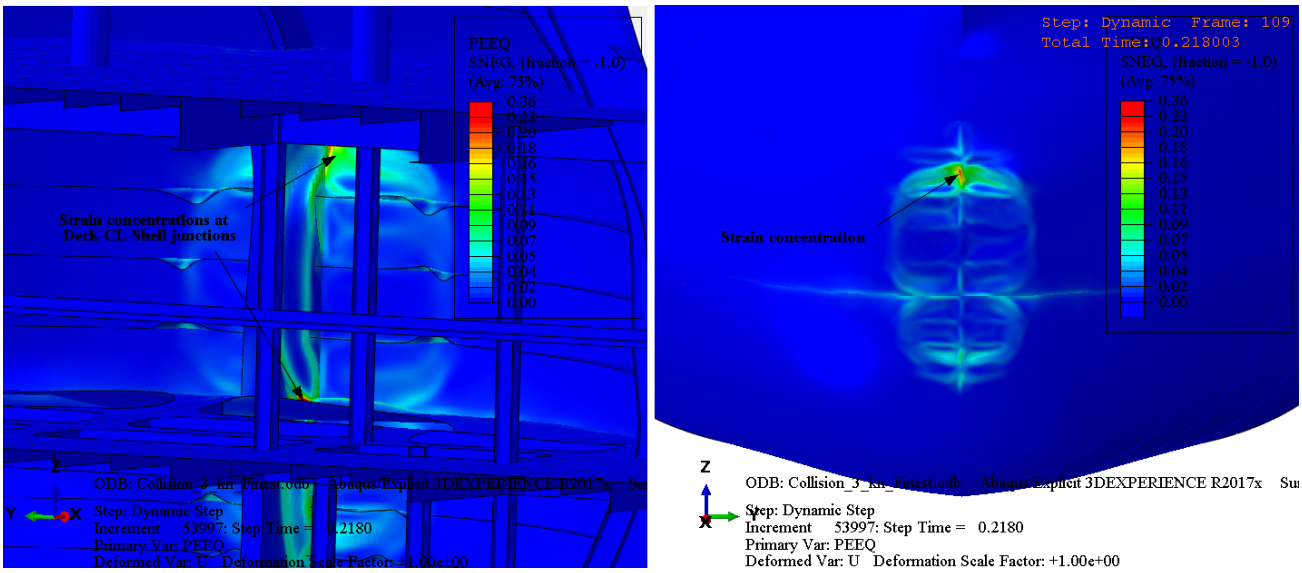

Figure 3.35: Distribution of equivalent plastic strains at t=0.218 sec (3 kn simulation)

Figure 3.35 depicts the damage distribution after the bulb contact has been established. A zoomed screenshot of the bulb aft view is depicted on the left, while a zoomed screenshot of the bulb fore view is depicted on the right, denoting the areas of plastic strain concentrations, which are observed in junctions of the outer shell with internal members, such as decks and CL section stiffeners.

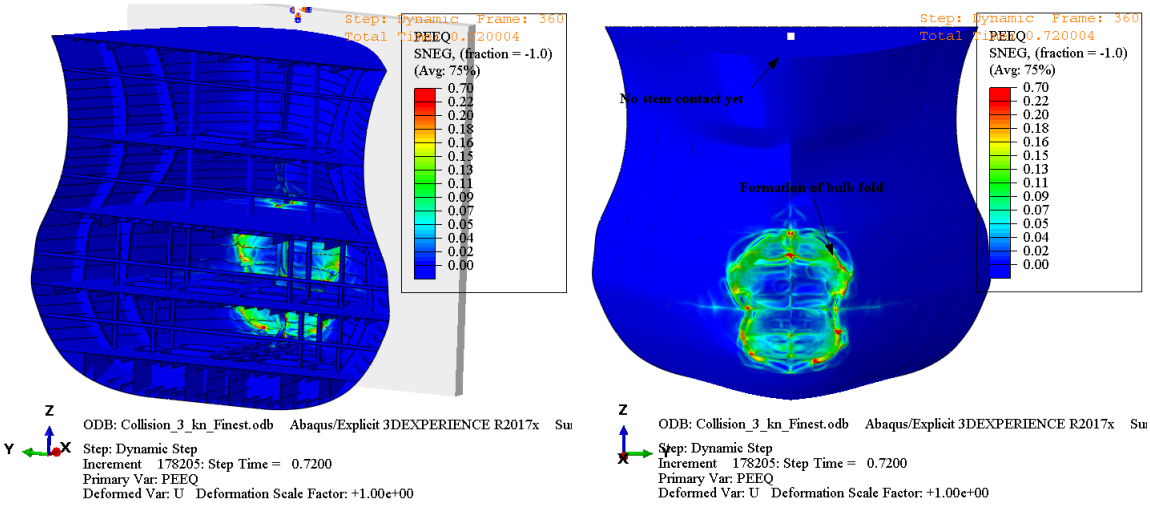

Figure 3.36: Distribution of equivalent plastic strains at t=0.72 sec (3 kn simulation)

Figure 3.36 depicts the damage distribution exactly before the initial stem contact. The formation of a bulb folding pattern is observed.

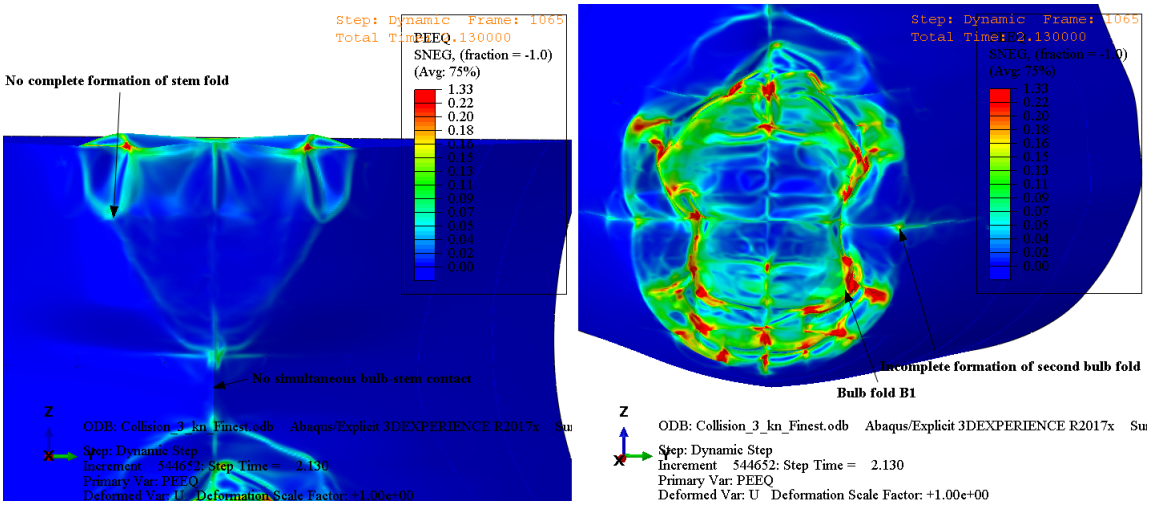

Figure 3.37: Distribution of equivalent plastic strains at t=2.12 sec (3 kn simulation)

Finally, Figure 3.37 depicts the final damage distribution at the end of the collision simulation (t=2.12 sec). A zoomed view of the stem is depicted on the left, while a zoomed view of the bulb is depicted on the right, noting the final folding patterns observed. No complete folding pattern is observed on the stem, while a single fully-developed fold (B1) is observed on the bulb. No simultaneous stem-bulb crushing has been established, hence, no interconnected folds have developed. This is expected of a low-energy collision, with mainly local damage distribution on the bulb.

3.5 Distribution of forces on the bulb/stem

During the simulated collisions, the forces exerted separately on the bulb and the stem were extracted, in order to identify their relative contribution to the total bow strength.

3.5.1 Force distribution from $V = 6\ kn$ simulation

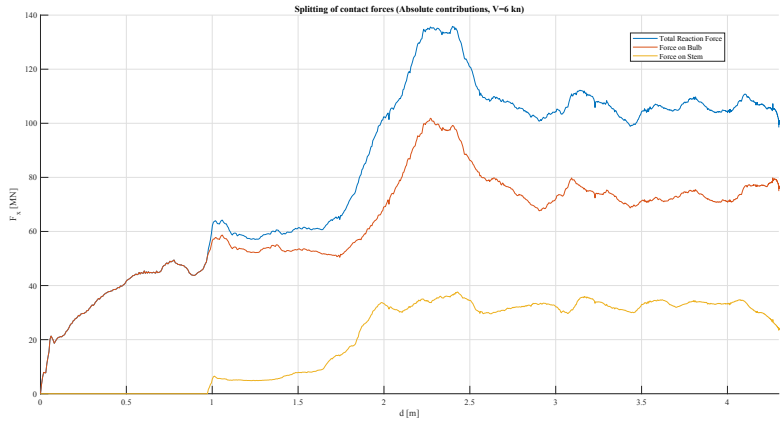

(a) Absolute contributions of bulb/stem on the F-d curve

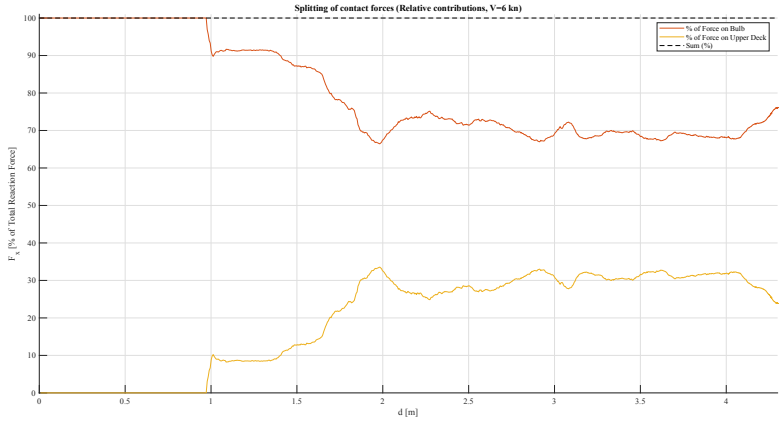

(b) Relative contributions of bulb/stem on the F-d curve

Figure 3.38: Force distribution (V = 6 kn simulation)

The absolute (in MN) and relative (in %) contribution of the bulb and the stem to the total reaction force, as a function of penetration depth, is depicted in Figures 3.38a and 3.38b, respectively, for the 6 kn collision simulation.

After the initial stem contact (around $d = 1\ m$), its relative contribution is increased, owing to the establishment of its full contact with the collision plate, and the force distribution balances around 70% for the bulb and 30% for the stem. The bulb is, notably, the primary structural member resisting the bow deformation.

3.5.2 Force distribution from $V = 9\ kn$ simulation

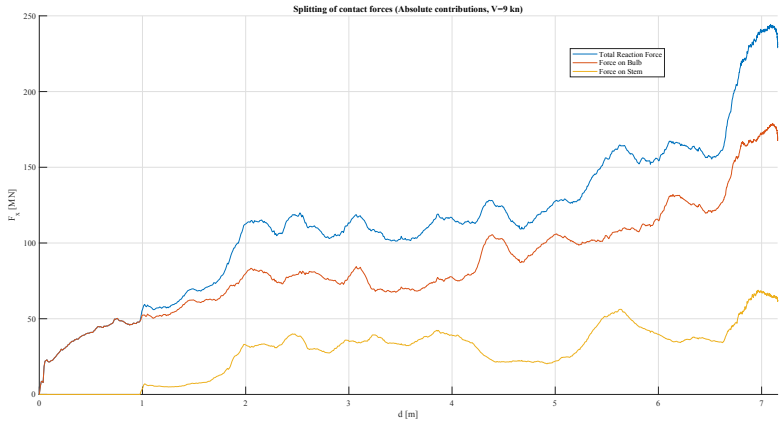

(a) Absolute contributions of bulb/stem on the F-d curve

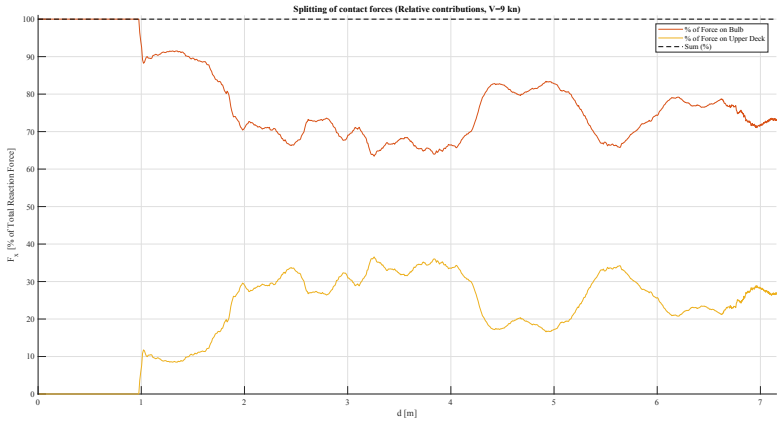

(b) Relative contributions of bulb/stem on the F-d curve

Figure 3.39: Force distribution (V = 9 kn simulation)

The absolute (in MN) and relative (in %) contribution of the bulb and the stem to the total reaction force, as a function of penetration depth, is depicted in Figures 3.39a and 3.39b, respectively, for the 9 kn collision simulation.

After the initial stem contact (around $d = 1\ m$), a force redistribution takes place between the bulb and the stem, up to $d = 2\ m$, during which the stem engagement on the crushing process becomes increasingly important (about 30%, as in the 6 kn simulation). After the damage extends towards and aft of the strengthened Web Frame 227 (which occurs after $d = 4.5\ m$), the force distribution balances (with several fluctuations, owing to the failure of intermediate decks, located on the bulb or the stem) at about 75% for the bulb - 25% for the stem. This 5% difference (compared to the 6 kn simulation) is attributed to the engagement of additional stiffeners on the bulb, aft of Frame 227.

3.5.3 Force distribution from $V = 3\ kn$ simulation

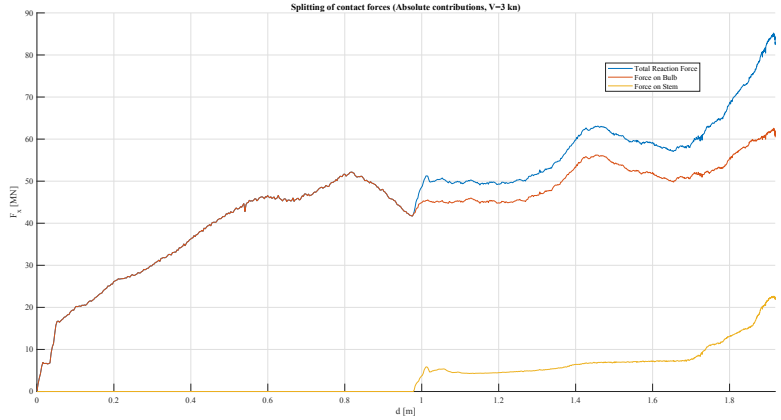

(a) Absolute contributions of bulb/stem on the F-d curve

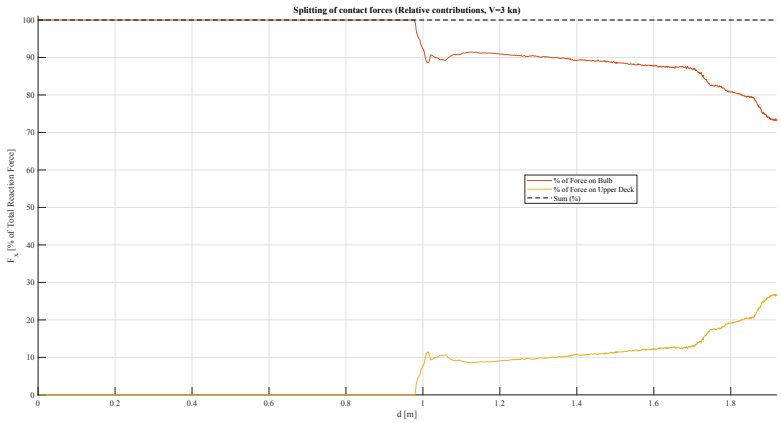

(b) Relative contributions of bulb/stem on the F-d curve

Figure 3.40: Force distribution (V = 3 kn simulation)

The absolute (in MN) and relative (in %) contribution of the bulb and the stem to the total reaction force, as a function of penetration depth, is depicted in Figures 3.40a and 3.40b, respectively, for the 3 kn collision simulation.

After the initial stem contact (around $d = 1\ m$), the bulb contributes about 90% to the total force, being the dominant structural member resisting the deformations. A decrease on this contribution is consequently observed, following the establishment of stem contact, but this is abruptly interrupted by the simulation termination.

3.5.4 Discussion on bulb/stem contribution (forces/energies)

The relative engagement of the bulb/stem structures in the crushing process is a direct function of the penetration depth, since different stiffening members contribute to the crushing strength, when examining different frames of the bow. The bulb, being stiffer than the stem, exerts/receives relatively larger forces (Servis et al. (2002)).

Relative contributions of the bulb in the total bow strength in the order of 70% are consistent with the observations of Pedersen et al. (1993), who calculated a 60% bulb contribution, for a 3000 DWT general cargo carrier. It is, however, noted, that such general cargo vessels exhibit relatively unstrengthened bulb designs, when compared to modern Bulk Carrier designs, hence the (slightly) reduced percentage in the relative bulb contribution.

Through direction integration of the force-displacement curves depicted in 3.38b, 3.39b and 3.40b, the relative contribution of the bulb and the stem on the energy absorption procedure in head-on collisions can be calculated.

The respective results are:

1. Relative contribution to total energy absorption of the bulb by 94% for the low-speed (3 kn) collision simulation.

2. Relative contribution to total energy absorption of the bulb by 80% for the intermediate-speed (6 kn) collision simulation.

3. Relative contribution to total energy absorption of the bulb by 78% for the high-speed (9 kn) collision simulation.

Hence, the bulb contribution to the total resistance of the bow structure is significant, since it must successfully absorb the majority of the forces exerted on the hull, as well as the kinetic energy through plastic deformations.

3.6 Comparison of different collision scenarios

3.6.1 Comparison of the force-displacement curves

The force-displacement curves for the different collision speeds examined ($V = 3\ kn, V = 6\ kn$ and $V = 9\ kn$) are plotted in Figure 3.41:

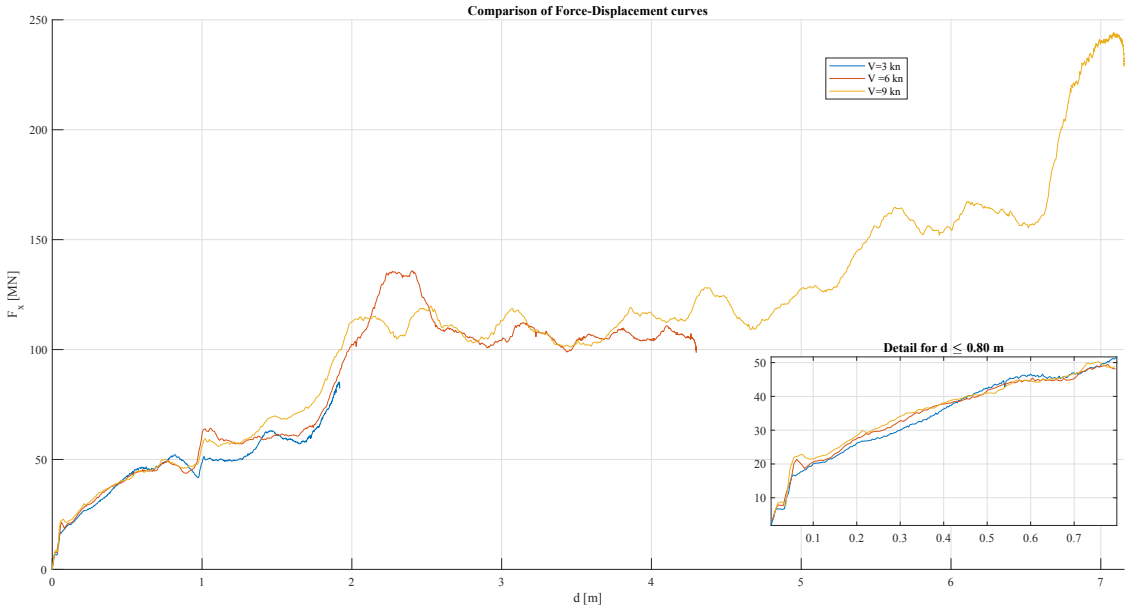

Figure 3.41: Comparison of Force-Displacement curves for various collision speeds

These curves clearly exhibit a similar pattern, regardless of the differences in initial speed/available kinetic energy. Especially for $d \leq 0.80\ m$, they are nearly coincidental.

Thus, the initial deformation pattern (before collapse of the first intermediate deck on the bulb) is independent of the collision velocity, and this part of the Force-Displacement curve can be considered static. Following this deformation, dynamic phenomena become relatively more important, with an increasing trend on the reaction forces, which, however, is not overly significant (in the order of $10 - 20\%$).

Hence, the assumption of quasi-static bow deformation for FEA analyses can be considered accurate enough for a rough computation of the force displacement curve, whilst also being a conservative assumption.

3.6.2 Summary of FEA results

The results of each FEA simulation are presented in Table 3.1:

Comparison of critical parameters for the different bow collision scenarios considered			
	V= 3 kn	V = 6 kn	V = 9 kn
Initial available kinetic energy [MJ]:	89.58	358.31	806.23
Maximum reaction force F_M [MN]:	85.22	135.85	244.24
Mean force F_m [MN]:	No clear mean force	105.62	111.86 and then 160.14
Maximum penetration depth d_{max} [m]:	1.92	4.30	7.16
Collision duration [sec]:	2.12	2.56	2.52
Bulb relative contribution to bow strength (forces):	90%	70%	70% and then 75%
Bulb relative contribution to energy absorption:	94%	80%	78%

Table 3.1: Summary of important results of FEA simulations

On the subject of maximum forces F_M, values in the order of 100 MN are typical of longitudinally stiffened bows, such as the present case. For transversely stiffened bows, maximum forces F_M are one order of magnitude lower (Lützen et al. (2000)).

3.7 Deformation patterns of actual bow collision incidents

Figure 3.42 depicts deformation patterns observed after actual bow collision incidents:

(a) M/V Basht (2021)

(b) F/V Kirrixki (2019)

(c) M/V Le-Sheng (2014)

(d) M/T Zephyr I (2022)

Figure 3.42: Deformation patterns of actual bow collision incidents

On Figure 3.42a, the bulb crushing of containership M/V Basht is observed, after contacting a pier. Four apparent folds can be discerned, whilst the bulb has been completely flattened. It should, however, be noted, that bulb designs for containerships usually exhibit a more sharp form than the blunt form examined in the present study.

On Figure 3.42b, the stem crushing pattern of fishing vessel Kirrixki is observed, following its collision with a large Bulk Carrier. Complete flattening of the stem is apparent, although the vessel is not equipped with a bulbous bow.

On Figure 3.42c, the stem crushing pattern of Handysize Bulk Carrier Le Sheng is observed, following its collision with a Capesize Bulk Carrier. The stem is flattened, whilst exhibiting clear folding patterns, much like Figure 3.26 of present study.

Finally, on Figure 3.42d, the stem crushing pattern of Aframax tanker Zephyr I is observed, following its collision with a Post-Panamax containership, where, yet again, complete flattening of the stem can be discerned.

Based on the aforementioned deformation patterns from actual bow collision incidents, the deformation patterns discussed in subsections 3.2.3, 3.3.3 and 3.4.3 appear to be in the right direction.

Chapter 4

Comparison of FEA results with simplified analytical methodologies

4.1 Introduction to simplified analytical methodologies

Since Finite Element methodologies usually require comprehensive modelling efforts, an alternative to assess the capacity of complex structures is by use of simplified analytical formulas. These are developed for simple elements, after theoretical analysis of their possible failure mechanisms, followed by experimental verification, and are especially suitable for risk assessment calculations, since their application is relatively straightforward.

On the subject of crushing, such methodologies developed are usually based on the assumption that a complex ship-shaped thin-walled structure can be subdivided into simple structural L-, T- and X-shaped elements (see, for example, Figure 4.1).

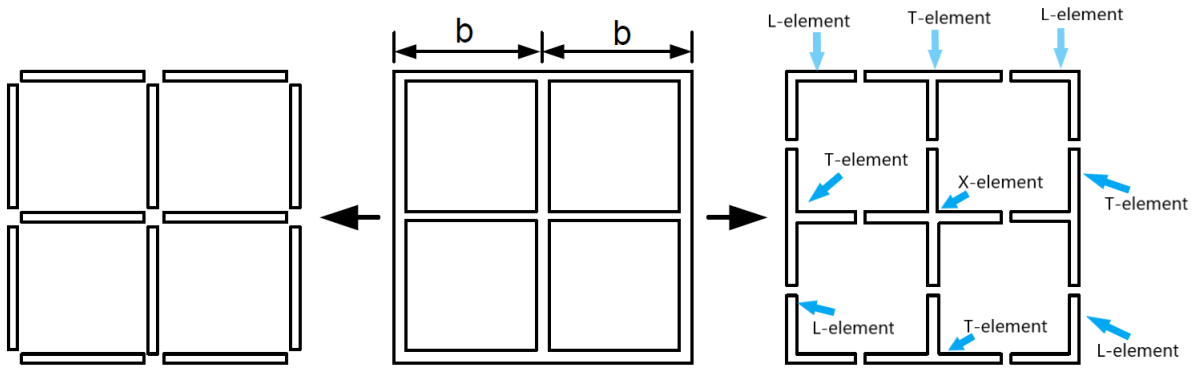

Figure 4.1: Division of plated ship structure into L-, T- and X-shaped elements

The relative contribution of these basic structural elements is then summed, producing the total resistance to crushing of the complex structure, as it is progressively crushed from the front (the contribution being either on the force, or the energy dissipated).

Perhaps the greatest advantage of such methodologies is the much more experimentally and computationally inexpensive capability to study simple L-, T- or X-shaped elements. However, the formulas produced should be used with caution, since they are calibrated against specific (dominant) failure mechanisms observed experimentally, and often exhibit an inability to accurately capture the structural interaction of basic elements, which rarely -if ever- truly behave independently of one another.

4.2 Division of bow section into L-, T-, and X-elements

In order to ensure that the results of Chapter 3 are in the right direction, several section cuts will be made at specific longitudinal positions of the bow structure. These bow sections will, then, be subdivided into L-, T- and X-elements (such as described in Figure 4.1), utilizing the smearing-out technique, which is described below.

4.2.1 The smearing-out technique

A longitudinal stiffener of a plate may be considered a T-element, if and only if the stiffener provides a relatively rigid support, which is usually not the case. This type of discretization leads to overestimation of the crushing strength of the bow section, since T-elements contribute significantly to the capacity to withstand crushing forces.

In order to avoid such overestimations, the concept of equivalent thickness for more accurate application of each simplified analytical method has been introduced by Paik et al. (1996), a technique also termed ”smearing-out” technique.

In this technique, the regular longitudinal stiffeners are smeared out in the adjacent plates, by enhancing the plates' respective thickness by a factor depending on the stiffeners' sectional area (see Equation 4.1):

$$t_{eq} = t + k \cdot \frac{A_s}{b} \tag{4.1}$$

where t is the regular plate-element thickness, k is an empirical constant, which usually

adopts the value 1.0, A_s is the sectional area of the longitudinal stiffeners and b is the plate breadth. This process is illustrated in Figure 4.2:

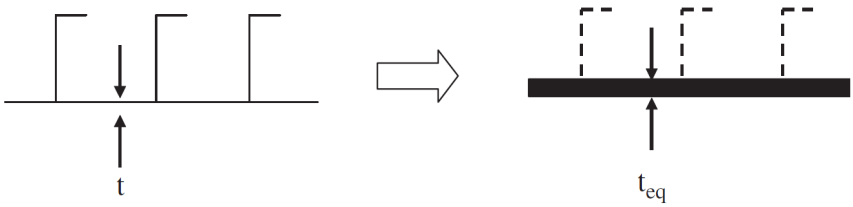

Figure 4.2: The smearing-out technique (reproduced from Yamada and Pedersen (2008))

For each bow section discretized to L-, T- and X-elements, the smearing-out technique will be utilized.

4.2.2 Bow structure discretization

For the bow geometric model presented in section 2.2, the following sectional cuts are studied:

1. A sectional cut on the bulb, in order to assess the crushing of the bulb before stem contact is established (Stage I).

2. A sectional cut on the stem, in order to assess the combined crushing behavior of the stem and the bulb, following the initial stem contact (Stage II).

3. A sectional cut fore of the strengthened Web Frame 227, in order to assess the combined crushing behavior of the stem and the bulb, following the establishment of full stem contact (Stage III).

4. A sectional cut fore of the strengthened Web Frame 223, in order to assess the crushing behavior of the bow structure, following the extent of damage aft of Frame 227, and the engagement of relatively more elements (Stage IV).

The analytical discretization of the aforementioned sectional cuts into L-, T- and X-elements is presented in Appendix B.

4.3 Analytical formulae utilizing L-, T- and X-elements

4.3.1 Method of Amdahl (1983)

Amdahl (1983) pioneered the first formula for computation of the mean crushing force F_m, as a function of the sectional cut longitudinal position. The contributions to the internal energy dissipation of L-, T- and X- elements are considered and then summed. Additionally, he suggested the use of a mean thickness, in order to account for the variation of the flow stress along the section. The suggested formula for a uniform thickness t is:

$$F_m = 2.42 \cdot \sigma_0 A \left(\frac{n_{AT} t^2}{A} \right)^{0.67} \cdot \left(0.87 + 1.27 \cdot \frac{n_X + 0.31 n_T}{n_{AT}} \cdot \left(\frac{A}{(n_X + 0.31 n_T) t^2} \right)^{0.25} \right)^{0.67} \tag{4.2}$$

where:

- σ_0: The flow stress, calculated as $\frac{\sigma_y + \sigma_{UTS}}{2}$, in order to include work-hardening effects
- $A = \sum A_i$: The total cross-sectional area
- t: The (equivalent) average plate thickness of the bow section
- $n_{AT} = n_L + n_T$ is the number of L-elements and T-elements
- n_L is the number of L-elements
- n_T is the number of T-elements
- n_X is the number of X-elements

4.3.2 Method of Yang and Caldwell (1988)

In a similar manner, the method of Yang and Caldwell (1988) considers the internal energy dissipation caused by plastic collapse of the individual L-, T- or X-elements, and then sums the contributions along the cross-section. The formula suggested is:

$$F_m = \sigma_0 \cdot (1.178 t^2 \frac{L}{H} + 0.215 n_{AT} t H + 6.935 n_{AT} t^2 + 0.265 n_T t H + 0.589 n_T t^2 + 0.75 n_X t H + 0.375 n_X t^2) \tag{4.3}$$

where the definitions of equation 4.2 hold, and, additionally:

- $L = \sum b_i$ (b_i being the width of an individual plate i)
- $H = \sqrt{\frac{1.178tL}{0.215n_L+0.48n_T+0.75n_X}}$ is the effective folding length

The increase expected by strain-rate effects is included in the aforementioned coefficients. The presence of longitudinal stiffeners in the cross-section is recommended to be modelled through the use of an equivalent thickness (smearing-out technique), owing to the additional plastic collapse moment provided by the stiffeners to the plate panels.

Through the use of Equation 4.3, Yang and Caldwell (1988) predict that the increase of crushing forces when considering the dynamic strain-rate effect is expected to be in the range of 10%, for velocities ranging from $0 - 15$ knots.

4.3.3 Method of Abramowicz (1994)

In a similar fashion with the aforementioned equations, Abramowicz (1994) suggested the following formula:

$$F_m = (n_L + 1.2n_T + 2.1n_X) \cdot (3.263\sigma_0 c^{0.33} t^{1.67}) \tag{4.4}$$

where the definitions of equations 4.2 and 4.3 apply, and, additionally:

- $n = n_L + n_T + n_X$: The total number of super-elements on the bow cross-section
- $c = \frac{L}{n}$

4.3.4 Discussion and comparison with FEA results

In the case of bow crushing, since the deformation mode can be well predicted (folding and crushing of individual elements), application of simplified analytical methods based on the upper bound theorem is expected to display good agreement with finite element analysis results (Liu et al. (2018a)).

It is also noted that the definition of flow stress σ_0 as the mean between yield stress σ_y and ultimate tensile stress σ_{UTS} is a frequent assumption when applying simplified analytical formulas, in order to account for strain-hardening effects in a simple manner.

In the present analysis, the mean thickness t of the bow section is calculated based on a weighted averaging procedure on the individual (smeared-out) plated elements, the weight being each element's cross-sectional area. The same calculation procedure is applied when evaluating the mean element width b, and the mean flow stress σ_0 of the bow-section (the analytical computations are presented in Appendix B).

A comparison of the application of Equations 4.2, 4.3 and 4.4 for the crushing stages I-IV (described in section 4.2.2), against the high-speed collision FEA simulation, is presented in Figure 4.3:

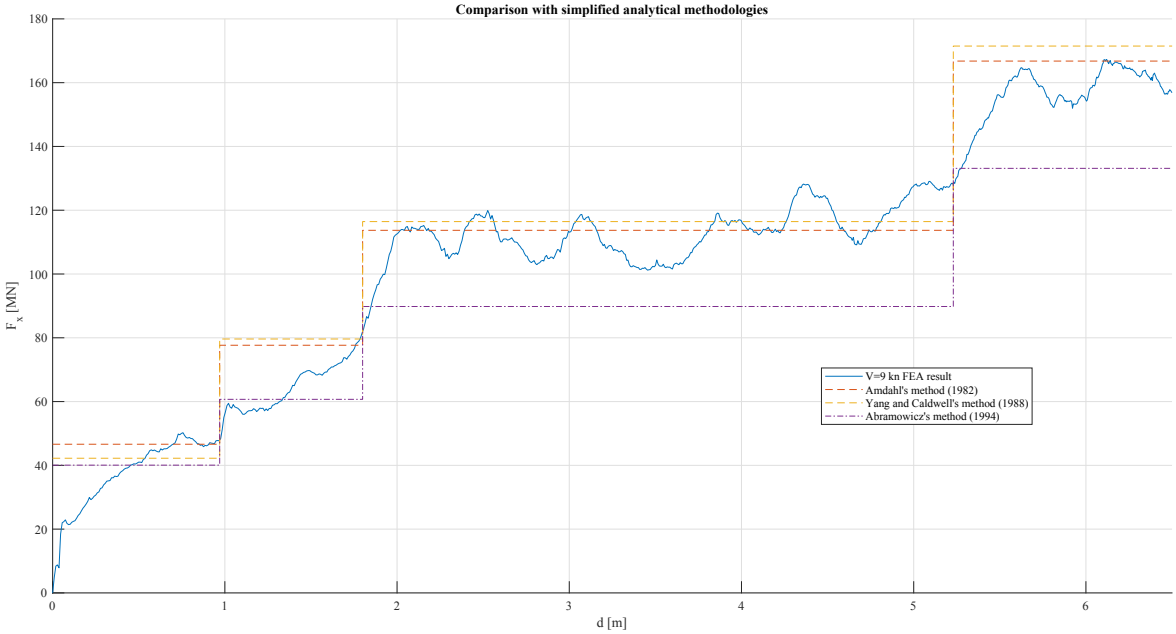

Figure 4.3: Comparison of Force-Displacement curve with simplified analytical formulas

The methods of Amdahl and Yang and Caldwell exhibit a reasonable degree of accuracy, although they tend to overestimate the expected mean crushing forces by up to 15%. Pedersen et al. (1993) also commented that Amdahl's method exhibits this overestimating trend, when evaluating longitudinally stiffened bows. In the case of Yang and Caldwell's method, this trend may be attributed to the inclusion of strain-rate effects in the simplified analytical formula suggested.

In the case of Abramowicz's method, the formula suggested tends to underestimate the mean crushing forces by up to 20%. This trend has also been observed in a benchmark study performed by Yamada and Pedersen (2008), comparing various simplified analytical formulas with experimental results of bow model crushing setups.

More accurate predictions of the mean crushing forces can be obtained by averaging the simplified analytical formulas used, in order to evenly distribute their errors. This comparison is depicted in Figure 4.4. The divergence percentages from the simulated mean crushing forces range from $1.5 - 6.5\%$.

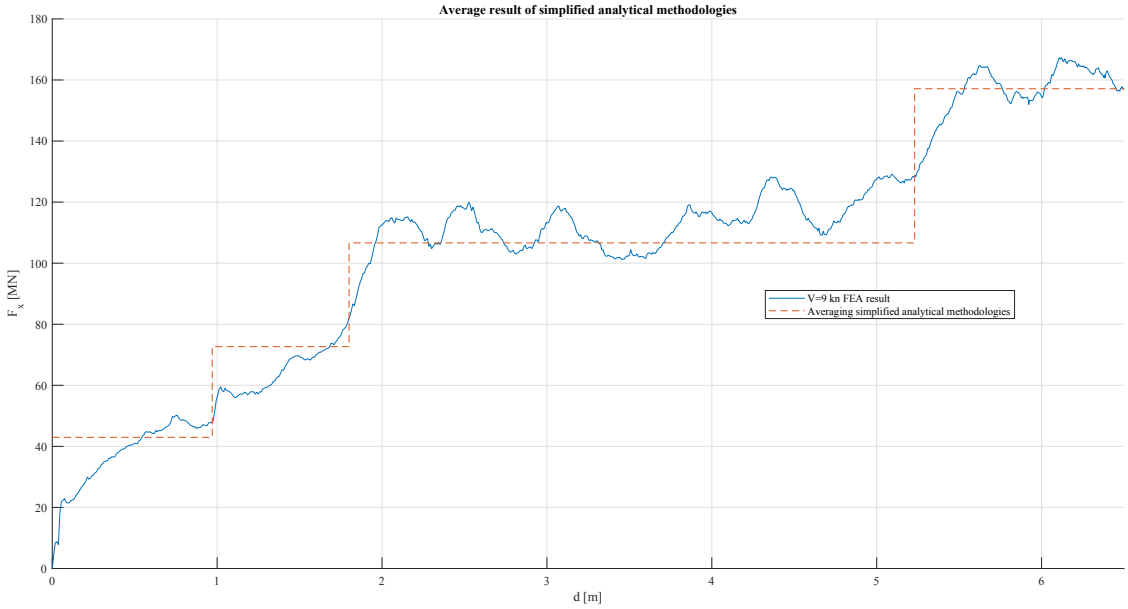

Figure 4.4: Comparison of Force-Displacement curve with averaged analytical formulas

Although the degree of accuracy attained is not ideal, it can be concluded that the results produced with FEA can be considered in the right direction, displaying acceptable agreement (<7%) with employment of simplified analytical procedures, utilizing L-, T- and X-elements.

4.4 Simple formulae for the maximum crushing force F_M

4.4.1 Method of Pedersen et al. (1993)

Pedersen et al. (1993) suggested a relatively simple empirical formula to estimate the maximum crushing load F_M, after careful consideration of the methods of Amdahl (1983) and Yang and Caldwell (1988). This formula fully accounts for strain-rate effects, loading condition, velocity and vessel size, and is recommended for central bow collisions with a rigid infinite plate. It is proposed for merchant vessels with $500\ t - 300,000\ t\ DWT$:

$$F_M\ [MN] = \begin{cases} P_0 \cdot \bar{L} \cdot \sqrt{\bar{E}_{imp} + (5.0 - \bar{L}) \cdot \bar{L}^{1.6}} & \text{for } \bar{E}_{imp} \geq \bar{L}^{2.6} \\ 2.24 \cdot P_0 \cdot \sqrt{\bar{E}_{imp} \cdot \bar{L}} & \text{for } \bar{E}_{imp} < \bar{L}^{2.6} \end{cases} \tag{4.5}$$

where the following definitions hold:

- $P_0 = 210\ MN$ is a reference collision load
- $\bar{L} = \frac{L_{BP}\ [m]}{275}$ is a dimensionless ship length
- $E_{imp} = \frac{1}{2} \cdot m_x \cdot V^2$ is the initially available kinetic energy. The ship mass should be enhanced with a 5% added mass due to the surge motion.
- $\bar{E}_{imp} = \frac{E_{imp}\ [MJ]}{1425}$ is a dimensionless ship collision energy

Results of Pedersen et al. (1993)'s formula and discussion

The application of Equation 4.5 for the prediction of the maximum crushing force F_M for the examined velocities (3 kn, 6 kn and 9 kn) yields the results presented in Table 4.1.

Results of application of Pedersen's formula (1993) for the maximum collision force			
	V = 3 kn	V = 6 kn	V = 9 kn
FEA simulation F_M [MN]:	85.22	135.85	244.24
Prediction of Pedersen's formula F_M [MN]:	96.99	193.98	240.98
Divergence percentage [%]:	13.8%	42.8%	-1.3%

Table 4.1: Results of application of Pedersen et al. (1993)'s formula for F_M calculation

Equation 4.5 overestimates noticeably and significantly the results of the 3 kn and the 6 kn simulation, respectively. This is mainly attributed to the calibration of the lower branch of Equation 4.5, which is in these cases utilized to yield the resulting F_M.

Pedersen et al. (1993) also commented that the maximum force depends on the structural type and shape of the bow so much so, that a scatter of 50% when employing simple formulae is not uncommon, due to the inability to capture the behavior of all ship types, bow strengthening systems and loading conditions. Excellent performance of Equation 4.5 is observed on the 9 kn simulation, where the upper branch of the equation is applied.

Nevertheless, the author recommends use of Equation 4.5 in lieu of FEA results when performing probabilistic analyses, in order to reduce computational costs (e.g. during a FSA). In the present study, the comparison between FEA results and this method yields a

somewhat acceptable correlation for the lower-speed collision simulation, an unacceptable result for the intermediate-speed collision simulation, and a surprisingly good agreement for the high-speed collision simulation.

4.4.2 Method of Zhang et al. (2004)

More recently, Zhang et al. (2004) proposed a simple formula to evaluate the maximum crushing force F_M expected during head-on collisions, as a function of collision velocity. The formula has been derived for longitudinally stiffened bulk carriers and oil tankers, with $L \geq 150\ m$, since some parameters were calibrated based on such ship types:

$$F_M\ [MN] = 10^{-3} \cdot 1.27 \cdot L^{2.08} \cdot V^{0.67} \tag{4.6}$$

where L denotes the ship Rule Length in m (as defined in CSR (2023), Part 1, Chapter 1, Section 4, Paragraph 3.1.1), and V denotes the collision speed in m/sec.

Results of Zhang et al. (2004)'s formula and discussion

The application of Equation 4.6 for the prediction of the maximum crushing force F_M for the examined velocities (3 kn, 6 kn and 9 kn) yields the results presented in Table 4.2:

Application of Zhang and Pedersen's formula (2004)			
	V=3kn	V=6kn	V=9kn
V [m/sec]	1.543	3.086	4.630
FEA simulation F_M [MN]:	85.22	135.85	244.24
Prediction of Zhang and Pedersen's formula F_M [MN]:	86.90	138.26	181.42
Divergence percentage [%]:	2.0%	1.8%	-25.7%

Table 4.2: Results of application of Zhang et al. (2004)'s formula for F_M calculation

Equation 4.6 predicts with excellent accuracy the maximum crushing force in the case of the low-speed and the intermediate-speed collision. However, it seriously underestimates the maximum crushing force F_M in the case of the high-speed collision. This underestimation trend is also observed by the author, when evaluating head-on collisions with a speed of $7 - 11$ kn, especially when compared to the method of Pedersen et al. (1993).

However, considering the simplicity of this formula, it is surprisingly accurate, compared to the present study's FEA results.

4.5 Simple formulae for the maximum penetration depth

In a similar fashion with subsection 4.4.2, Zhang et al. (2004) also proposed a simple formula for the calculation of the maximum penetration expected during head-on collisions. This formula is, much like subsection 4.4.2, derived for longitudinally stiffened bulk carriers and oil tankers with $L \geq 150\ m$, under the assumption that all of the initially available kinetic energy is absorbed by the ship bow structure, and through approximation of the response curve as a non-linear spring (see section 4.6 for additional information). The formula suggested is:

$$d_{max}\ [m] = \frac{0.069}{0.75} \cdot (\frac{MV^2}{L^{1.47}})^{0.67} \tag{4.7}$$

The application of Equation 4.7 for the prediction of the maximum penetration d_{max} for the examined velocities (3 kn, 6 kn and 9 kn) yields the results presented in Table 4.3:

Application of Zhang and Pedersen's formula (2004)			
	V=3kn	V=6kn	V=9kn
V [m/sec]	1.543	3.086	4.630
FEA simulation d_{max} [m]:	1.92	4.30	7.16
Prediction of Zhang and Pedersen's formula d_{max} [m]:	1.79	4.54	7.82
Divergence percentage [%]:	-6.6%	5.6%	9.2%

Table 4.3: Results of application of Zhang et al. (2004)'s formula for d_{max} calculation

Good agreement is observed, compared with the present study's FEA results, especially considering the simplicity of the proposed formula.

4.6 Simple formulae for the force-deformation curve

In a similar fashion with subsection 4.4.2 and section 4.5, Zhang et al. (2004) also suggested a simple formula for the determination of the full force-displacement curve, under the assumption that the ship bow is being crushed in a static fashion (an assumption which can hold true under limited penetration depths, as observed in Chapter 3). The ship bow is idealized as a non-linear spring, as:

$$F = K_1 \cdot \sqrt{d} \tag{4.8}$$

which is assumed for values of $d \leq 0.3 \cdot B \approx 10m$.

The author suggests the calculation of K_1 as:

$$K_1\ [kN/\sqrt{m}] = 14.25 \cdot \frac{L^2}{\sqrt{B}} = 84.670 \tag{4.9}$$

The result of application of Equations 4.8 and 4.9 is depicted in Figure 4.5:

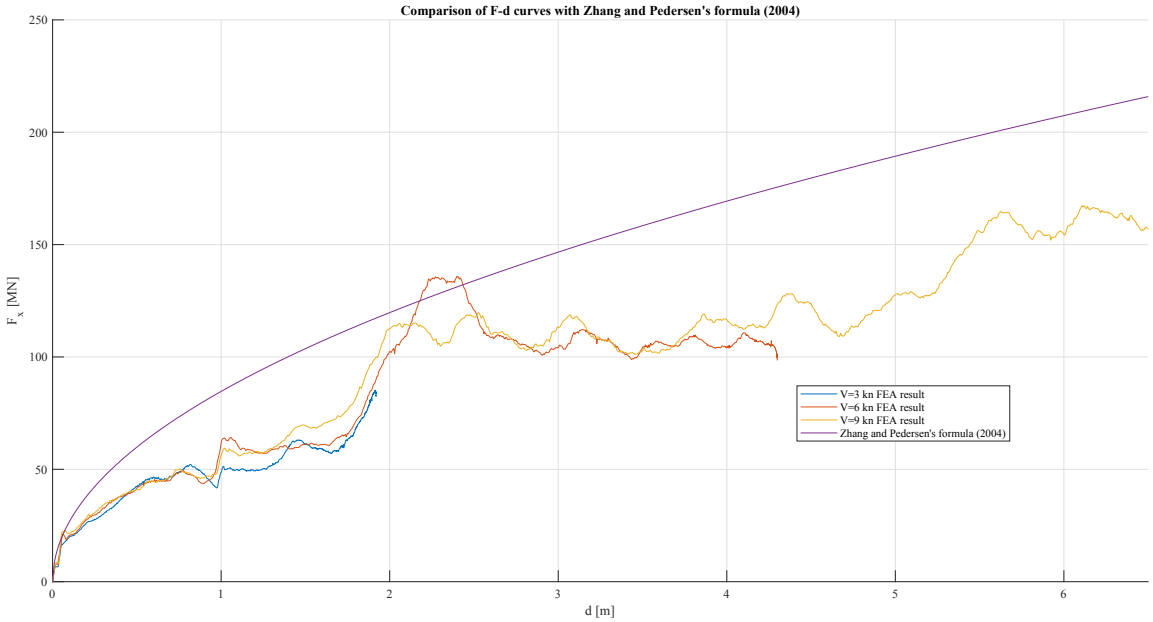

Figure 4.5: Zhang et al. (2004)'s method for the F-d curve, compared with FEA results

Although the general shape of the curve is well-captured (indicating that, indeed, the ship bow behaves as a non-linear spring), a large overestimation of its response is observed, indicating that a better calculation method for the coefficient K_1 should be established. Care should be exercised when applying Equations 4.8 and 4.9, as direct application may lead to nonconservative results for the bow structure response.

4.7 Conclusions from comparisons with analytical methodologies

In the present Chapter, an extensive application of simplified analytical methods has been performed, in order to assess the reliability of the FEA results.

- For the calculation of the mean crushing forces as a function of penetration depth (approximation of the force-displacement curve as a piecewise linear function), discretization to L-, T- and X-elements has been performed. The method of Yang and Caldwell (1988) produces relatively accurate predictions, with Amdahl (1983)'s method also being reliable. An even better prediction is achieved by averaging the individual methods, producing results with acceptable agreement with FEA results.

- For the calculation of the maximum crushing forces, Pedersen et al. (1993)'s formula accurately captured the maximum crushing strength in high-speed collisions, whilst Zhang et al. (2004)'s formula performs better on the low- and intermediate-speed collisions.

- For the maximum penetration depth, Zhang et al. (2004)'s formula produced very good agreement with the FEA simulations.

- Finally, when approximating the bow response as a non-linear spring, as suggested by Zhang et al. (2004), the forces are overestimated, signifying a need for better calibration of the method coefficients.

Although the results of the comparisons do not always exhibit satisfactory agreement, the simplified analytical methods produced results well-correlated with FEA results in most cases, especially considering their straighforward application, and the inherent model uncertainties/assumptions. Thus, it appears that the present study's FEA model has been well-calibrated, and its results can be considered satisfactory.

Chapter 5

Conclusion and future work

5.1 Conclusions from present work results

The most important results of the present study are summarized below:

1. The mesh convergence study conducted indicates that a good compromise between reliability and cost-effectiveness is achieved, when employing a general element size of 50 mm ($3t$), for the simulation of head-on collisions using FEA.

2. The available kinetic energy to cause structural damage is predominantly dissipated through plastic strains; the contribution of friction dissipation is low enough to be ignored in such analyses ($<5\%$).

3. Even in the high-speed simulation ($9\ kn$), the damage extent is limited to fore of the collision bulkhead.

4. The dominant structural member to dissipate the plastic strain energy is the bulb, absorbing the forces exerted by $> 70\%$, and the plastic strain energy by $> 80\%$.

5. The assumption of static bow deformation (ignoring dynamic phenomena) holds for limited penetrations (just before stem contact). Additionally, even after stem contact, their effect on the exhibited forces is no more than 20%.

6. Simplified analytical formulae based on division of bow sections to L-, T- and X-elements can predict the force-displacement curve during head-on collisions with acceptable accuracy, and may be employed instead of FEA modelling, when the

computational resources and the available time are limited. Better predictions can be achieved by averaging the different individual methods' results.

7. Care should be exercised when applying simple formulae to calculate critical parameters of head-on collisions (such as F_m, F_M and d_{max}). Although they may often perform well, especially considering their simplicity, they might also produce both conservative and non-conservative results for the structure's actual behavior.

5.2 Recommendations for future work

Some directions for possible future research are outlined below:

- Since the bow form examined in the present study is a bulbous blunt form, an examination of the structural behavior of different bow forms (sharp, non-bulbous) would be beneficial, in order to compare the advantages of other bow designs, and their respective stiffening systems, for performance against head-on collision events.
- A comparison of FEA results without considering the materials' strain-rate effects, with the present study's results, could assist in quantifying the strain-rate effect on the bow response and the most important collision parameters (F_M, d_{max}).
- The inclusion of a failure criterion, experimentally calibrated for crushing / compression-dominated analyses would be an interesting modelling addition.
- Although the forces exerted on the hull structure due to hull-girder loads are negligible, an inclusion of the effect of hull-girder deflections/rotations would be of interest, since it can also induce energy dissipation due to bulb bending.
- A FEA simulation of static bow crushing, as well as simulations employing constant-speed techniques (instead of initial-speed techniques) could produce important results, regarding the extent of the static bow crushing assumption.
- An investigation on the effect of the plate collision angle (either on the XY or the YZ plane) could be conducted. This, however, imposes the additional problem of coupled external/internal mechanics simulation, owing to the hydrodynamic interaction.

References

Abaqus 6.14 (2014), 'Abaqus/CAE User's Guide 6.14'.

Abramowicz, W. (1994), 'Crushing resistance of "T", "Y" and "X" sections', Joint MIT-Industry Program on Tanker Safety, Report No. 24 .

Abubakar, A. and Dow, R. (2013), 'Simulation of ship grounding damage using the finite element method', International Journal of Solids and Structures 50(5), 623–636.

Akita, Y., Ando, N., Fujita, Y. and Kitamura, K. (1972), 'Studies on collision-protective structures in nuclear powered vessels', Nuclear Engineering and Design 19(2), 365–401.

Amdahl, J. (1983), 'Energy absorption in ship-platform impacts (Ph.D. Thesis)', Norwegian Institute of Technology (Report No. UR 83-84) .

Chen, J., Zhu, L. and Pedersen, P. (2019), On dynamic effect of bulbous bow crushing, in 'Proceedings of the 29th International Ocean and Polar Engineering Conference', pp. 4288–4295.

Choung, J. (2013), 'Dynamic hardening behaviors of various marine structural steels considering dependencies on strain rate and temperature', Marine Structures 32, 49–67.

Cowper, G. and Symonds, P. (1957), 'Strain hardening and strain-rate effects in the impact loading of cantilever beams', Brown University Providence R. I. (Technical Report No. 28) .

CSR (2023), 'Common Structural Rules for Bulk Carriers and Oil Tankers - 01 Jan 2023 consolidated', The International Association of Classification Societies .

DNV-RP-C208 (2019), 'Determination of structural capacity by non-linear finite element analysis methods', Recommended Practice .

Ehlers, S. (2011), 'A review of collision and grounding damage assessment methods', Marine Systems and Ocean Technology 6, 5–15.

Ehlers, S., Broekhuijsen, J., Alsos, H., Biehl, F. and Tabri, K. (2008), 'Simulating the collision response of ship side structures: a failure criteria benchmark study', International Shipbuilding Progress 55(1), 127–144.

EMSA (2022), 'Annual overview of marine casualties and incidents'.

Hareide, O., Brubak, L. and Pettersen, T. (2013), Modelling ship grounding with finite elements, in 'Proceedings of the 26th Nordic Seminar on Computational Mechanics', pp. 88–91.

IMO (2018), 'Revised guidelines for Formal Safety Assessment (FSA) for use in the IMO rule-making process', MSC-MEPC.2/Cirv.12/Rev.2 .

Iqbal, J. and Shifan, Z. (2018), 'Modeling and simulation of ship structures using Finite Element Method', International Journal of Industrial and Manufacturing Engineering 12(7), 874–880.

Jones, N. (1989), Some comments on the modelling of material properties for dynamic structural plasticity, in 'Mechanical Properties of Materials at High Rates of Strain', pp. 435–445.

Jones, N. (2013), 'The credibility of predictions for structural designs subjected to large dynamic loadings causing inelastic behaviour', International Journal of Impact Engineering 53, 106–114.

Kitamura, O. (2000), 'Buffer bow design for the improved safety of ships', IMO, MEPC45/INF.5, Annex .

Ko, Y., Kim, S., Sohn, J. and Paik, J. (2018), 'A practical method to determine the dynamic fracture strain for the nonlinear finite element analysis of structural crashworthiness in ship-ship collisions', Ships and Offshore Structures 13(4), 412–422.

Kristiansen, S. and Haugen, S. (2023), Maritime Transportation: Safety Management and Risk Analysis, Routledge.

Lettnin, H. (1973), The safety containment for nuclear powered ships, Technical report, IASMiRT, J2- Design and Structural Analysis of Containment Structures (No. 2).

Liu, B., Pedersen, P., Zhu, L. and Zhang, S. (2018a), 'Review of experiments and calculation procedures for ship collision and grounding damage', Marine Structures 59, 105–121.

Liu, B., Villavicencio, R., Zhang, S. and Soares, C. (2017), 'A simple criterion to evaluate the rupture of materials in ship collision simulations', Marine Structures 54, 92–111.

Liu, K., Liu, B., Villavicencio, R., Wang, Z. and Soares, C. (2018b), 'Assessment of material strain rate effects on square steel plates under lateral dynamic impact loads', Ships and Offshore Structures 13(2), 217–225.

Lloyd's Register (2018), 'Rules and Regulations for the Classification of Ships'.

Lützen, M., Simonsen, B. and Pedersen, P. (2000), Rapid prediction of damage to struck and striking vessels in a collision event, in 'SSC/SNAME/ASNE Symposium'.

MARPOL 73/78 (1992), 'International Convention for the Prevention of Pollution from Ships, 1973, as modified by the protocol of 1978 relating thereto', International Maritime Organization .

Minorsky, V. (1959), 'An analysis of ship collisions with reference to protection of nuclear power plants', Journal of Ship Research 3(2), 1–4.

OPA (1990), 'The Oil Pollution Act of 1990 (OPA 90)', 33 U.S.C. ch. 40, par. 2701 .

Paik, J. (2007a), 'Practical techniques for finite element modelling to simulate structural crashworthiness in ship collision and grounding (Part I: Theory)', Ships and Offshore Structures 2(1), 69–80.

Paik, J. (2007b), 'Practical techniques for finite element modelling to simulate structural crashworthiness in ship collisions and grounding (Part II: Verification)', Ships and Offshore Structures 2(1), 81–85.

Paik, J. (2018), Ultimate Limit State Analysis and Design of Plated Structures, (2nd edition), John Wiley and Sons, Incorporated.

Paik, J., Chung, J. and Chun, M. (1996), 'On quasi-static crushing of a stiffened square tube', Journal of Ship Research 40(03), 258–267.

Pedersen, P. (2010), 'Review and application of ship collision and grounding analysis procedures', Marine Structures 23(3), 242–262.

Pedersen, P., Valsgard, S., Olsen, D. and Spangenberg, S. (1993), 'Ship impacts: Bow collisions', International Journal of Impact Engineering 13(2), 163–187.

Pedersen, P., Zhang, S. and Villavicencio, R. (2019), Probability and Mechanics of Ship Collision and Grounding, Butterworth-Heinemann.

Petersen, M. (1982), 'Dynamic of ship collisions', Ocean Engineering 9(4), 295–329.

Samuelides, M. (2009), Design against collision: Half a century of research, in 'Proceedings of the tenth international marine design conference', pp. 456–475.

Samuelides, M. (2015), 'Recent advances and future trends in structural crashworthiness of ship structures subjected to impact loads', Ships and Offshore Structures 10(5), 488–497.

Samuelides, M., Ventikos, N. and Gemelos, I. (2009), 'Survey on grounding incidents: Statistical analysis and risk assessment', Ships and Offshore Structures 4(1), 55–68.

Servis, D., Samuelides, M., Louka, T. and Voudouris, G. (2002), 'Implementation of finite element codes for the simulation of ship-ship collisions', Journal of Ship Research 46(4), 239–247.

Sever, N., Choi, C., Yang, X. and Altan, T. (2011), 'Determining the flow stress curve with yield and ultimate tensile strengths (part ii)', Stamp J July/August .

Storheim, M. and Amdahl, J. (2015), 'On the sensitivity to work hardening and strain-rate effects in nonlinear FEM analysis of ship collisions', Ships and Offshore Structures 12(1), 100–115.

Storheim, M., Amdahl, J. and Martens, I. (2015), 'On the accuracy of fracture estimation in collision analysis of ship and offshore structures', Marine Structures 44, 254–287.

Tautz, I., Schottelndreyer, M., Gaurke, J., Lehmann, E. and Fricke, W. (2013), Structural design of a bulbous bow with regard to collision safety, in '5th International Conference on Computational Methods in Marine Engineering (MARINE 2013)', pp. 901–911.

Van de Graaf, B., Broekhuijsen, J., Vredeveldt, A. and van de Ven, A. (2004), Construction aspects for the Schelde Y-shape crashworthy hull structure, in 'Proceedings of the 3rd International Conference on Collision and Grounding of Ships (ICCGS 2004)', pp. 229–233.

Wang, G., Spencer, J. and Chen, Y. (2002), 'Assessment of ship's performance in accidents', Marine Structures 15(4), 313–333.

Woisin, G. (1976), 'Die kollisionsversuche der GKSS (in german)', Jahrbuch der Shiffbautechniscehn Gesselschaft 70.

Yamada, Y. and Endo, H. (2005), 'Collapse mechanism of the buffer bow structure on axial crushing', International Journal of Offshore Polar Engineering 15(02), 147–154.

Yamada, Y. and Pedersen, P. (2008), 'A benchmark study of procedures for analysis of axial crushing of bulbous bows', Marine Structures 21(2), 257–293.

Yang, P. and Caldwell, J. (1988), 'Collision energy absorption of ships' bow structures', International Journal of Impact Engineering 7(2), 181–196.

Zhang, S., Pedersen, P. and Ocakli, H. (2004), 'Crushing of ship bows in head-on collision', International Journal of Maritime Engineering 146, 39–46.

Appendix A

Scantlings of Bow Structure

In this Appendix, the analytical scantlings and geometrical entities, designed in the Abaqus/CAE environment for the bow strength assessment of the Bulk Carrier ship under consideration, are presented, in table format.

A.1 Outer Shell for the bow hull

The outer shell has been designed based on surface extrapolation of waterlines, available from the vessel Lines Plan. The outer side shell has been assigned a thickness of t=19.5 (15.5) mm out of AH36 steel, while the bottom (flat part) has been assigned a thickness of t=23.5 (20.5) mm out of AH36 steel (see for reference Figure A.1).

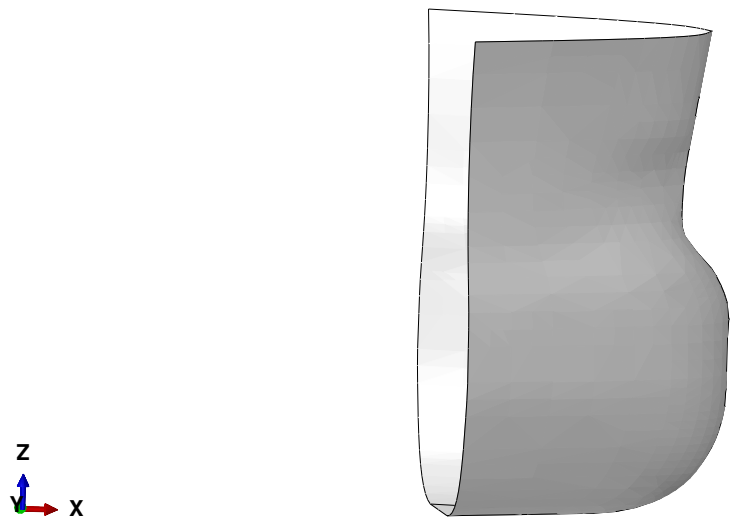

Figure A.1: Snapshot of Outer Shell (starboard view) in Abaqus/CAE environment

A.2 Deck at 18900 mm scantlings (Upper Deck)

For the Upper Deck of the bow structure, a deck at 18900 mm height is considered, which comprises of the items presented in Table A.1 and depicted in Figure A.2:

Deck at 18900 mm stiffeners (PS, symmetrical on SS)					
Name	Type	Dimensions (h_w x t_w) [mm x mm]	Material	Distance (towards port side) from CL [mm]	Length [mm]
CL Girder	T-bar	450 x 150 x 11.5 (9.5) x 14 (12)	Grade A	0	8400
L1	Flat bar	180 x 9 (7)	Grade A	636	8400
L2	Flat bar	180 x 9 (7)	Grade A	1272	8400
L3	Flat bar	180 x 9 (7)	Grade A	2072	8400
L4	Flat bar	180 x 9 (7)	Grade A	2792	8400
L5	T-bar	450 x 150 x 11.5 (9.5) x 14 (12)	Grade A	3552	8400
L6	Flat bar	180 x 9 (7)	Grade A	4312	6600
L7	Flat bar	180 x 9 (7)	Grade A	5072	6600
L8	Flat bar	180 x 9 (7)	Grade A	5832	4800
L9	T-bar	450 x 150 x 11.5 (9.5) x 14 (12)	Grade A	6592	4800
L10	Flat bar	180 x 9 (7)	Grade A	7227	2400
L11	Flat bar	180 x 9 (7)	Grade A	7862	2400
L12	Flat bar	180 x 9 (7)	Grade A	8497	2400

Deck Thickness [mm]	Material
14.5 (10)	AH36

Frames at 18900 mm Deck				
Frame No	Type	Dimensions (h_w x b_f x t_w x t_f) [mm x mm x mm x mm]	Material	Horizontal distance from Collision Bulkhead [mm]
223	T-bar	450 x 150 x 11.5 (9.5) x 14 (12)	Grade A	2400
227	T-bar	450 x 150 x 11.5 (9.5) x 14 (12)	Grade A	4800
230	T-bar	450 x 150 x 11.5 (9.5) x 14 (12)	Grade A	6600
233	T-bar	450 x 150 x 11.5 (9.5) x 14 (12)	Grade A	8400

Table A.1: Scantlings of Deck at 18900 mm

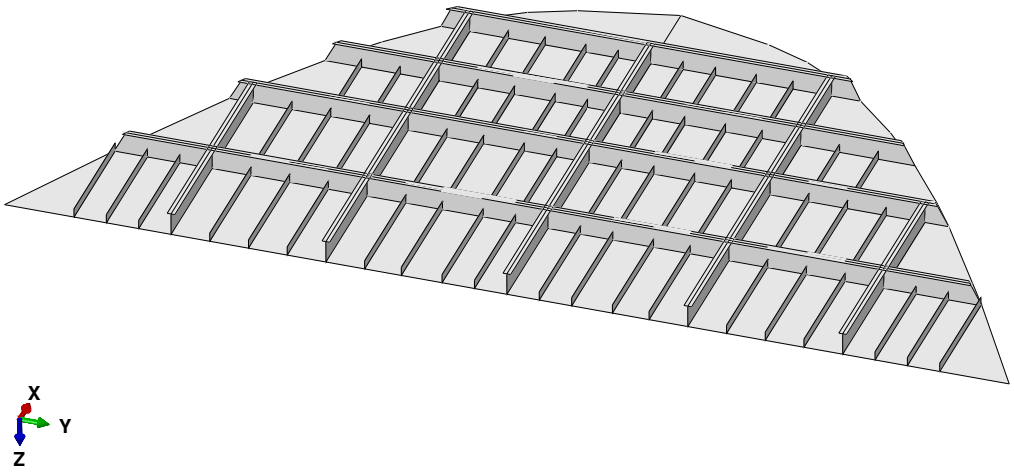

Figure A.2: Bottom view of Deck at 18900 mm (Upper) in Abaqus/CAE environment

A.3 Deck at 13600 mm scantlings

For the intermediate deck at a height of 13600 mm of the ship under consideration, the analytical scantlings determined are presented in Table A.2 and depicted in Figure A.3:

Deck at 13600 mm stiffeners (PS, symmetrical on SS)					
Name	Type	Dimensions (h_w x t_w) [mm x mm]	Material	Distance (towards port side) from CL [mm]	Length [mm]
CL Girder	T-bar	350 x 120 x 11.5 (9.5) x 12 (10)	Grade A	0	8400
L1	Flat bar	180 x 8 (6)	Grade A	636	2400
L2	Flat bar	180 x 8 (6)	Grade A	1272	2400
L3	Flat bar	180 x 8 (6)	Grade A	2072	2400
L4	Flat bar	180 x 8 (6)	Grade A	2792	2400
L5	T-bar	350 x 120 x 11.5 (9.5) x 12 (10)	Grade A	3552	4800
L6	Flat bar	180 x 8 (6)	Grade A	4312	2400
L7	Flat bar	180 x 8 (6)	Grade A	5072	2400
L8	Flat bar	180 x 8 (6)	Grade A	5832	2400
L9	T-bar	350 x 120 x 11.5 (9.5) x 12 (10)	Grade A	6592	2400

Deck Thickness [mm]	Material
10 (8)	Grade A

Frames at 13600 mm Deck				
Frame No	Type	Dimensions (h_w x b_f x t_w x t_f) [mm x mm x mm x mm]	Material	Horizontal distance from Collision Bulkhead [mm]
223	T-bar	350 x 120 x 11.5 (9.5) x 12 (10)	Grade A	2400
227	T-bar	350 x 120 x 11.5 (9.5) x 12 (10)	Grade A	4800
230	T-bar	350 x 120 x 11.5 (9.5) x 12 (10)	Grade A	6600
233	Flat bar	180 x 8 (6)	Grade A	8400

Table A.2: Scantlings of Deck at 13600 mm

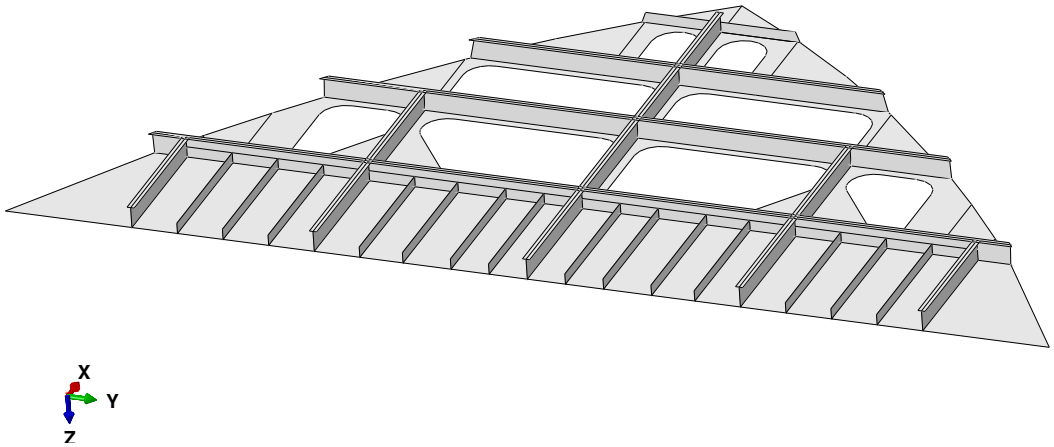

Figure A.3: Bottom view of Deck at 13600 mm in Abaqus/CAE environment

It is noted that the deck at 13600 mm exhibits large openings, i.e. it is not watertight.

A.4 Deck at 9520 mm scantlings

For the intermediate deck at a height of 9520 mm of the ship under consideration, the analytical scantlings determined are presented in Table A.3 and depicted in Figure A.4:

Deck at 9520 mm stiffeners (PS, symmetrical on SS)					
Name	Type	Dimensions (h_w x t_w) [mm x mm]	Material	Position from CL [mm]	Length [mm]
CL Girder	T-bar	600 x 250 x 12.5 (9.5) x 15 (11.5)	AH36	0	8400
L1	Flat bar	200 x 9 (6)	AH36	636	8400
L2	Flat bar	200 x 9 (6)	AH36	1272	8400
L3	Flat bar	200 x 9 (6)	AH36	2072	8400
L4	Flat bar	200 x 9 (6)	AH36	2792	8400
L5	T-bar	600 x 250 x 12.5 (9.5) x 15 (11.5)	AH36	3552	8400
L6	Flat bar	200 x 9 (6)	AH36	4312	6600
L7	Flat bar	200 x 9 (6)	AH36	5072	6600
L8	Flat bar	200 x 9 (6)	AH36	5832	4800
L9	T-bar	600 x 250 x 12.5 (9.5) x 15 (11.5)	AH36	6592	4800
L10	Flat bar	200 x 9 (6)	AH36	7227	2400
L11	Flat bar	200 x 9 (6)	AH36	7862	2400

Deck Thickness [mm]	Material
11 (8.5)	AH36

Frames at 9520 mm Deck				
Frame No	Type	Dimensions (h_w x b_f x t_w x t_f) [mm x mm x mm x mm]	Material	Distance from Collision Blkhd [mm]
223	T-bar	600 x 250 x 12.5 (9.5) x 15 (11.5)	AH36	2400
227	T-bar	600 x 250 x 12.5 (9.5) x 15 (11.5)	AH36	4800
230	T-bar	600 x 250 x 12.5 (9.5) x 15 (11.5)	AH36	6600
233	T-bar	600 x 250 x 12.5 (9.5) x 15 (11.5)	AH36	8400

Table A.3: Scantlings of Deck at 9520 mm

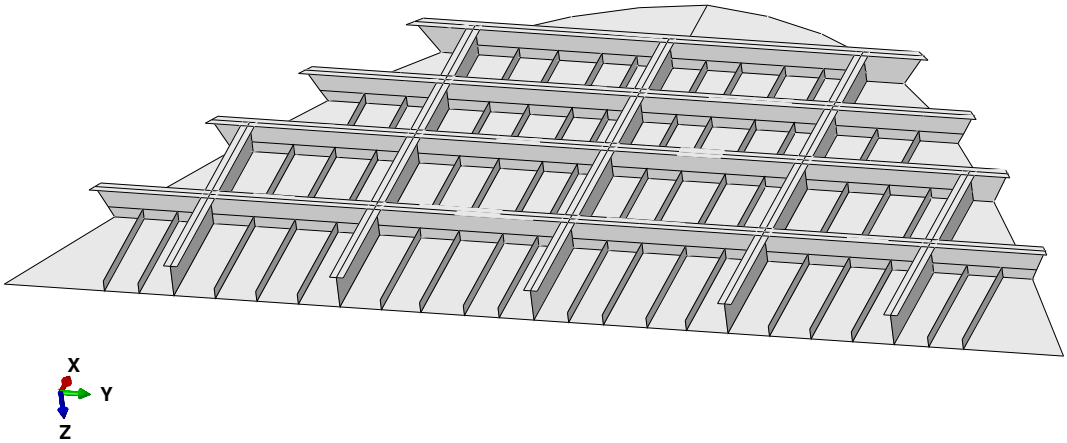

Figure A.4: Bottom view of Deck at 9520 mm in Abaqus/CAE environment

A.5 Deck at 5440 mm scantlings

For the intermediate deck at a height of 5440 mm of the ship under consideration, the analytical scantlings determined are presented in Table A.4 and depicted in Figure A.5:

Deck at 5440 mm stiffeners (PS, symmetrical on SS)					
Name	**Type**	**Dimensions (h_w x t_w) [mm x mm]**	**Material**	**Position from CL [mm]**	**Length [mm]**
CL Girder	T-bar	350 x 120 x 12.5 (9.5) x 12 (8.5)	Grade A	0	8400
L1	Flat bar	180 x 9 (6)	Grade A	636	2400
L2	Flat bar	180 x 9 (6)	Grade A	1272	2400
L3	Flat bar	180 x 9 (6)	Grade A	2072	2400
L4	Flat bar	180 x 9 (6)	Grade A	2792	2400
L5	T-bar	350 x 120 x 12.5 (9.5) x 12 (8.5)	Grade A	3552	4800
L6	Flat bar	180 x 9 (6)	Grade A	4312	2400
L7	Flat bar	180 x 9 (6)	Grade A	5072	2400
L8	Flat bar	180 x 9 (6)	Grade A	5832	2400
L9	T-bar	350 x 120 x 12.5 (9.5) x 12 (8.5)	Grade A	6592	4800
L10	Flat bar	180 x 9 (6)	Grade A	7227	2400
L11	Flat bar	180 x 9 (6)	Grade A	7862	2400
L12	Flat bar	180 x 9 (6)	Grade A	8497	2400
L13	T-bar	350 x 120 x 12.5 (9.5) x 12 (8.5)	Grade A	9130	2400

Deck Thickness [mm]	**Material**
13.5 (10.5)	Grade A

Frames at 5440 mm Deck				
Frame No	**Type**	**Dimensions (h_w x b_f x t_w x t_f) [mm x mm x mm x mm]**	**Material**	**Distance from Collision Blkhd [mm]**
223	T-bar	350 x 120 x 12.5 (9.5) x 12 (8.5)	Grade A	2400
227	T-bar	350 x 120 x 12.5 (9.5) x 12 (8.5)	Grade A	4800
230	T-bar	350 x 120 x 12.5 (9.5) x 12 (8.5)	Grade A	6600
233	Does not have a support at frame 233			

Table A.4: Scantlings of Deck at 5440 mm

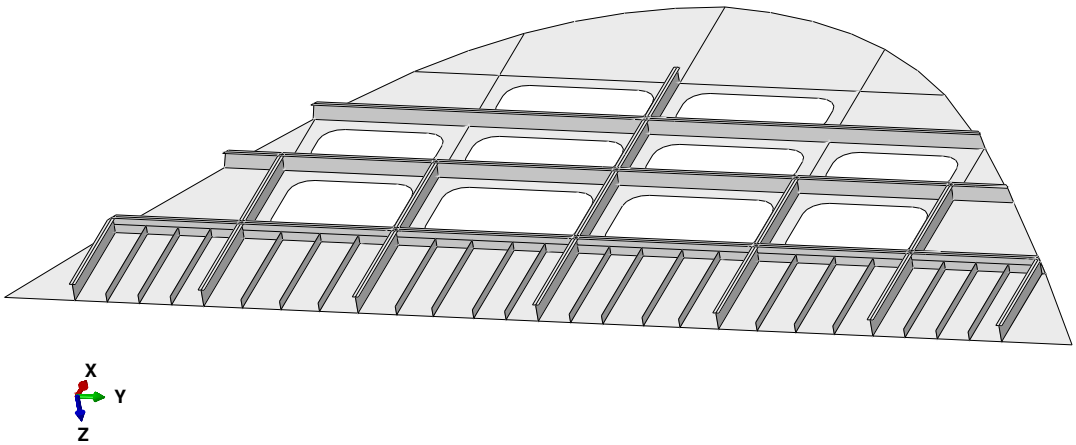

Figure A.5: Bottom view of Deck at 5440 mm in Abaqus/CAE environment

It is noted that the deck at 5440 mm also exhibits large openings (non-watertight).

A.6 Web Frames at sides scantlings

Frames 223 and 227 of the modelled bow structure are strengthened with T-bars in the transverse direction. The analytical scantlings are presented in Table A.5 and depicted in Figure A.6:

Frame 223 side transverse strengthening			
Name	**Type**	**Dimensions (h_w x b_f x t_wx t_f) [mm x mm x mm x mm]**	**Material**
Deck 13600 mm to Upper Deck	T-bar	800 x 150 x 14 (12) x 16 (14)	AH36
Deck 9520 mm to Deck 13600 mm	T-bar	800 x 250 x 14 (12) x 16 (14)	AH36
Deck 5440 mm to Deck 9520 mm	T-bar	700 x 150 x 14 (12) x 16 (14)	AH36
Tank Top to Deck 5440 mm	T-bar	800 x 250 x 14 (11) x 16 (12.5)	AH36
Frame 227 side transverse strengthening			
Name	**Type**	**Dimensions (h_w x b_f x t_wx t_f) [mm x mm x mm x mm]**	**Material**
Deck 13600 mm to Upper Deck	T-bar	800 x 250 x 14 (12) x 16 (14)	AH36
Deck 9520 mm to Deck 13600 mm	T-bar	800 x 250 x 15 (13) x 17 (15)	AH36
Deck 5440 mm to Deck 9520 mm	T-bar	700 x 150 x 14 (12) x 16 (14)	AH36
Tank Top to Deck 5440 mm	T-bar	850 x 250 x 14 (11) x 16 (12.5)	AH36
Note: Frames 230 & 233 are not supported at sides.			

Table A.5: Scantlings of strengthened Web Frames

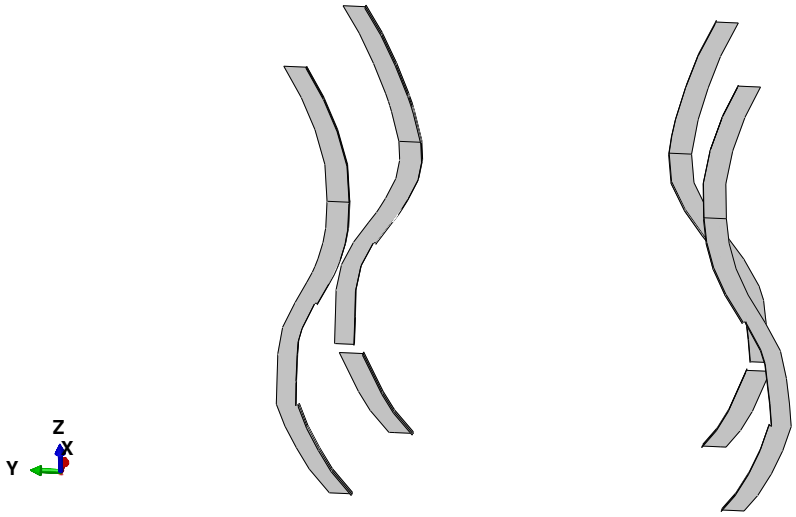

Figure A.6: Aft view of strengthened Web Frames 223-227 in Abaqus/CAE environment

A.7 Double Bottom structure scantlings

The double bottom structure comprises of a Tank Top deck (at a height of 2000 mm), the respective longitudinal stiffeners and girders, the frame supports of the grillage, as well as the bottom longitudinal stiffeners. The analytical scantlings are presented in Table A.6 and depicted in Figure A.7:

Tank Top stiffeners (PS, symmetrical on SS)					
Name	Type	Dimensions (h_w x t_w) [mm x mm]	Material	Position from CL [mm]	Length [mm]
CL Girder	Girder	2000 x 13 (10.5)	AH36	0	9600
Stiff. 1 of CL Girder	Flat bar	260 x 10 (7)	AH36	0	8400
Stiff. 2 of CL Girder	Flat bar	260 x 10 (7)	AH36	0	8400
L1	Flat bar	320 x 13 (10)	AH36	636	9600
L2 Girder	Girder	2000 x 15.5 (12.5)	Grade A	1272	9600
Stiff. 1 of L2 Girder	Flat bar	200 x 10 (7)	AH36	0	8400
Stiff. 2 of L2 Girder	Flat bar	200 x 10 (7)	AH36	0	8400
L3	Flat bar	320 x 13 (10)	AH36	2072	2400
L4	Flat bar	320 x 13 (10)	AH36	2792	2400
L5	Flat bar	320 x 13 (10)	AH36	3552	2400
L6 Girder	Girder	2000 x 14 (11)	Grade A	4312	6600
Stiff. 1 of L6 Girder	Flat bar	160 x 9 (6)	AH36	0	4800
Stiff. 2 of L6 Girder	Flat bar	160 x 9 (6)	AH36	0	4800
L7	Flat bar	320 x 13 (10)	AH36	5072	2400
L8	Flat bar	320 x 13 (10)	AH36	5832	4800
L9 Girder	Girder	2000 x 14 (11)	Grade A	6592	2400
L10 Girder	Girder	2000 x 14 (11)	Grade A	7227	2400

Deck Thickness [mm]	Material
15.5 (12.5)	Grade A

Frames at Tank Top				
Frame No	Type	Dimensions (h_w x t_w) [mm x mm]	Material	Distance from Collision Blkhd [mm]
223	Plate	2000 x 15 (12)	AH36	2400
227	Plate	2000 x 14 (11)	Grade A	4800
230	Plate	2000 x 14 (11)	Grade A	6600
233	Plate	2000 x 14 (11)	Grade A	8400
235	Plate	2000 x 14 (11)	Grade A	9600

Bottom stiffeners (PS, symmetrical on SS)					
Name	Type	Dimensions (h_w x t_w) [mm x mm]	Material	Position from CL [mm]	Length [mm]
L1	Flat bar	320 x 13 (10)	AH36	636	9600
L3	Flat bar	320 x 13 (10)	AH36	2072	2400
L4	Flat bar	320 x 13 (10)	AH36	2792	2400
L5	Flat bar	320 x 13 (10)	AH36	3552	2400
L7	Flat bar	320 x 13 (10)	AH36	5072	2400
L8	Flat bar	320 x 13 (10)	AH36	5832	4800

Table A.6: Scantlings of double bottom grillage structure

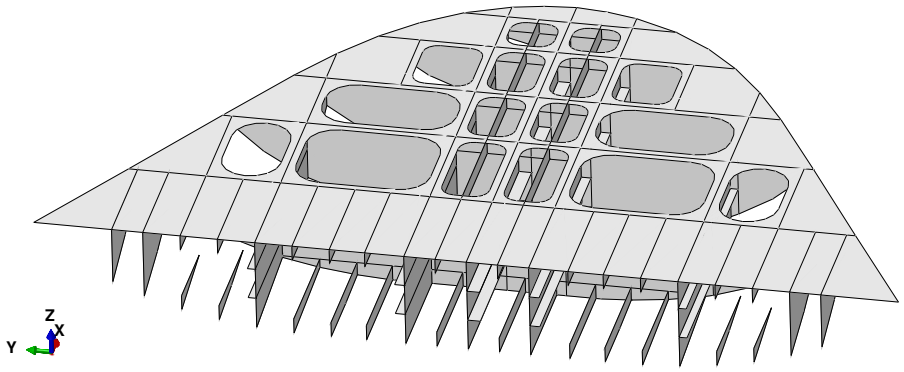

Figure A.7: Top view of double bottom structure in Abaqus/CAE environment

A.8 Horizontal side longitudinals scantlings

The horizontal stiffening system of the ship bow structure comprises of longitudinal stiffeners placed on the bow sides at specific heights above the baseline. The stiffeners' analytical scantlings are presented in Table A.7 and depicted in Figure A.8:

Horizontal Stiffeners at Side Shell				
Name	**Type**	**Dimensions (h_w x t_w) [mm x mm]**	**Material**	**Position ab BL [mm]**
SL.9a	Flat bar	300 x 12 (9)	Grade A	2550
SL.9	Flat bar	280 x 11 (8)	AH36	3100
SL.8	Flat bar	300 x 12 (9)	Grade A	3750
Stiffener of SL.8 on Collision Bulkhead	T-bar	500 x 200 x 12.5 (9.5) x 15 (11.5)	AH36	3750
SL.7	Flat bar	280 x 11 (8)	AH36	4300
SL.6	Flat bar	300 x 12 (9)	Grade A	4850
SL.6a2	Flat bar	400 x 12 (9)	Grade A	6240
SL.6a3	Flat bar	280 x 11 (8)	AH36	7040
Stiffener of SL.6a3 on Collision Bulkhead	T-bar	500 x 200 x 12.5 (9.5) x 15 (11.5)	AH36	7040
SL.6a4	Flat bar	400 x 12 (9)	Grade A	7840
SL.6a5	Flat bar	400 x 12 (9)	Grade A	8640
SL.6a7	Flat bar	260 x 10 (8)	AH36	10220
SL.6a8	Flat bar	260 x 10 (8)	AH36	10900
SL.6a9	Flat bar	260 x 10 (8)	AH36	11400
Stiffener of SL.6a9 on Collision Bulkhead	T-bar	500 x 150 x 11.5 (9.5) x 12 (10)	Grade A	11400
SL.6a10	Flat bar	260 x 10 (8)	AH36	11900
SL.6a11	Flat bar	260 x 10 (8)	AH36	12400
SL.6a12	Flat bar	260 x 10 (8)	AH36	12900
SL.5	Flat bar	260 x 10 (8)	AH36	14050
SL.5a	Flat bar	260 x 10 (8)	AH36	14500
SL.5b	Flat bar	260 x 10 (8)	AH36	15050
SL.4	Flat bar	260 x 10 (8)	AH36	15600
SL.3	Flat bar	260 x 10 (8)	AH36	16100
SL.2	Flat bar	260 x 10 (8)	AH36	16600
SL.1	Flat bar	260 x 10 (8)	AH36	17100
Stiffener of SL.1 on Collision Bulkhead	T-bar	450 x 150 x 11.5 (9.5) x 12 (10)	Grade A	17100

Table A.7: Scantlings of horizontal stiffeners (side girders)

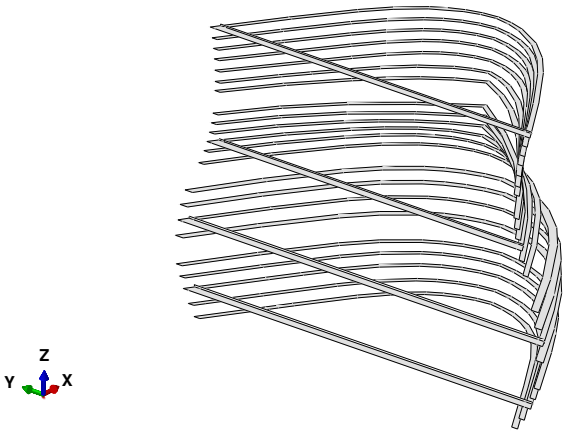

Figure A.8: Top view of bow horizontal stiffening in Abaqus/CAE environment

A.9 Vertical stiffeners scantlings

The vertical stiffening system of the ship bow structure comprises of three cylindrical pillars supporting each of the decks 9520 mm - 13600 mm - 18900 mm, as well as six I-bar girders supporting each of the decks 2000 mm - 5440 mm - 9520 mm. The stiffeners' analytical scantlings are presented in Table A.8 and depicted in Figure A.9:

Vertical Stiffeners (PS, symmetrical on SS)					
Name	**Type**	**Dimensions [all in mm]**	**Material**	**Position coordinate [x, y, z] [mm x mm x mm]**	**Length [mm]**
Pillar 1 Deck 13600 mm to Upper Deck	Cylindrical	Φ219 x 13 (11)	Grade A	[4800, 3552, 13600]	5300
Pillar 2 Deck 13600 mm to Upper Deck	Cylindrical	Φ219 x 13 (11)	Grade A	[4800, 0, 13600]	5300
Pillar 1 Deck 9520 mm to Deck 13600 mm	Cylindrical	Φ219 x 13 (11)	Grade A	[4800, 3552, 9520]	4080
Pillar 2 Deck 9520 mm to Deck 13600 mm	Cylindrical	Φ219 x 13 (11)	Grade A	[4800, 0, 9520]	4080
Vertical Girder 1 Deck 5440 mm to Deck 9520 mm	I-bar	200 x 200 x 14 (11) x 14 (11)	Grade A	[2400, 3552, 5440]	4080
Vertical Girder 2 Deck 5440 mm to Deck 9520 mm	I-bar	200 x 200 x 14 (11) x 14 (11)	Grade A	[4800, 3552, 5440]	4080
Vertical Girder 3 Deck 5440 mm to Deck 9520 mm	I-bar	200 x 200 x 14 (11) x 14 (11)	Grade A	[2400, 6592, 5440]	4080
Vertical Girder 1 Tank Top to Deck 5440 mm	I-bar	200 x 200 x 14 (11) x 14 (11)	Grade A	[2400, 4312, 2000]	3440
Vertical Girder 2 Tank Top to Deck 5440 mm	I-bar	200 x 200 x 14 (11) x 14 (11)	Grade A	[4800, 4312, 2000]	3440
Vertical Girder 3 Tank Top to Deck 5440 mm	I-bar	200 x 200 x 14 (11) x 14 (11)	Grade A	[2400, 6592, 2000]	3440

Table A.8: Scantlings of vertical stiffeners (pillars & girders)

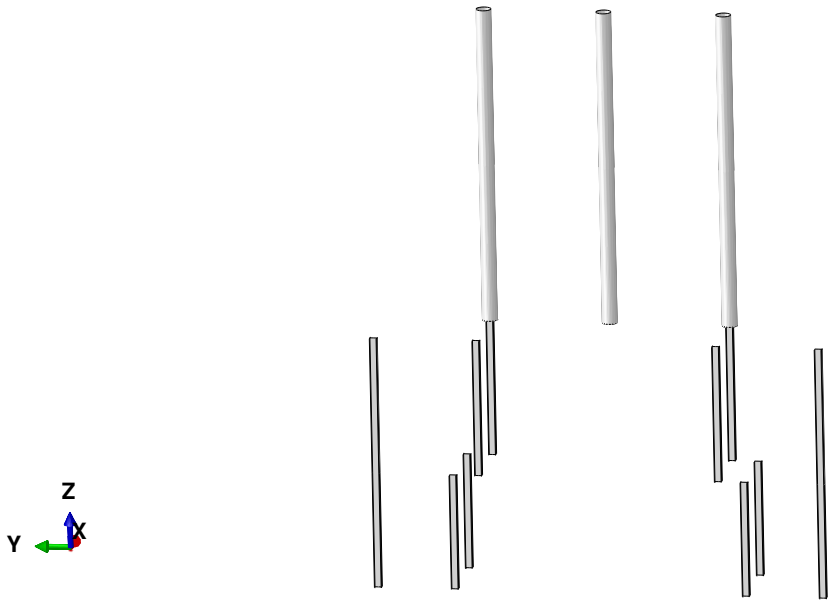

Figure A.9: Aft view of vertical stiffeners in Abaqus/CAE environment

A.10 Stiffeners at CL section scantlings

The CL section stiffening system of the ship bow structure comprises of four T-bars stiffening the foremost part of the CL section of the bow hull. The stiffeners' analytical scantlings are presented in Table A.9 and depicted in Figure A.10:

CL Section Stiffeners at Fore			
Name	Type	Dimensions (h_w x b_f x t_wx t_f) [mm x mm x mm x mm]	Material
Deck 13600 mm to Upper Deck	T-bar	1000 x 150 x 16 (14) x 16 (14)	AH36
Deck 9520 mm to Deck 13600 mm	T-bar	850 x 150 x 16 (14) x 16 (14)	AH36
Deck 5440 mm to Deck 9520 mm	T-bar	1880 x 250 x 16 (14) x 16 (14)	AH36
Tank Top to Deck 5440 mm	T-bar	1880 x 250 x 16 (14) x 16 (14)	AH36

Table A.9: Scantlings of CL section stiffeners

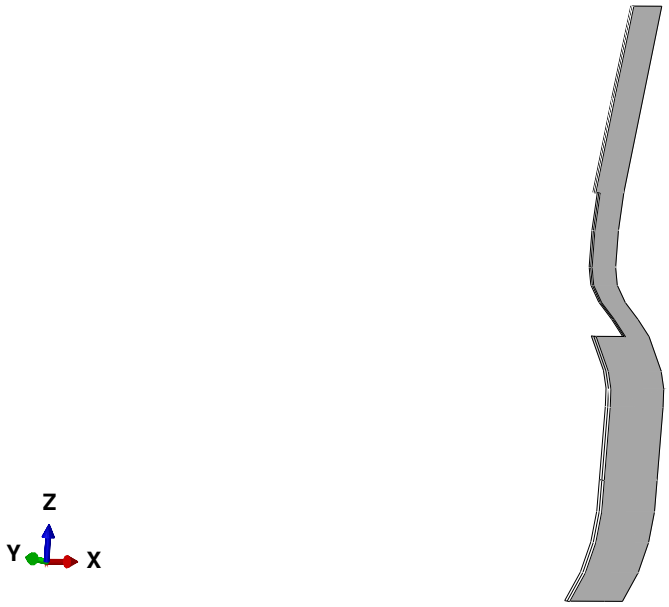

Figure A.10: Starboard view of bow fore CL stiffeners in Abaqus/CAE environment

Appendix B

Discretization to L-, T- and X- elements

In this Appendix, the discretization of each crushed bow section (as described in subsection 4.2.2) to L-, T- and X-elements is presented, in table format.

B.1 Bulb section (Stage I)

The bulb's crushing behavior is first examined. The cross-section discretized is depicted in Figure B.1a, while a cut view of the respective Abaqus/CAE model is depicted in Figure B.1b.

The relevant scantlings of the individual super-elements are presented in Table B.1.

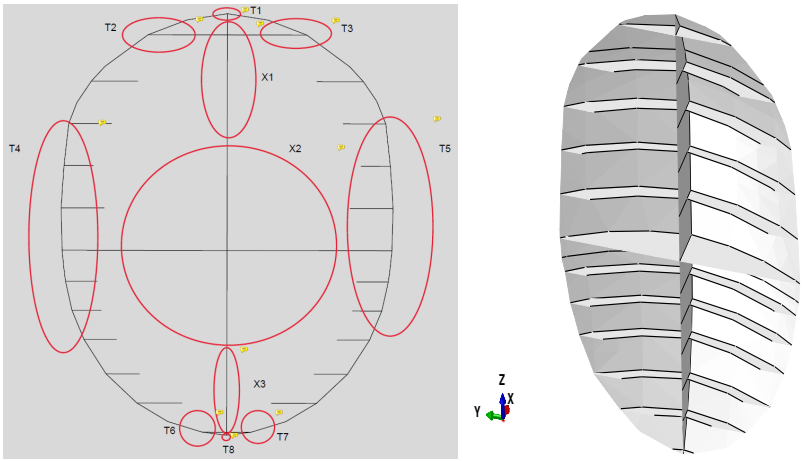

(a) Bulb cross-section super-elements (b) Bulb cut view in Abaqus/CAE

Figure B.1: Bulb discretization to L-, T- and X- elements

Bulb section: Discretization to L-, T- and X-elements

Element #	n_x counter	n_L counter	n_T counter	Element l_1 [mm]	Element t_1 [mm]	Element l_2 [mm]	Element t_2 [mm]	Element area [mm^2]	Element thickness [mm]	Element yield stress [N/mm^2]	Element ultimate tensile stress [N/mm^2]	Element flow stress [N/mm^2]	Summation of element widths [mm]
1 (T1)	0	0	1	1560	17.50	200	15.00	30300	17.25	355.0	490.0	422.5	1760
2 (T2)	0	0	1	1780	17.50	750	9.75	38462.5	16.03	355.0	490.0	422.5	2530
3 (T3)	0	0	1	1780	17.50	750	9.75	38462.5	16.03	355.0	490.0	422.5	2530
4 (X1)	1	0	0	2280	15.00	1500	9.75	48825	13.43	355.0	490.0	422.5	3780
5 (X2)	1	0	0	3690	15.00	3120	12.00	92790.0	13.79	306.6	453.7	380.1	6810
6 (T4)	0	0	1	8400	21.08	1560	12.00	195750.0	20.21	343.5	481.4	412.5	9960
7 (T5)	0	0	1	8400	21.08	1560	12.00	195750.0	20.21	343.5	481.4	412.5	9960
8 (X3)	1	0	0	1780	15.00	464	14.00	33196.0	14.80	331.5	472.4	402.0	2244
9 (T6)	0	0	1	914	17.50	232	14.00	19243.0	16.91	334.7	474.8	404.8	1146
10 (T7)	0	0	1	914	17.50	232	14.00	19243.0	16.91	334.7	474.8	404.8	1146
11 (T8)	0	0	1	470	17.50	30	15.00	8675.0	17.37	355.0	490.0	422.5	500
	n_x [-]	n_L [-]	n_T [-]					Total Area A [mm^2]:	Average weighted thickness t [mm]:			Average weighted flow stress σ_0 [N/mm^2]:	Sum of element widths [mm]:
	3	0	8					720697.0	17.89			409.70	42366.00
													Average weighted element width b [mm]:
													7058.00

Table B.1: Scantlings of bulb section L-, T- and X- elements

B.2 Stem and Bulb section (Stage II)

The combined crushing behavior of the stem and the bulb is examined. The cross-section discretized in depicted in Figure B.2a, while a cut view of the Abaqus/CAE model is depicted in Figure B.2b.

The relevant scantlings of the individual super-elements are presented in Table B.2.

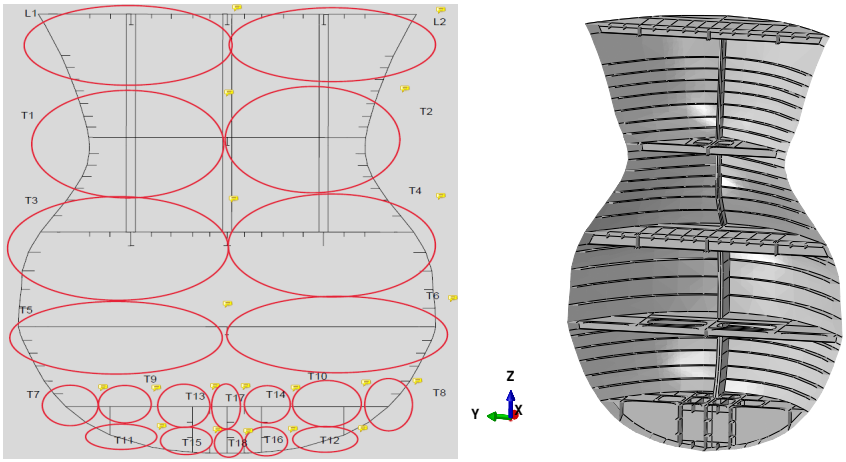

(a) Bulb-stem section super-elements (b) Bulb-stem view in Abaqus/CAE

Figure B.2: Bulb-stem discretization to L-, T- and X- elements

Bulb and Stem section: Discretization to L-, T- and X-elements

Element #	n_x counter	n_L counter	n_T counter	Element l_1 [mm]	Element t_1 [mm]	Element l_2 [mm]	Element t_2 [mm]	Element area [mm^2]	Element thickness [mm]	Element yield stress [N/mm^2]	Element ultimate tensile stress [N/mm^2]	Element flow stress [N/mm^2]	Summation of element widths [mm]
1 (L1)	0	1	0	6970	14.93	3400	19.56	170555	16.74	355.0	490.0	422.5	10370
2 (L2)	0	1	0	6970	14.93	3400	19.56	170555	16.74	355.0	490.0	422.5	10370
3 (T1)	0	0	1	5100	9.49	4350	21.27	140902.5	17.22	313.8	459.1	386.4	9450
4 (T2)	0	0	1	5100	9.49	4350	21.27	140902.5	17.22	313.8	459.1	386.4	9450
5 (T3)	0	0	1	6875	13.22	4750	20.75	189445	17.14	355.0	490.0	422.5	11625
6 (T4)	0	0	1	6875	13.22	4750	20.75	189445	17.14	355.0	490.0	422.5	11625
7 (T5)	0	0	1	7690	12.33	4170	20.54	180465	16.23	291.9	442.7	367.3	11860
8 (T6)	0	0	1	7690	12.33	4170	20.54	180465	16.23	291.9	442.7	367.3	11860
9 (T7)	0	0	1	815	14.00	2750	19.61	65345	18.63	334.0	474.3	404.2	3565
10 (T8)	0	0	1	815	14.00	2750	19.61	65345	18.63	334.0	474.3	404.2	3565
11 (T9)	0	0	1	2335	14.00	610	12.50	40315	13.72	235.0	400.0	317.5	2945
12 (T10)	0	0	1	2335	14.00	610	12.50	40315	13.72	235.0	400.0	317.5	2945
13 (T11)	0	0	1	2635	17.50	610	12.50	53737.5	16.79	338.0	477.2	407.6	3245
14 (T12)	0	0	1	2635	17.50	610	12.50	53737.5	16.79	338.0	477.2	407.6	3245
15 (T13)	0	0	1	2156	14.85	1000	15.70	47724	15.13	235.0	400.0	317.5	3156
16 (T14)	0	0	1	2156	14.85	1000	15.70	47724	15.13	235.0	400.0	317.5	3156
17 (T15)	0	0	1	2180	17.50	1000	15.70	53850	16.98	320.0	463.8	391.9	3180
18 (T16)	0	0	1	2180	17.50	1000	15.70	53850	16.98	320.0	463.8	391.9	3180
19 (T17)	0	0	1	1272	19.79	1000	13.96	39128	17.71	277.8	432.1	355.0	2272
20 (T18)	0	0	1	1272	27.79	1000	13.96	49304	23.87	355.0	490.0	422.5	2272
	n_x [-]	n_L [-]	n_T [-]					Total Area A [mm^2]:	Average weighted thickness t [mm]:			Average weighted flow stress σ_0 [N/mm^2]:	Sum of element widths [mm]:
	0	2	18					1973110.0	16.93			392.85	123336.00
													Average weighted element width b [mm]:
													8505.53

Table B.2: Scantlings of bulb-stem section L-, T- and X- elements

B.3 Section fore of Frame 227 (Stage III)

The combined crushing behavior of the stem and the bulb, following the establishment of stem full contact, is examined, i.e. a section exactly fore of the strengthened Web Frame 227. The cross-section discretized in depicted in Figure B.3a, while a cut view of the respective Abaqus/CAE model is depicted in Figure B.3b.

The relevant scantlings of the individual super-elements are presented in Table B.3.

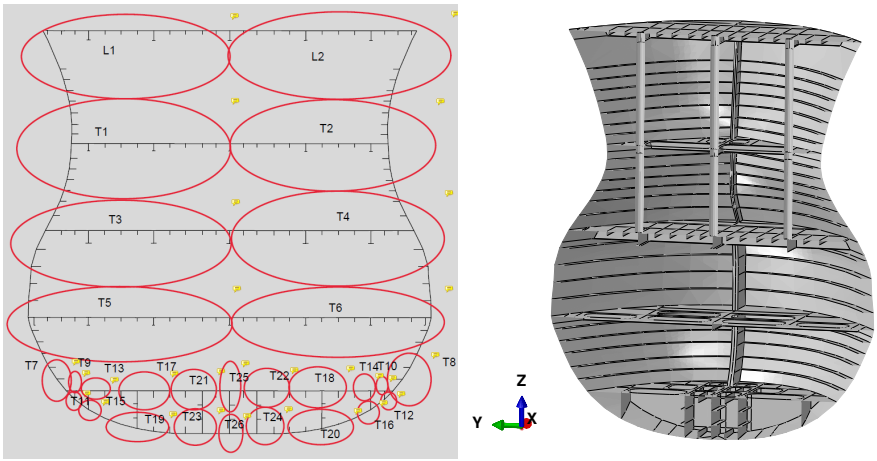

(a) Fr. 227 section super-elements (b) Fr. 227 view in Abaqus/CAE

Figure B.3: Section fore of Fr. 227 discretization to L-, T- and X- elements

Fore of Frame 227 section: Discretization to L-, T- and X-elements

Element #	n_x counter	n_t counter	n_r counter	Element l_1 [mm]	Element t_1 [mm]	Element l_2 [mm]	Element t_2 [mm]	Element area [mm^2]	Element thickness [mm]	Element yield stress [N/mm^2]	Element ultimate tensile stress [N/mm^2]	Element flow stress [N/mm^2]	Summation of element widths [mm]
1 (L1)	0	1	0	8730	16.65	3270	19.65	209565	17.57	355.0	490.0	422.5	12000
2 (L2)	0	1	0	8730	16.65	3270	19.65	209565	17.57	355.0	490.0	422.5	12000
3 (T1)	0	0	1	7400	12.88	4230	21.37	185712.5	17.01	293.4	443.8	368.6	11630
4 (T2)	0	0	1	7400	12.88	4230	21.37	185712.5	17.01	293.4	443.8	368.6	11630
5 (T3)	0	0	1	8600	15.20	4530	20.90	225426.25	17.60	355.0	490.0	422.5	13130
6 (T4)	0	0	1	8600	15.20	4530	20.90	225426.25	17.60	355.0	490.0	422.5	13130
7 (T5)	0	0	1	9400	15.79	4170	21.18	236705	17.80	279.8	433.6	356.7	13570
8 (T6)	0	0	1	9400	15.79	4170	21.18	236705	17.80	279.8	433.6	356.7	13570
9 (T7)	0	0	1	200	15.00	2000	20.41	43810	20.03	346.8	483.8	415.3	2200
10 (T8)	0	0	1	200	15.00	2000	20.41	43810	20.03	346.8	483.8	415.3	2200
11 (T9)	0	0	1	515	15.00	200	12.50	10225	14.39	235.0	400.0	317.5	715
12 (T10)	0	0	1	515	15.00	200	12.50	10225	14.39	235.0	400.0	317.5	715
13 (T11)	0	0	1	680	18.50	200	12.50	15080	17.51	335.1	475.1	405.1	880
14 (T12)	0	0	1	680	18.50	200	12.50	15080	17.51	335.1	475.1	405.1	880
15 (T13)	0	0	1	1458	17.52	320	12.50	29550	16.84	235.0	400.0	317.5	1778
16 (T14)	0	0	1	1458	17.52	320	12.50	29550	16.84	235.0	400.0	317.5	1778
17 (T15)	0	0	1	1660	18.50	550	12.50	37585	17.40	333.0	473.5	403.3	2210
18 (T16)	0	0	1	1660	18.50	550	12.50	37585	17.40	333.0	473.5	403.3	2210
19 (T17)	0	0	1	2660	18.46	615	14.45	57987.5	17.84	235.0	400.0	317.5	3275
20 (T18)	0	0	1	2660	18.46	615	14.45	57987.5	17.84	235.0	400.0	317.5	3275
21 (T19)	0	0	1	2725	20.53	820	13.96	67382.5	19.41	334.6	474.7	404.7	3545
22 (T20)	0	0	1	2725	20.53	820	13.96	67382.5	19.41	334.6	474.7	404.7	3545
23 (T21)	0	0	1	2150	18.42	1000	15.70	55310	17.65	320.9	464.5	392.7	3150
24 (T22)	0	0	1	2150	18.42	1000	15.70	55310	17.65	320.9	464.5	392.7	3150
25 (T23)	0	0	1	2150	26.42	1000	13.96	70770	23.96	331.3	472.2	401.8	3150
26 (T24)	0	0	1	2150	26.42	1000	13.96	70770	23.96	331.3	472.2	401.8	3150
27 (T25)	0	0	1	1272	17.89	1000	13.96	36720	16.40	280.6	434.2	357.4	2272
28 (T26)	0	0	1	1272	25.89	1000	13.96	46896	22.34	355.0	490.0	422.5	2272
	n_x [-]	n_t [-]	n_r [-]					Total Area A [mm^2]:	Average weighted thickness t [mm]:			Average weighted flow stress σ_0 [N/mm^2]:	Sum of element widths [mm]:
	0	2	26					2573833.5	18.11			389.35	147010.00
													Average weighted element width b [mm]:
													9340.18

Table B.3: Scantlings of Fr. 227 section L-, T- and X- elements

B.4 Section fore of Frame 223 (Stage IV)

A section exactly fore of the strengthened Web Frame 223 is examined. The cross-section discretized in depicted in Figure B.4a, while a cut view of the respective Abaqus/-CAE model is depicted in Figure B.4b.

The relevant scantlings of the individual super-elements are presented in Table B.4.

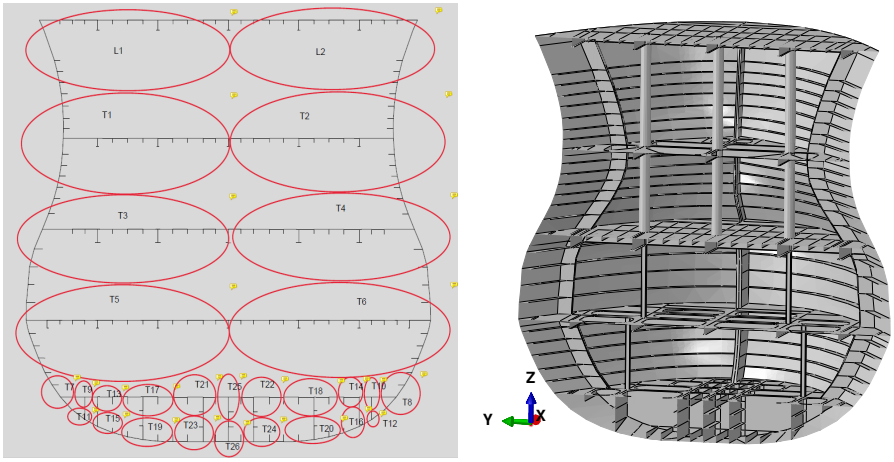

(a) Fr. 223 section super-elements (b) Fr. 223 view in Abaqus/CAE

Figure B.4: Section fore of Fr. 223 discretization to L-, T- and X- elements

Fore of Frame 223 section: Discretization to L-, T- and X-elements

Element #	n_x counter	n_L counter	n_T counter	Element l_1 [mm]	Element t_1 [mm]	Element l_2 [mm]	Element t_2 [mm]	Element area [mm^2]	Element thickness [mm]	Element yield stress [N/mm^2]	Element ultimate tensile stress [N/mm^2]	Element flow stress [N/mm^2]	Summation of element widths [mm]
1 (L1)	0	1	0	9860	21.40	3300	24.63	292302.5	22.30	355.0	490.0	422.5	13160
2 (L2)	0	1	0	9860	21.26	3300	24.63	290862.5	22.20	355.0	490.0	422.5	13160
3 (T1)	0	0	1	8700	17.45	4580	26.08	271237.5	21.25	287.8	439.6	363.7	13280
4 (T2)	0	0	1	8700	17.45	4580	26.08	271237.5	21.25	287.8	439.6	363.7	13280
5 (T3)	0	0	1	9700	19.70	4700	25.78	312226.25	22.06	355.0	490.0	422.5	14400
6 (T4)	0	0	1	9700	19.70	4700	25.78	312226.25	22.06	355.0	490.0	422.5	14400
7 (T5)	0	0	1	10550	20.48	4200	26.15	325930	22.39	275.4	430.3	352.9	14750
8 (T6)	0	0	1	10550	20.48	4200	26.15	325930	22.39	275.4	430.3	352.9	14750
9 (T7)	0	0	1	800	20.00	2700	24.65	82560	23.75	331.7	472.6	402.2	3500
10 (T8)	0	0	1	800	20.00	2700	29.65	96060	28.04	335.0	475.0	405.0	3500
11 (T9)	0	0	1	1100	20.00	600	17.50	32500	19.19	235.0	400.0	317.5	1700
12 (T10)	0	0	1	1100	20.00	600	17.50	32500	19.19	235.0	400.0	317.5	1700
13 (T11)	0	0	1	350	23.50	600	17.50	18725	20.14	287.7	439.5	363.6	950
14 (T12)	0	0	1	350	23.50	600	17.50	18725	20.14	287.7	439.5	363.6	950
15 (T13)	0	0	1	1500	22.45	900	17.50	49430	20.88	235.0	400.0	317.5	2400
16 (T14)	0	0	1	1500	22.45	900	17.50	49430	20.88	235.0	400.0	317.5	2400
17 (T15)	0	0	1	750	23.50	600	17.50	28125	21.26	310.2	456.4	383.3	1350
18 (T16)	0	0	1	750	23.50	600	17.50	28125	21.26	310.2	456.4	383.3	1350
19 (T17)	0	0	1	2660	23.46	950	18.76	80225	22.42	235.0	400.0	317.5	3610
20 (T18)	0	0	1	2660	23.46	950	18.76	80225	22.42	235.0	400.0	317.5	3610
21 (T19)	0	0	1	2350	25.85	1000	18.70	79445	24.17	326.8	468.8	397.8	3350
22 (T20)	0	0	1	2350	25.85	1000	18.70	79445	24.17	326.8	468.8	397.8	3350
23 (T21)	0	0	1	2160	23.41	1000	20.70	71260	22.62	320.1	463.9	392.0	3160
24 (T22)	0	0	1	2160	23.41	1000	20.70	71260	22.62	320.1	463.9	392.0	3160
25 (T23)	0	0	1	2160	31.41	1000	18.96	86800	28.69	328.8	470.3	399.6	3160
26 (T24)	0	0	1	2160	31.41	1000	18.96	86800	28.69	328.8	470.3	399.6	3160
27 (T25)	0	0	1	1272	22.89	1000	18.96	48080	21.34	282.3	435.5	358.9	2272
28 (T26)	0	0	1	1272	30.89	1000	18.96	58256	27.01	355.0	490.0	422.5	2272
	n_x [-]	n_L [-]	n_T [-]					Total Area A [mm^2]:	Average weighted thickness t [mm]:			Average weighted flow stress σ_0 [N/mm^2]:	Sum of element widths [mm]:
	0	2	26					3579928.5	22.63			384.96	162084.00
													Average weighted element width b [mm]:
													10313.63

Table B.4: Scantlings of Fr. 223 section L-, T- and X- elements